SAND2023-04823

SANDIA REPORT

Printed June 2023

Sandia National Laboratories

Improved Compaction Experiments and Modeling of Waste Isolation Pilot Plant Standard, Non-degraded, Waste Containers

Richard P. Jensen, Scott T. Broome, Courtney G. Herrick, Benjamin Reedlunn

Prepared by
Sandia National Laboratories
Albuquerque, New Mexico 87185
Livermore, California 94550

Issued by Sandia National Laboratories, operated for the United States Department of Energy by National Technology & Engineering Solutions of Sandia, LLC.

Available to DOE and DOE contractors from

U.S. Department of Energy
Office of Scientific and Technical Information
P.O. Box 62
Oak Ridge, TN 37831

Telephone: (865) 576-8401
Facsimile: (865) 576-5728
E-Mail: reports@osti.gov
Online ordering: http://www.osti.gov/scitech

Available to the public from

U.S. Department of Commerce
National Technical Information Service
5301 Shawnee Road
Alexandria, VA 22312

Telephone: (800) 553-6847
Facsimile: (703) 605-6900
E-Mail: orders@ntis.gov
Online order: https://classic.ntis.gov/help/order-methods

ABSTRACT

A credible simulation of disposal room porosity at the Waste Isolation Pilot Plant (WIPP) requires a tenable compaction model for the 55-gallon waste containers within the room. A review of the legacy waste material model, however, revealed several out-of-date and untested assumptions that could affect the model's compaction behavior. For example, the legacy model predicted non-physical tensile out-of-plane stresses under plane strain compression. (Plane strain compression is similar to waste compaction in the middle of a long drift.) Consequently, a suite of new compaction experiments were performed on containers filled with surrogate, non-degraded, waste. The new experiments involved uniaxial, triaxial, and hydrostatic compaction tests on quarter-scale and full-scale containers. Special effort was made to measure the volume strain during uniaxial and triaxial tests, so that the lateral strain could be inferred from the axial and volume strain. These experimental measurements were then used to calibrate a pressure dependent, viscoplastic, constitutive model for the homogenized compaction behavior of the waste containers. This new waste material model's predictions agreed far better with the experimental measurements than the legacy model's predictions, especially under triaxial and hydrostatic conditions. Under plane strain compression, the new model predicted reasonable compressive out-of-plane stresses, instead of tensile stresses. Moreover, the new model's plane strain behavior was substantially weaker for the same strain, yet substantially stronger for the same porosity, than the legacy model's behavior. Although room for improvement exists, the new model appears ready for prudent engineering use.

ACKNOWLEDGMENTS

The authors would like to gratefully acknowledge the assistance of several individuals. Mathew Ingraham, Greg Flint, Mike Hileman, and Perry Barrow helped conduct most of the waste compaction experiments. Mark Orlowski and the team at the Southwest Research Institute (SwRI) conducted the hydrostatic testing of the 55-gal drums. Michael Neilsen provided invaluable assistance with calibrating the Foam Damage constitutive model. Jim Bean also provided useful suggestions to calibrate the Foam Damage model and reviewed a draft of the report. Lastly, Chet Vignes ran a disposal room simulation that exercised the new waste compaction material model.

CONTENTS

LIST OF FIGURES

LIST OF TABLES

1. INTRODUCTION

1.1. Background

The Waste Isolation Pilot Plant (WIPP) is a repository for defense-related nuclear waste located in southeast New Mexico. The repository is about 650 m underground in the Salado rock salt formation. As shown in Fig. 1-1, the waste disposal rooms within the repository have a rectangular cross-section and typically contain waste containers, magnesium oxide sacks, and gas. These items initially supply a negligible amount of back pressure, so the salt surrounding the rooms develops deviatoric stresses to support the weight of the overburden above the repository. Salt viscoplastically deforms under deviatoric stress, which causes the rooms to gradually close and compact their contents over the course of decades to centuries. The compaction process continues until the room contents supply sufficient back pressure to resist the lithostatic pressure at the repository horizon, which is $p^{\text{litho}} \approx 14.7$ MPa.

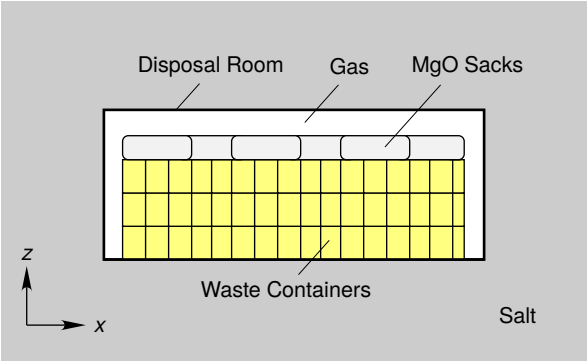

Figure 1-1. Schematic of a disposal room filled with waste containers, magnesium oxide sacks, and gas.

One important reason to develop models for the room closure process is to predict room porosity. Porosity is used to compute the fluid (gas or liquid) pressure within a disposal room in the flow simulations that help predict WIPP's long term-performance. Porosity would also play a critical role in any future effort to predict how the permeability of disposal rooms filled with waste evolves over time. (The WIPP performance assessment flow simulations currently assume that disposal rooms have a constant permeability.)

The legacy model used to predict WIPP disposal room porosity was developed in the 1980's and 1990's, culminating in the simulations by Stone (1997a). This disposal room porosity model can be divided into three sub-models: a model for the geomechanical behavior of the surrounding rock mass, a model for the gas trapped in the room, and a model for compaction of standard waste containers. Stone (1997a) ignored the magnesium oxide sacks. Stone's (1997a) porosity predictions were used in the original WIPP Compliance Certification Application (CCA) and in

each Compliance Recertification Application (CRA) since then. More recently, Reedlunn et al. (2022) updated the geomechanical model, King (2021) revised the gas generation function, and this report concerns revisions to the material model for standard waste containers.

The legacy waste material model was designed to capture the compaction behavior of standard 55-gallon drums (a.k.a. standard waste) filled with various types of contaminated debris. Standard drums are not the only type of container emplaced in WIPP disposal rooms, but they are the most prevalent. The inventory estimate for CRA-2019 (LANL, 2018) reported that standard drums made up 68.6 % of the containers in the repository. A defensible material model for standard drums is, therefore, necessary to reasonably predict disposal room porosity. The reasons for revising the legacy waste material model will be discussed after reviewing the legacy waste compaction experiments and model development.

1.2. Legacy Waste Compaction Experiments

Several studies of standard, non-degraded, waste container compaction have been published. Baker et al. (1980); Huerta et al. (1983) conducted quasi-static and impact tests in order to evaluate transportation accident scenarios. VandeKraats (1987) and a study from 1989, reported subsequently by Wawersik (2001), quasi-statically compacted waste containers to help develop models for WIPP disposal room closure. In order to be consistent with the planned WIPP waste emplacement method at that time, VandeKraats (1987) and the 1989 study compacted their samples consisting of containers surrounded by crushed salt. Now that waste is being emplaced at the WIPP without crushed salt backfill, these particular experiments are perhaps less relevant. The most relevant legacy experiments are those by Butcher et al. (1991), which formed the basis for the legacy waste material model.

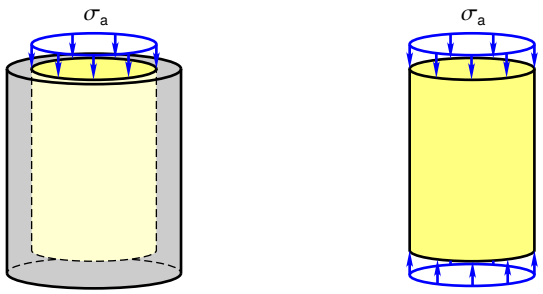

Figure 1-2. Schematics of the waste compaction tests utilized in Butcher et al. (1991).

Butcher et al. (1991) performed two series of experiments. The first series involved uniaxial strain compaction of various surrogate, non-degraded, waste components in an oedometer (see Fig. 1-2a). Five waste components were considered: rubbers/plastics, cellulosics, sorbents, metals, and "sludges". Only one waste component was tested in the oedometer at a time. Axial strain ε_a and axial stress σ_a were measured as the waste component was compacted, but the lateral (radial) stress σ_l associated with the waste pushing against the relatively rigid oedometer

wall was not measured. The friction between the waste component and oedometer wall also was not accounted for. As one might expect, each waste component was relatively compliant to begin with, but gradually became stiffer as further compaction was applied and the porosity was reduced. The second test series involved uniaxial stress compaction (see Fig. 1-2b) of a full-scale 55-gallon drum filled with various surrogate, non-degraded, waste components mixed together. Axial strain and axial stress were measured, while lateral (radial) strain ε_l was typically assessed by qualitative observation. All drums compacted with minimal lateral strain early in the tests, but compaction of drums filled mostly with inorganic sludge split open on the sides towards the end the tests, while drums filled mostly with metals, plastics, and cellulosics did not exhibit similar obvious signs of lateral expansion. Nevertheless, Butcher et al. (1991, Section 3.3.2) filled the void space within two drums with water before compaction, measured the volume of expelled water during compaction, and computed the lateral strain from the volumetric and axial strain. These two drums laterally shrank slightly during the first half of axial compaction, and then began to bulge outward as axial compaction continued. Unfortunately, water leaks two-thirds through these two tests halted the volumetric strain measurements thus preventing the determination of lateral strain before substantial lateral expansion occurred.

1.3. Legacy Waste Compaction Model Development

The constitutive model at the core of the legacy waste compaction model is the Soil and Foam (SAF) constitutive model (a.k.a. Crushable Foam model). The SAF model is implemented in the SANTOS (Stone, 1997b) and Sierra/SolidMechanics (2022) finite element codes, and its yield surface is a surface of revolution about the hydrostat combined with a planar end cap whose normal aligns with the hydrostat. The surface of revolution does not harden, but the end cap hardens by translating along the hydrostat towards higher pressure if the material experiences a compressive volume strain greater than the previous most compressive volume strain. The hydrostatic pressure p vs. volume strain ε_v relationship associated with the end cap translation is a user input to the SAF model.

The SAF constitutive model was calibrated against the Butcher et al. (1991) test results to create the legacy waste material model. The p vs. ε_v relationship was derived from the oedometer tests in the following five steps:

1. Butcher et al. (1991, Section 4.3) computed a composite σ_a vs. ε_v response as a weighted average of the responses for the individual waste components. The weighting was based on an expected (assumed) composition of waste in a drum.

2. Butcher (1997a, Pg. A-1 through A-21, and C-2 through C-6) updated the σ_a vs. ε_v response based on DOE (1995)'s updated expectations for the waste composition[1]. See Fig. 1-3 for a plot of this curve.

3. Butcher (1997b, Section 3.2.2) assumed $\sigma_l = 0$ in the oedometer tests so they could compute the hydrostatic pressure as $p = (\sigma_l + \sigma_h + \sigma_a)/3 = \sigma_a/3$. (The hoop stress $\sigma_h = \sigma_l$

[1]One can also find the updated waste composition estimates in Butcher (1997a, Table 5 and 6) and Stone (1997a, Table 1), except the column heading of "volume fraction" should be "weight fraction" in both locations.

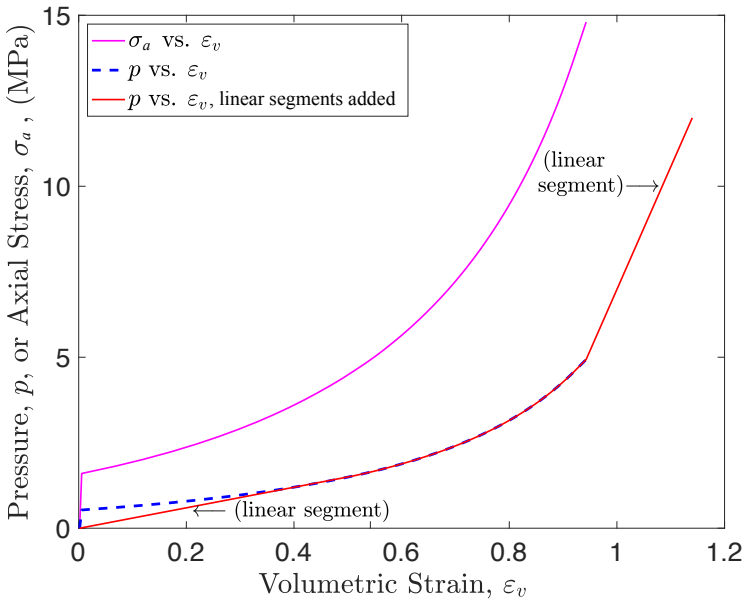

Figure 1-3. Construction of the legacy waste material model's hydrostatic response.

in an axisymmetric oedometer test.) They justified assuming $\sigma_l = 0$ by the lack of lateral expansion in the early portions of the uniaxial stress compaction tests on full-scale drums. This resulted in a hydrostatic response that ranged from (ε_v, p) = (0, 0.53 MPa) to (0.942, 4.93 MPa), as shown by the blue dashed curve in Fig. 1-3.

4. Butcher (1997a) replaced the early response with a linear segment from (ε_v, p) = (0, 0.0 MPa) to (0.510, 1.53 MPa) to force the response to begin at zero pressure (see Fig. 1-3).

5. Butcher (1997a) extended the response from (ε_v, p) = (0.942, 4.93 MPa) to (1.14, 12.0 MPa) by adding a linear segment with an assumed slope that was steeper than the preceding slope (see Fig. 1-3).

Although the p vs. ε_v relationship was (loosely) based on experimental measurements, the elastic parameters and yield surface of revolution were selected without experimental justification. Stone (1997a) chose to make yield surface of revolution a Drucker-Prager yield surface. The legacy waste material model parameters can be found in Stone (1997a, pg. 21–23)[2].

Once the legacy waste material model was fully defined, Stone (1997a) used it in a number of disposal room porosity simulations. Rather than model each individual container, he

[2]Stone (1997a, Table 5) and Butcher (1997a, Table 7) made two mistakes when they listed the elastic shear and bulk moduli as $G = 333$ MPa and $K = 222$ MPa, respectively. The precise values for the elastic moduli should have minimal impact on the disposal room porosity predictions, so we note these two mistakes primarily in the spirit of accurate documentation. First, Butcher (1997a, Table 7) cites Weatherby et al. (1991) for the elastic properties of the waste, yet Weatherby et al. (1991) actually lists $G = 222$ MPa and $K = 333$ MPa. Second, the input file for the disposal room porosity simulation (Stone, 1997a, Appendix A), however, shows he actually used $G = 333/2 = 166.5$ MPa. The legacy model simulations presented herein utilized $G = 166.5$ MPa and $K = 222$ MPa to be consistent with the simulations performed by Stone (1997a, Appendix A).

homogenized the standard waste containers within a room into a continuous effective material, thereby creating the legacy waste compaction model.

1.4. Shortcomings of the Legacy Waste Compaction Experiments and Material Model

Not long after Stone (1997a) was released, the adequacy of the legacy waste material model was questioned, particularly its non-physical predictions under plane strain conditions. WIPP disposal rooms are long and slender, so they are commonly modeled using plane strain conditions, where no deformation is permitted along the length of the room, which is the out-of-plane direction. Under these conditions, one would expect the waste within the room to push against the out-of-plane zero displacement boundary condition, thereby producing compressive stresses, but Callahan (2004); Callahan and Hansen (2005); Park and Hansen (2005) showed that the legacy waste material model predicts tensile stresses in the out-of-plane direction. The Park and Hansen (2005) simulation was performed with SANTOS, the same finite element code used in Stone (1997a), while the Callahan (2004); Callahan and Hansen (2005) simulations were performed with SPECTROM-32 (Callahan, 2002), a different finite element code developed by RESPEC. Both codes produced similar out-of-plane tensile stress values, which suggests these tensile stresses were not due to numerical implementation errors; the legacy waste material model simply predicts erroneous out-of-plane tensile stresses in disposal room simulations.

Callahan (2004); Callahan and Hansen (2005) sought to eliminate these tensile out-of-plane stresses with two different approaches. They did not have new experimental measurements, so both approaches were simply sensitivity studies. In the first approach, they constructed three different variations of the legacy model, each with a different Drucker-Prager yield surface. The best version predicted the out-of-plane stresses were tensile for about 1,000 years and then became compressive, which was enlightening, but not a clear success. In the second approach, they simulated the waste with a non-linear elastic material model and used various values for the effective Poisson's ratio. All variations of the elastic waste material model predicted compressive out-of-plane stresses throughout a disposal room porosity simulation, which was encouraging, but this approach was not pursued further. Presumably it was not satisfying to treat the waste as a fully elastic material because the room can close and subsequently reopen if gas pressure can build within the room. Fully elastic waste would significantly assist the gas in reopening the room, while an elastic-plastic model would help reopen the room only a slight amount as it elastically unloads.

Although the Callahan (2004); Callahan and Hansen (2005) study did not result in a new waste material model, interest in revising the legacy waste material model for non-degraded waste has remained. A recent careful review of the legacy model uncovered the following shortcomings:

1. The waste composition utilized by Butcher (1997a) was substantially different than that reported in the last several WIPP inventory reports, as shown in Fig. 1-4a. Utilizing roughly half as much metal than disposed in actual standard waste containers, for example, likely reduced the legacy waste model's strength.

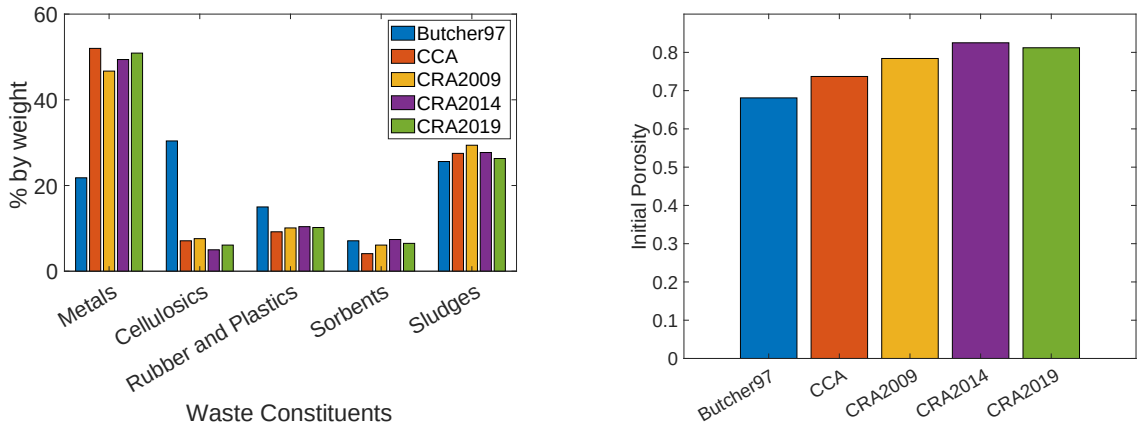

(a) Waste weight fractions **(b) Waste initial porosity**

Figure 1-4. Waste weight fractions and initial porosity comparisons. Raw data and references are listed in Tables 2-2 and 2-3.

2. The waste container initial porosity utilized by Butcher (1997a) was lower than that reported in the last several waste inventories, as shown in Fig. 1-4b. A lower initial porosity would cause the legacy model to exhibit increased resistance early in the compaction process, and the final volume of the fully compacted canister would be larger which would lead to a larger final disposal room volume.

3. Although Butcher (1997b, Section 3.2.2) could reasonably assume $\sigma_l = \sigma_h = 0$ as the waste was first compacted in the oedometer, one should expect substantial radial and hoop stresses once the waste densifies past some point. Ignoring these substantial radial and hoop stresses likely made the legacy model too compliant during the latter portions of Stone (1997a)'s disposal room porosity simulations.

4. The compaction stiffness near p^{litho} probably had an impact on the final predicted room porosity, so the stiffness for 4.93 MPa $< p \leq p^{\text{litho}}$ should have been experimentally characterized instead of assumed[3].

5. As previously mentioned, the legacy waste model's Drucker-Prager yield surface was not calibrated against experimental measurements. Callahan (2004); Callahan and Hansen (2005) found that varying the legacy model's Drucker-Prager yield surface had a moderate effect on the final waste porosity in disposal room simulations.

6. As previously mentioned, the legacy waste model predicts out-of-plane tensile stresses in disposal room simulations. A simpler manifestation of this same problem is found with a material point under plane strain (see Fig. 1-5a), where the out-of-plane strain $\varepsilon_{\text{yy}} = 0$ and in-plane normal stresses $\sigma_{\text{xx}} = \sigma_{\text{zz}}$ are applied. As shown in Fig. 1-5b, this plane strain loading causes compressive in-plane stresses, but the out-of-plane normal stress σ_{yy} is

[3] Although Butcher (1997a) only extended the response to $p \leq 12$ MPa, instead of $p \leq p^{\text{litho}}$, the SAF model was never forced to extrapolate beyond 12 MPa in the disposal room simulations because, as shown in Fig. 1-5b, the out-of-plane tensile stress σ_{yy} kept $p \leq 12$ MPa, even when the in-plane compressive stresses reached $\sigma_{xx} \approx \sigma_{zz} \approx p^{\text{litho}}$.

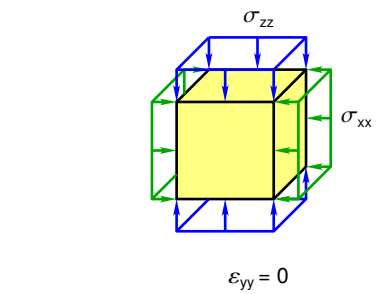

(a) Plane strain schematic

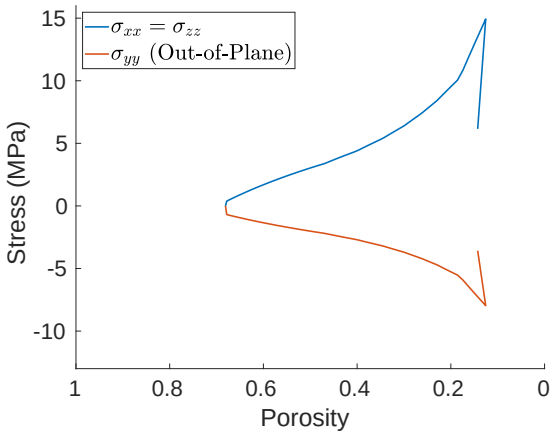

(b) Plane strain predictions

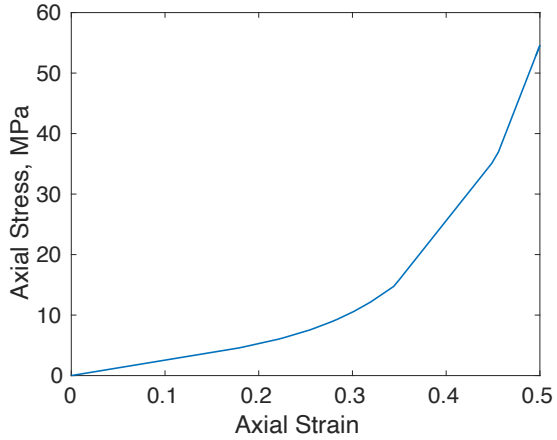

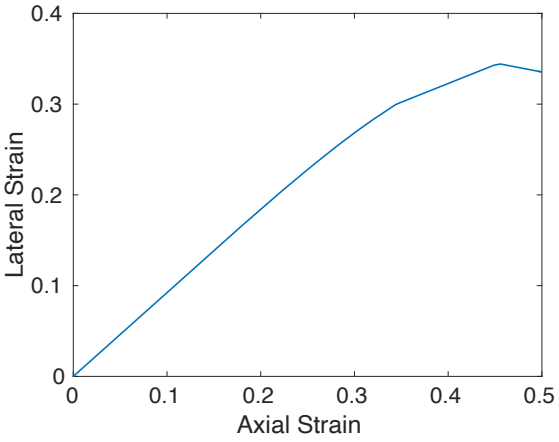

(c) Uniaxial stress predictions

Figure 1-5. Legacy waste material model behavior under uniaxial stress and plane strain compaction. Note the prediction of negative (tensile) out-of-plane stress σ_{yy} during plane strain compaction and the positive lateral strain (lateral shrinkage) during uniaxial stress compaction.

tensile (negative). Similar behavior happens even under uniaxial compression in Fig. 1-5c, where the model predicts considerable lateral shrinkage (positive lateral strain). Thus, although (Butcher, 1997b, Section 3.2.2) justified assuming $\sigma_{rr} = \sigma_{\theta\theta} = 0$ by the lack of lateral strain *early* in their uniaxial stress compaction tests, the legacy waste material model is not consistent with this justification.

7. Several waste constituents, such as metals, plastics, and cellulosics, likely exhibit strain rate sensitivity, yet the legacy waste material model assumes rate-independent behavior.

Careful experiments that characterize the waste's actual behavior are a crucial component to overcoming the model shortcomings listed above, so the experiments documented in Baker et al. (1980); Huerta et al. (1983); Wawersik (2001); Butcher et al. (1991) were also reviewed. This review found these studies were inadequate to improve the waste material model for the following reasons:

1. These prior studies all used waste compositions and porosities that differ from waste actually disposed at the WIPP because these studies were conducted before the WIPP began accepting and cataloging waste.
2. These prior studies only used uniaxial stress, uniaxial strain, or something in-between due to the compliant lateral confinement provided by the crushed salt. If the gas pressure within a disposal room remains low, one can readily expect the waste compaction to transition from uniaxial compression between the floor and ceiling, towards a more hydrostatic stress state as the waste laterally expands outward and the room walls close inward. Despite this expectation, no hydrostatic compression or triaxial (axisymmetric) compression tests were performed.
3. The studies did not successfully measure the lateral strains throughout their uniaxial stress experiments, did not measure the lateral stresses in their uniaxial strain experiments, and/or did not obtain measurements of the lateral stress/strain evolution related to the compliant lateral confinement provided by the crushed salt.
4. Although perhaps less important than the aforementioned reasons, the existing studies did not probe the rate sensitivity of the waste.

Consequently, new experiments and a new model were both needed. These experimental and modeling efforts were performed under TP 08-01 (Broome and Costin, 2010) and AP-180 (Herrick, 2017), respectively.

1.5. Organization

The remainder of this report documents the experiments and modeling performed to rectify the shortcomings listed above. Chapter 2 presents a series of new compaction experiments on surrogate, non-degraded, waste. Chapter 3 describes the new waste material model based on those experiments. Chapter 4 discusses possible future work. Chapter 5 concludes the report with a summary of the findings and results.

2. WASTE COMPACTION EXPERIMENTS

The purpose of the experimental program was to provide data that would allow for the calibration of a new waste material model that does not suffer from the shortcomings discussed in Chapter 1. To avoid these shortcomings, the uniaxial, triaxial, and hydrostatic tests were performed on 1/4-scale and full-scale containers to characterize the deviatoric and volumetric behaviors. Both axial and volume strain measurements were collected in the uniaxial and triaxial tests to infer, rather than assume, the lateral strain behavior.

This chapter documents two sets of experiments. The first set of uniaxial, triaxial, and hydrostatic experiments were originally documented in Broome et al. (2016); Orlowski (2015), but this report is intended to serve as the more complete reference. These first experiments were conducted at axial and volumetric engineering strain rates of 10^{-4} 1/s. The second set of experiments, which have not been documented before, were uniaxial compression tests on 1/4-scale containers at slower axial engineering strain rates of 10^{-5}, 2.1×10^{-6}, and 10^{-7} 1/s. All files associated with these waste compaction experiments are archived at `/data/cvs/CVSLIB/WIPP_EXTERNAL/tp08-01_files` on Sandia Carlsbad's Linux Server.

The remainder of this chapter is organized as follows: Section 2.1 discusses the waste composition and porosity; Section 2.2 presents the sample preparation; Section 2.3 covers the laboratories and testing systems; Section 2.4 describes the data reduction procedures, and Section 2.5, Section 2.6, and Section 2.7 contain the experimental results for the uniaxial, triaxial, and hydrostatic tests, respectively.

2.1. Waste Composition and Porosity

The material used during the tests described herein is a surrogate contact-handled, non-degraded (a.k.a. "fresh"), WIPP waste mixture. Non-degraded waste represents newly emplaced waste and degraded waste represents waste that has degraded under potential repository conditions for the entire 10,000-year regulatory period. Compaction experiments on degraded waste can be found in Hansen and Mellegard (1998); Broome et al. (2014), but a waste material model has not been developed to simulate those experimental results. During the Broome et al. (2014) experiments, hydrostatic compression, triaxial compression, and uniaxial strain tests were performed with volumetric and radial strain measurements recorded.

The (non-degraded) waste composition utilized to generate the new (non-degraded) waste material model was chosen to reasonably match the composition of waste actually disposed at the WIPP over the past two decades, resolving legacy model Shortcoming 1 in Section 1.4. Table 2-1 provides a description of each waste component, while Table 2-2 and Fig. 1-4a compare the weight fraction of each component against the inventory estimates used in the legacy waste

Table 2-1. Descriptions of WIPP waste components.

Component	Description
Metals	iron based metals/alloys, steel containers, aluminum based metals/alloys, other metals/alloys
Cellulosics	cellulosics, cellulosics packaging material
Rubber and Plastics	rubber, rubber container materials, plastics, plastic container/liner material
Sorbents	other inorganic materials
Sludges	vitrified, solidified inorganic material, solidified organic material, solidification cements, soils

Table 2-2. Comparison of weight fractions (expressed as percentages) of the five major waste components used in the legacy waste material model, CCA, and last three CRAs. The cells marked in yellow correspond to the weight percentages used for the waste compaction tests documented in this report.

Waste Component	Legacy Model (TWBIR, rev1[a])	CCA (TWBIR, rev3[b])	CRA-2009 (PAIR-2008[c])	CRA-2014 (PAIR-2012[d])	CRA-2019 (PAIR-2018[e])
Metals	21.8	52.0	46.7	49.4	50.9
Cellulosics	30.4	7.1	7.6	5.0	6.1
Rubber and Plastics	15.0	9.2	10.1	10.4	10.2
Sorbents	7.1	4.1	6.1	7.4	6.5
Sludges	25.6	27.5	29.4	27.7	26.3

[a] DOE (1995)
[b] DOE (1996)
[c] LANL (2008)
[d] LANL (2012)
[e] LANL (2018)

material model, CCA, and recent CRAs (CRA-2009 through CRA-2019). As noted in the column headings and footnotes of Table 2-2, the inventory estimates were computed from various Transuranic Waste Baseline Inventory Report (TWBIR) and Performance Assessment Inventory Reports (PAIRs). Fig. 1-4a clearly shows that the legacy model waste composition does not resemble more recent inventory estimates, but the waste composition has remained relatively stable since the CCA (TWBIR rev. 3). Furthermore, the Environmental Protection Agency (EPA) has accepted the CCA (TWBIR, rev. 3) weight fractions for other WIPP model parameter determinations, including the Spallings model (EPA, 2006) and the Waste Shear Strength parameter (EPA, 2017, 2022). The current study, therefore, utilized the CCA (TWBIR, rev. 3) weight fractions shown in Table 2-2 when creating waste compaction samples.

Similarly, the initial density and solid density of the waste compaction samples were chosen to resolve legacy model Shortcoming 2 in Section 1.4. Table 2-3 lists the initial waste density ρ_0,

Table 2-3. Comparison of the estimated material densities (kg/m^3) and porosities used in the legacy waste material model, CCA, and last three CRAs. The cells marked in yellow correspond to the densities and porosity used for the waste compaction tests documented in this report.

Waste Material	Legacy Model (TWBIR, rev1)	CCA (TWBIR, rev3)	CRA-2009 (PAIR-2008)	CRA-2014 (PAIR-2012)	CRA-2019 (PAIR-2018)
ρ_0 (kg/m^3)	559.5	757.6	587.2	505.5	543.2
ρ_s (kg/m^3)	1755.6	2881.8	2721.9	2889.9	2886.2
ϕ_0 (−)	0.681	0.737	0.784	0.825	0.812

solid density ρ_s, and initial porosity $\phi_0 = 1 - \rho_s/\rho_0$ of the waste for several inventory estimates since 1995. These values were computed following the method described in a 1997 memorandum by Papenguth and Myers, which can be found in Appendix A of Hansen et al. (1997). As shown in Fig. 1-4b, the initial waste porosities have not dramatically changed since CRA-2009, so one can expect them to remain relatively stable as more standard waste drums are emplaced at the WIPP in the future. The waste densities and porosity studied herein were chosen to match those used in CRA-2014, because the CRA-2014 estimate was the most recent one when the first set of tests on surrogate, non-degraded waste were started.

2.2. Waste Specimen Preparation

Two types of waste containers were used for the new tests. The first was a United States Department of Transportation Specification 7A; General Packaging, Type A (US DOT 7A Type A) 55-gal drums. These drums are designed and certified for the transport of radioactive materials. The second container type was No. 12 food cans are referred herein to as 1/4-scale cans.

Table 2-4. Comparison of full-scale 55-gallon drums with proposed 1/4-scale container dimensions. The values in the yellow cells were used when reducing the experimental measurements (see Section 2.4).

Container Type	D_0 (mm)	L_0 (mm)	H_0 (mm)
DOT-7A Type A[a]	609.6	881.4	1.519
Exact 1/4-scale	152.4	220.3	0.380
No. 12 food can	156.7	222.3	0.315

[a]The DOT-7A Type A 55-gallon drums used in this study are from Skolnik Industries, Inc, in Chicago, IL. The part number is CQ5508. The dimensions are converted from their detailed drawing CQ5508_A5.pdf (https://www.skolnik.com/documents/CQ5508_A5.pdf)

The 1/4-scale cans are a very close 1/4-scale representation of the US DOT 7A Type A 55-gal drums, as noted by Baker et al. (1980); Huerta et al. (1983). To compare, Table 2-4 lists the rim

diameter D_0, height L_0, and wall thickness H_0 of 55-gallon drums, an exact 1/4-scaling of the drums, and the No. 12 food cans. The quarter dimensional scaling is quite good for No. 12 food cans except for the wall thickness, which results in the food can being slightly thinner than optimally desirable. In addition, the construction of the containers is somewhat different. The principal difference is the lid attachment: the DOT 55-gallon drums use a ring clamp secured with a bolt whereas the food can lid is crimped in place.

Despite differences in the lip-closure configuration, lid and wall thickness, yield and ultimate strengths of the food cans, and drum fill materials, Huerta et al. (1983) found that the compaction behaviors of a No.12 food can and a 55-gallon drum filled with appropriately scaled waste were similar. To validate that this scaling also holds for the waste specimens utilized herein, the uniaxial and hydrostatic tests discussed in Sections 2.5 and 2.7 used both 1/4- and full-scale containers.

A listing of the waste components and weights used in the two containers are given in Tables 2-5 and 2-6. The surrogate materials used for each waste constituent were largely the same as those used in Butcher et al. (1991). One minor difference was the constituent part sizes were chosen so that those used in the 1/4-scale cans were one fourth the size of the same components used in the full-scaled drums. The raw materials used were all off-the-shelf products. For the steel and plastic components, the weights of the containers, lids, and packaging materials did not match the inventory estimates perfectly. For both of these, the containers and lids were weighed, and the internal material weights adjusted so that they matched the inventory estimate. These are shaded in green in Tables 2-5 and 2-6 to draw attention to them. In the same vein, some of the other materials could not achieve the target weight and stay within the nominal sizes listed in the tables. For these instances, small portions of the same material type were added to compensate for the additional weight needed to reach the target weight.

The surrogate waste materials were added randomly to the drum, whether a 1/4-scale drum (Fig. 2-2) or a full-scale 55-gallon drum (Fig. 2-1). This random emplacement procedure filled the cans/drums between 66 % to 75 % of the drum capacity. The fill percentage is the ratio of the material height in the drum to the total drum height and is different than the solid volume fraction or porosity. To maintain the random distribution of materials, the drums/cans were moved only as necessary after filling.

It is not straightforward to compute the fill percentage corresponding to the legacy waste model; however, one can compare the porosity of a can/drum 100 % filled with the current waste mixture ($\phi_{0\,\text{full}}$) against the legacy model's porosity. One can estimate $\phi_{0\,\text{full}}$ by assuming the fill percentage is linearly proportional to the solid volume fraction $1-\phi_0$, constructing the ratio $(1-\phi_{0\,\text{full}})/(1-\phi_0) = 1.0/0.66$ with $\phi_0 = 0.825$, and solving to obtain $\phi_{0\,\text{full}} = 0.734$. This value still does not match Butcher (1997a)'s porosity of 0.681, but the current cans/drums would have to be > 100 % filled to lower $\phi_{0\,\text{full}} = 0.734$ to 0.681. Overfilling could explain how Butcher's (1997a) weighted averaging of the waste component responses produced $(\varepsilon^{\text{vol}},\ p) = (0,\ 0.53)$ MPa at $\phi_0 = 0.681$, but it is not possible to prove this since the Butcher (1997a) waste composition might simply settle to a lower fill percentage for a given porosity than the waste composition utilized herein.

The drums/cans were specially prepared to measure the airflow in and out of the container during compaction as a means to quantify the volumetric strain. A 1/4" pipe for the full-scaled drums and

Figure 2-1. Photograph of surrogate waste components used in a full-scale 55-gallon drum.

(a) 1/4-scale can **(b) Full-scale 55-gallon drum**

Figure 2-2. Photographs of a 1/4-scale can and full-scale 55-gallon drum randomly filled with surrogate waste and ready for sealing with a lid. Note that the waste constituent sizes are scaled according to the container type.

Table 2-5. List of the surrogate waste materials used in the 1/4-scale cans. Weights were determined using a can volume of 4287 cc and a waste density of 0.5055 g/cc. The can and packaging materials do not match the inventory estimates identically for steel and plastic, so the difference was adjusted for in the internal container components. These are shaded in green. The initial porosity is calculated to be 0.825.

Waste material listed in inventory report		Surrogate waste material used in 1/4-scale cans	Target 1/4-scale weight (g)	1/4-scale can weight fraction (%)
Metals	iron based metals	≈ 1/2" diam. rod stock, ≈ 2" long	464	21.4
	steel containers	can and lid	420	19.4
	aluminum based metals	≈ 1/4" square stock, ≈ 2" long	51	2.4
	other metals	≈ 5/8" diam. x ≈ 1/32" wall x ≈ 3" long copper tube	192	8.9
	total metals		1127	52.0
Cellulosics	cellulosics	≈ 1" pine cube	94	4.3
		cotton rags	60	2.8
	total cellulosics		154	7.1
Rubber and Plastics	rubber	latex gloves cut in half	29	1.3
	plastics	half of 1000cc polyethylene bottle, cut into ≈ 10 pieces	36	1.7
	plastics	≈ 0.84" OD (1/2" HDPE pipe) x ≈ 1/16" wall x ≈ 1.8" long	35	1.6
	plastics	1/2" Schedule 40 PVC pipe, ≈ 1.8" long	100	4.6
	plastic container/liner mat'ls	no liner for 1/4-scale cans, liner weight included in poly bottle		
	total rubber and plastics		200	9.2
Sorbents	other inorganic mat'ls	portland cement	45	2.1
		Oilsorb	45	2.1
	total sorbents		89	4.1
Sludges	vitrified	Pyrex glass pass 1" sieve	157	7.2
	solidified inorganic mat'ls	Hydrostone pass 1" sieve	155	7.2
	solidified organic mat'ls	Kent marine organic absorption resin or equivalent	16	0.7
	cements (solidified)	Quickrete or similar pass 1" sieve	143	6.6
	soils	soil pass 1" sieve	126	5.8
	total sludges		597	27.5
Waste Total			2167	100.0

Table 2-6. List of the surrogate waste materials used in the full-scale drums. Weights were determined using a can volume of 212,358 cc and a waste density of 0.5055 g/cc. The drum and packaging materials do not match the inventory estimates ("target") identically for steel and plastic, so the difference was adjusted for in the internal container components. These are shaded in green. The initial porosity is calculated to be 0.825.

Waste material listed in inventory report		Surrogate waste material used in full-scale drums	Target full-scale weight (g)	Full-scale drum weight fraction (%)
Metals	iron based metals	2" diam. rod stock, 3" to 8" long	17332	16.1
	steel containers	can and lid	26451	24.6
	aluminum based metals	1" square stock, 2" to 8" long	2551	2.4
	other metals	$2^1/_8$" diam. x ≈ $^1/_{16}$" wall thick x 8" to 16" long copper tube	9494	8.8
	total metals		55287	52.0
Cellulosics	cellulosics	construction grade 4"×4", 3" to 5" long pine	6161	5.7
		cotton rags	1490	1.4
	total cellulosics		7651	7.1
Rubber and Plastics	rubber	latex gloves	1417	1.3
	plastics	ten 1-gallon poly bottles	1011	0.9
	plastics	2" diameter HDPE pipe or next smaller size, 5" to 9" long	932	0.9
	plastics	2" diameter Schedule 40 PVC pipe, 5" to 9" long	1891	1.8
	plastic container/liner mat'ls		4668	4.3
	total rubber and plastics		9919	9.2
Sorbents	other inorganic mat'ls	portland cement	2196	2.0
		Oilsorb	2196	2.0
	total sorbents		4393	4.1
Sludges	vitrified	Pyrex glass pass 4" sieve	7793	7.3
	solidified inorganic mat'ls	Hydrostone pass 4" sieve	7651	7.1
	solidified organic mat'ls	Kent marine organic absorption resin or equivalent	794	0.7
	cements (solidified)	Quickrete or similar pass 4" sieve	7085	6.6
	soils	soil pass 4" sieve	6235	5.8
	total sludges		29557	27.5
Waste Total			107347	100.0

a 1/4" tube for the 1/4-scale cans were added to the lids to serve as vent ports. A piece of felt metal was placed over the vent ports, on the inside of the drum, to help ensure that the port did not get clogged by a piece of surrogate waste material covering it. Once the container was filled with surrogate waste, the container lid was sealed. The 1/4-scale can lids were sealed with an industrial can sealer; the full-scaled drum lids were sealed by a ring clamp tightened to create an air-tight seal. These samples were then jacketed with different materials to prevent confining fluid from infiltrating the sample in the case of hydrostatic or triaxial compression experiments, and to ensure reliable volumetric strain measurements. Specific jacketing materials and techniques will be discussed in the different compaction test sections. These modifications are believed to have an insignificant effect on the compaction behavior of the containers. Moreover, adding a vent to each sample is consistent with actual WIPP waste containers: WIPP waste containers are vented so that gas pressure does not build up inside of them during transportation and emplacement.

The nomenclature for the test samples in this study is:

- 1/4-scale hydrostatic: WC-HC-NDQ-##
- 1/4-scale uniaxial: WC-UC-NDQ-##
- 1/4-scale triaxial: WC-TX-NDQ-CP-##
- Full-scale hydrostatic: WC-HC-NDF-##
- Full-scale uniaxial: WC-UC-NDF-##

where WC is waste compaction, HC is hydrostatic compaction, UC is uniaxial compaction, TC is triaxial compaction, NDQ is non-degraded quarter-scale, NDF is non-degraded full-scale, and ## is the respective sample number. For triaxial samples, the letters CP are replaced by the confining pressure in MPa and then the respective sample number is listed by ##.

2.3. Testing Systems

The tests described in this report were conducted at two different sites. The majority of the tests were conducted in the Geomechanics Laboratory of Sandia National Laboratories in Albuquerque, New Mexico, but the Marine Engineering Department of the Southwest Research Institute (SwRI) in San Antonio, Texas performed the full-scale hydrostatic compression tests.

2.3.1. Testing Systems at Sandia National Laboratories

The Geomechanics Laboratory has three computer-controlled servo-hydraulic test systems, manufactured by MTS Systems Corporation (MTS). As shown in Table 2-7, the primary differences between the test systems is the maximum axial loads and confining pressures that can be applied during a test. In general, tests were run using the loading system best suited to meet the axial load and confining pressure requirements for that test.

Table 2-7. SNL test systems used in non-degraded surrogate waste compaction tests

Test System	Axial Force Range MN (kip)	Confining Pressure Vessel Range MPa (ksi)	Test Utilization
1.0 MN	0 - 1.0 (0 - 220)	0 - 100 (0 - 15)	• 1/4-scale uniaxial tests. • 1/4-scale hydrostatic and triaxial samples tested utilizing the 100 MPa pressure vessel.
1.0 MN AT (Axial Torsion)	0 - 1.0 (0 - 220)	– (–)	• 1/4-scale uniaxial tests.
5.0 MN	0 - 5.0 (0 - 1100)	– (–)	• Full-scale uniaxial tests. • Pressurization for 1/4-scale hydrostatic tests.

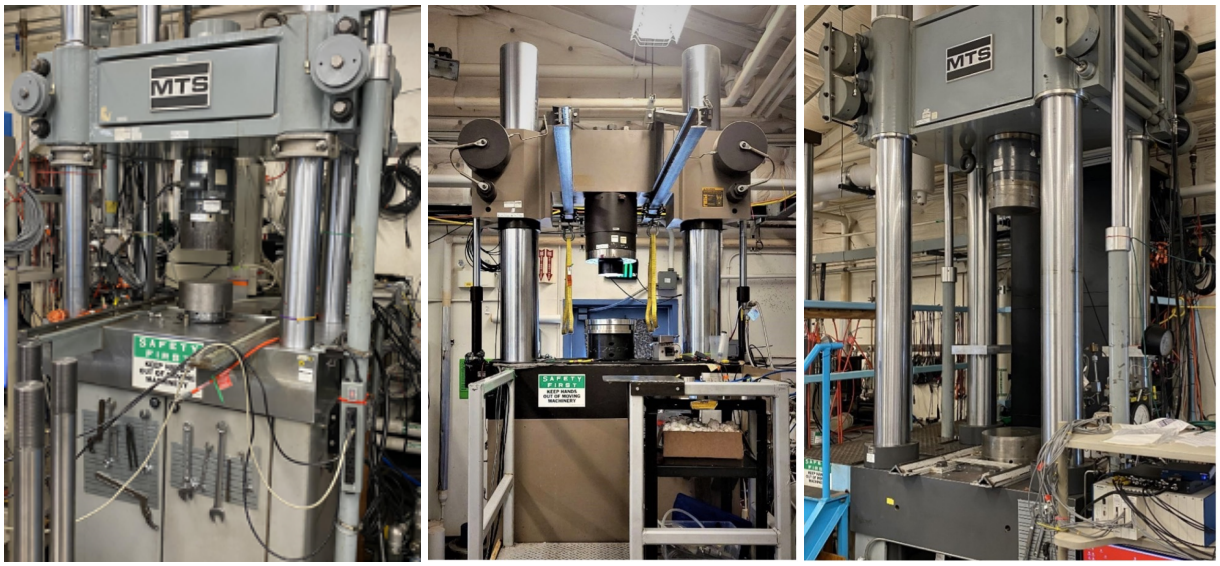

(a) 1.0 MN (220 kip) load frame

(b) 1.0 MN (220 kip) Axial Torsion (AT) load frame

(c) 5.0 MN (1100 kip) load frame

Figure 2-3. Photographs of the 1.0 MN (220 kip) load frame, the 1.0 MN (220 kip) Axial Torsion (AT) load frame, and the 5.0 MN (1100 kip) load frame.

The uniaxial 1/4-scale tests were performed using the MTS 1.0 MN (220 kip) and 1.0 MN (220 kip) Axial Torsion (AT) test systems (Figures 2-3a and 2-3b, respectively). Hydrostatic and triaxial 1/4-scale tests were performed using the MTS 1.0 MN (220 kip) test system (Fig. 2-3a). This system was used in conjunction with the 100 MPa (15 ksi) pressure vessel (Fig. 2-4a). For all successful 1/4-scale tests performed under confining pressure, the pressure in the pressure vessel was applied using a high-volume hydraulic piston (Fig. 2-4b) that was driven by the 5.0 MN (1100 kip) load frame (Fig. 2-3c). This high-volume piston reduced the need for restroking, which interrupts otherwise smooth pressure changes. The 5.0 MN load frame was also used to uniaxially compact the full-scaled 55-gallon drums.

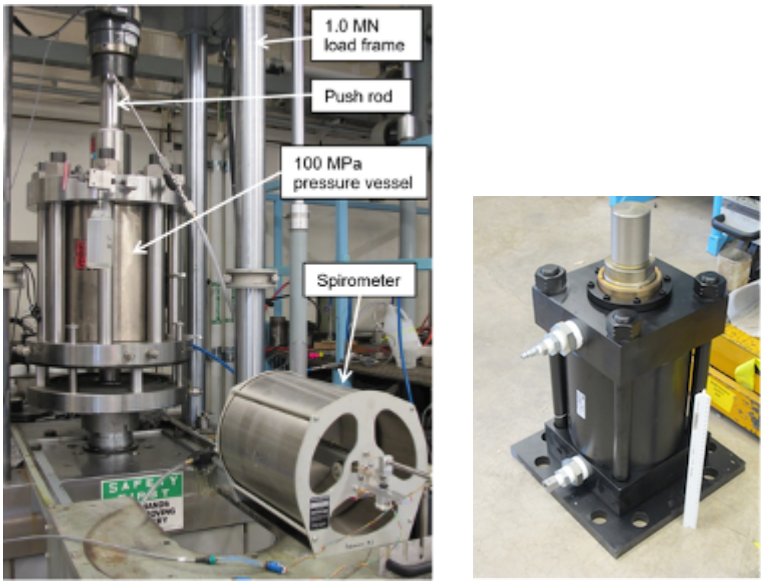

(a) 100 MPa pressure vessel and spirometer

(b) High-volume hydraulic piston

Figure 2-4. Photographs of the 100 MPa pressure vessel and spirometer installed in the 1.0 MN (220 kip) load frame and the high-volume hydraulic piston used to generate hydrostatic pressure for the 1/4-scale tests.

The MTS load frames used for all tests are equipped with movable crossheads to accommodate different specimen types and equipment geometries. Hydraulic actuators, located in the base of a particular load frame, can apply compressive axial forces over the ranges specified in Table 2-7. The axial force was measured by an electronic load cell mounted on the crosshead. The relative displacement of the load actuator was determined from a LVDT mounted in the actuator housing.

The sample volume change ΔV was assumed to be equivalent to the air volume change of the sample. The rate of air volume change was measured using either a spirometer or air flow meter. The air flow meter was used for the uniaxial compression tests performed at axial engineering strain rates of 10^{-4} sec^{-1} and all triaxial compression tests. The uniaxial compression tests performed at axial engineering strain rates less than 10^{-4} sec^{-1} used a spirometer in series with the flow meter for redundant flow rate measurements. The 1/4-scale hydrostatic compression tests used a spirometer for one test and used an air flow meter for the remaining tests.

The spirometer and air flow meters were selected because each can accurately measure the air flow rate from the sample with a near zero pressure drop across the measurement device. Fig. 2-4a shows the spirometer connected to the 100 MPa pressure vessel used for the 1/4-scale triaxial and hydrostatic tests. The volume of the spirometer was sufficiently large that a restroke was not needed for 1/4-scale experiments. The flow meters used in this study were the Alicat Scientific Whisper Series.

2.3.2. The Testing System at SwRI

(a) Pressure vessel exterior **(b) Pressure vessel interior**

Figure 2-5. Photographs of the 50-inch pressure vessel at SwRI: fully assembled vessel and vessel interior with a 55-gallon drum suspended in water from a test fixture.

The full-scale hydrostatic tests were conducted at the Marine Engineering Department of the SwRI in San Antonio, Texas. SwRI was chosen because they have pressure vessels large enough to apply 15 MPa (2175 psi) hydrostatic pressure to a 55-gallon drum and they operate under an NQA-1 compliant quality program (Orlowski, 2015). Our tests were performed in a 50-inch (127 cm) ID, 6000 psi (41 MPa) test chamber (Fig. 2-5). Tap water at ambient temperature was used as the confining pressure fluid. The test chamber was pressurized using two Haskel brand air pumps. A calibrated, 20.7 MPa (3000psi), pressure transducer was used to measure the fluid pressure inside the pressure vessel.

Each drum was suspended in the pressure vessel by a test fixture (Fig. 2-5b). A spirometer plumbed to the vent bung on the lid of the drum was used to measure air exiting/entering the sample during the unload/reload cycles. Fig. 2-6a shows the spirometer and data acquisition system (DAS) for the spirometer's linear variable differential transformer (LVDT). An underwater video camera located inside the pressure vessel monitored and recorded each drum's physical condition during testing (Fig. 2-6b).

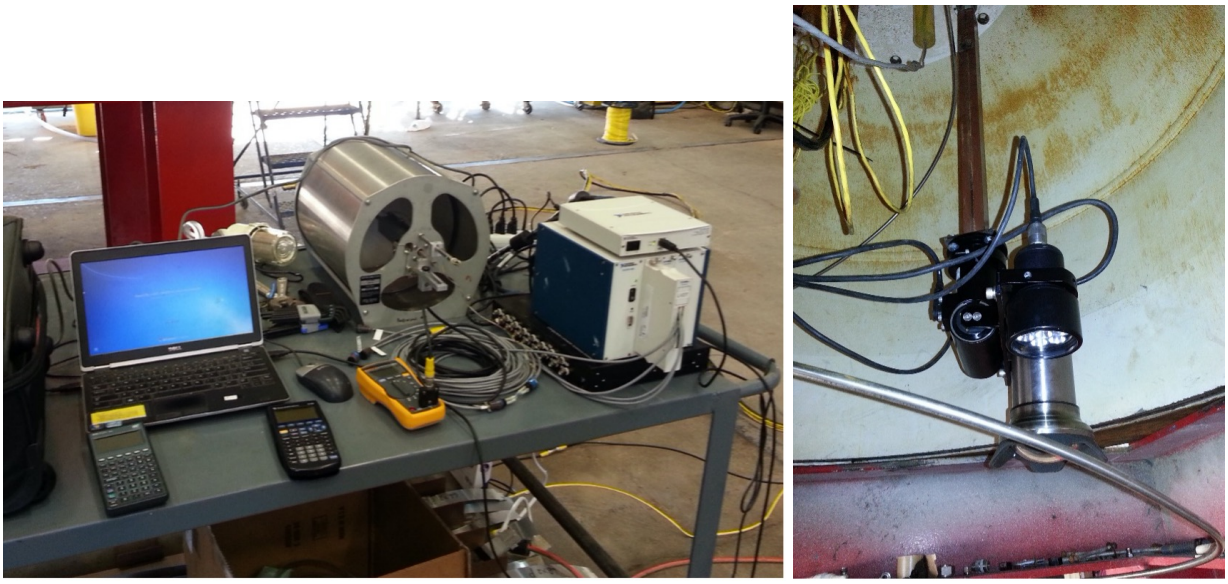

(a) Spirometer and data acquisition system **(b) Underwater video camera**

Figure 2-6. SwRI spirometer, data acquisition system, and underwater video camera inside the top of the pressure vessel.

2.4. Data Reduction

Depending upon the specific test, the data obtained by the data acquisition system included the axial force, axial displacement, confining pressure, air volume flow rate, and elapsed time. The voltage signal obtained by the data acquisition system (DAS) was converted to engineering units using standardized calibration sensitivity values, traceable to National Institute of Standards and Technology (NIST) standards. Engineering units were used to program the DAS, which was also used to control the load frames.

For this report, the traditional rock mechanics sign convention is used: compressive stresses and strains are taken as positive quantities and tensile stresses and strains are taken as negative quantities. Cauchy (or true) stress is denoted as σ and its conjugate logarithmic (or true) strain is denoted as ε. Engineering stress and engineering strain are denoted as s and e, respectively.

The axial engineering strain and axial logarithmic strain were respectively computed as

$$e_a = \frac{L_0 - L}{L_0} \tag{2.1}$$

$$\varepsilon_a = \ln\left(\frac{L_0}{L}\right) \tag{2.2}$$

in the uniaxial and triaxial compression experiments. The original length of each specimen L_0 can be found in Table 2-4, while the current length was computed as $L = L_0 - \Delta L$. The axial displacement of the specimen ΔL was not directly measured. Instead, it was computed as

$$\Delta L = \Delta L^{LVDT} - F_a / k_a, \tag{2.3}$$

where ΔL^{LVDT} is the axial displacement measured by the load frame linear variable differential transformer (LVDT), k_a is the load stack axial stiffness, and F_a is the axial force. The stiffness k_a was determined in the following manner. The crosshead was placed in a position similar to that used in the experiments. A steel billet with elastic modulus E^{sb}, length L^{sb}, and cross-sectional area A^{sb} was placed between the compression platens. The steel billet was compressed and unloaded, taking care to not plastically deform the billet, while measuring F_a vs. ΔL^{LVDT}. The axial displacement of the steel billet was computed as $\Delta L = F_a L^{sb}/(A^{sb} E^{sb})$. The stiffness k_a was then computed as the slope of a best fit line through the F_a vs. $\Delta L^{LVDT} - \Delta L$ measurements. This approach gave $k_a = 995$ kN/mm for the 1 MN load frame and $k_a = 2790$ kN/mm for the 5 MN load frame.

The volumetric engineering strain and volumetric logarithmic strain were respectively computed as

$$e_v = \frac{V_0 - V}{V_0} \tag{2.4}$$

$$\varepsilon_v = \ln\left(\frac{V_0}{V}\right) \tag{2.5}$$

in all experiments. The original volume of each specimen was computed as $V_0 = L_0 \pi D_0^2/4$, while the current volume was computed as $V = V_0 - \Delta V$. The change in volume ΔV was computed by integrating the flow rate measurements using the "cumtrapz" function in Matlab®.

Other measures of volumetric compaction, such as the current density ρ, solid volume fraction ξ, and current porosity ϕ were computed as

$$\rho = \frac{M}{V} \tag{2.6}$$

$$\xi = \frac{\rho}{\rho_s}, \tag{2.7}$$

$$\phi = 1 - \xi \tag{2.8}$$

where M is the mass of the specimen and the solid density ρ_s can be found in Table 2-3.

The lateral strain in the uniaxial and triaxial compression tests was inferred from the axial and volumetric strains because the asymmetric lateral deformation of the samples would have made direct, useful, lateral displacement measurements very difficult to near impossible to accomplish. The lateral logarithmic strain [1] was computed as

$$\varepsilon_l = \frac{\varepsilon_v - \varepsilon_a}{2}. \tag{2.9}$$

Calculating the lateral strain from the axial and volume strain provides a lateral strain that has been averaged over the sample volume, which is assumed to be sufficient for the purposes of developing a homogenized waste material model.

[1] Broome et al. (2016); Herrick (2020) incorrectly calculated the engineering lateral strain as $e_l = (e_v - e_a)/2$. This equation is only valid for small strains (less than roughly 8 %) and the strains are clearly large in the waste compaction experiments, so care was taken to use Eq. (2.9) to compute ε_l herein.

Each triaxial compression experiment began with a hydrostatic compression phase prior to triaxial loading. Occasionally, the strain relative to the hydrostatically compacted state was plotted in the following sections. The axial, volume, and lateral strains at the end of the hydrostatic compaction phase were respectively computed as

$$\varepsilon_a^h = \ln\left(\frac{L_0}{L_h}\right), \tag{2.10}$$

$$\varepsilon_v^h = \ln\left(\frac{V_0}{V_h}\right), \tag{2.11}$$

$$\varepsilon_l^h = \frac{\varepsilon_v^h - \varepsilon_a^h}{2}, \tag{2.12}$$

where L_h and V_h respectively were the specimen length and volume at the end of the hydrostatic phase.

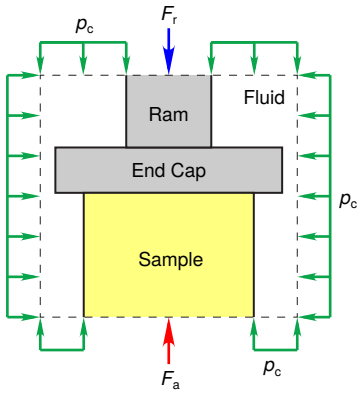

Figure 2-7. Free body diagram of ram (piston), end cap, sample, and fluid within triaxial cell.

The stresses were determined differently in each type of experiment. To calculate the axial stresses in the uniaxial and triaxial experiments, the sample's current cross-sectional area was computed as

$$A = \frac{V}{L} = \frac{V_0 - \Delta V}{L_0 - \Delta L}, \tag{2.13}$$

which treats the non-uniform container deformations as if they were affine, that is a cylinder deforms into a cylinder. The axial Cauchy stress in the uniaxial compression tests was computed as

$$\sigma_a = \frac{F_a}{A}, \tag{2.14}$$

where F_a was directly measured by the axial load cell. The axial force F_a experienced by the specimen in the triaxial experiments, by contrast, was computed from other measurements. Fig. 2-7 depicts a free body diagram of the axial loading ram (piston) with cross-sectional area $A_r = 4560$ mm^2, the sample end cap, the top part of the sample with cross-sectional area A, and confining fluid all inside the triaxial cell. The axial ram force F_r was measured by the load cell and the confining pressure p_c was measured by a pressure transducer. A force balance in axial direction gives

$$F_a = F_r + p_c\,(A - A_r)\,, \tag{2.15}$$

which was then used to compute the Cauchy stress difference as

$$\sigma_d = \frac{F_a}{A} - p_c = \frac{F_r - p_c A_r}{A}. \tag{2.16}$$

The pressure p in the hydrostatic tests was simply the pressure of the confining fluid $p = p_c$, measured by a pressure transducer.

Unload/reload cycles were performed at multiple points during compaction to measure elastic properties. Young's modulus E, Poisson's ratio ν, and the bulk modulus K were computed as

$$E = \frac{\Delta\sigma_a}{\Delta\varepsilon_a}, \tag{2.17}$$

$$\nu = -\frac{\Delta\varepsilon_l}{\Delta\varepsilon_a}, \tag{2.18}$$

$$K = \frac{\Delta p}{\Delta\varepsilon_v}, \tag{2.19}$$

where $\Delta\sigma_a$, Δp, $\Delta\varepsilon_a$, $\Delta\varepsilon_l$, and $\Delta\varepsilon_v$ are the change in axial Cauchy stress, Cauchy pressure, axial logarithmic strain, lateral logarithmic strain, and volumetric logarithmic strain during elastic unloading/reloading, respectively. These changes were typically computed by fitting a line to the most linear portion of the unloading curve. If the unloading curve did not have a clear linear region, then the two-point method was utilized. In the two point method, the upper point was where the reload data intersects the unload data and the lower point was the lowest stress measured during unloading. Using these two points effectively averages the slope of the unload/reload loop.

2.5. Uniaxial Compression Tests

Uniaxial compressions tests were conducted on both the 1/4-scale cans and full-scale 55-gallon drums. The initial set of uniaxial tests were conducted at an engineering axial strain rate of 10^{-4} sec^{-1}. These tests included five tests on 1/4-scale food cans and four tests on full-scale 55-gallon drums. Subsequent tests, which were performed at slower axial strain rates, used only 1/4-scale cans. These tests were carried out using engineering axial strain rates of 10^{-5}, 2.1×10^{-6}, and 10^{-7} sec^{-1} to characterize the surrogate waste material's strain rate dependence. Table 2-8 lists the samples, the container size, and the engineering strain rate at which the tests were conducted.

2.5.1. Jacketing of Uniaxial Compression Samples

Sections 2.1 and 2.2 described the surrogate waste, filling of the drums, and closing with lids to form an airtight seal. Once the containers were sealed, they were jacketed. For the uniaxial experiments, the purpose of the jacket was to keep the container sealed so that volumetric strain data, measured by a precision flow meter or spirometer, could be collected continuously throughout the duration of the test. The jacketing was assumed to not affect the mechanical

Table 2-8. The uniaxial compression test sample numbers, container size, and engineering strain at which the tests were conducted.

Sample	1/4- or full-scale	Axial Engineering Strain Rate (sec^{-1})
WC-UC-NDQ-01	1/4	1.0×10^{-4}
WC-UC-NDQ-02	1/4	1.0×10^{-4}
WC-UC-NDQ-03	1/4	1.0×10^{-4}
WC-UC-NDQ-04	1/4	1.0×10^{-4}
WC-UC-NDQ-05	1/4	1.0×10^{-4}
WC-UC-NDQ-10	1/4	1.0×10^{-5}
WC-UC-NDQ-11	1/4	1.0×10^{-5}
WC-UC-NDQ-12	1/4	1.0×10^{-5}
WC-UC-NDQ-13	1/4	1.0×10^{-5}
WC-UC-NDQ-14	1/4	2.1×10^{-6}
WC-UC-NDQ-15	1/4	2.1×10^{-6}
WC-UC-NDQ-16	1/4	2.1×10^{-6}
WC-UC-NDQ-17	1/4	2.1×10^{-6}
WC-UC-NDQ-18	1/4	1.0×10^{-7}
WC-UC-NDQ-19	1/4	1.0×10^{-7}
WC-UC-NDF-01	Full	1.0×10^{-4}
WC-UC-NDF-02	Full	1.0×10^{-4}
WC-UC-NDF-03	Full	1.0×10^{-4}
WC-UC-NDF-04	Full	1.0×10^{-4}

response of the sample. Different methods of jacketing were used based on the container and test type.

(a) Sample loading **(b) After jacketing**

Figure 2-8. Photographs of the 55-gal. drum, WC-UC-NDF-03, as loaded with surrogate waste material (left) and after jacketing with Smooth-On PMC®-770 (right).

The full-scale drums usually remained intact and did not split during the uniaxial tests, only forming small holes as they were compressed. Multiple coats of Smooth-On PMC®-770 urethane rubber was found to create a sufficient jacket. This coating remained flexible when dry and was found to have a negligible effect on the strength of the sample during compaction when compared to preliminary tests on full-scale drums without any coating. The jacket was able to remain intact across small holes in the sample that formed during compaction. Only one full scale sample, WC-UC-NDF-03, split along the seam in its side. An example of a full-scale drum filled with surrogate waste material and subsequently jacketed is shown in Fig. 2-8.

The 1/4-scale cans would consistently split open along their sides (see Fig. 2-9), requiring a different jacketing method. Initially no jacket was used for the first portion of the test. After a pre-determined amount of compaction, usually 50% of the can height, or when there was an abrupt decrease in the air flow exiting the can, indicating a breach in the can, the test was paused (Fig. 2-10a). The sample was covered with Van Aken Plastalina modeling clay (Fig. 2-10b). After that, a rubber sleeve was then rolled over the clay to hold it in place. The sleeve was taped to the top and bottom platens to produce an airtight seal (Fig. 2-10c). This method proved effective for most tests, but a few specimens still developed leaks (see Section 2.5.3).

Figure 2-9. Photographs of specimen WC-UC-NDQ-10 at the end of its test. The sample shows numerous large splits in the sample's side which occurs underneath the clay and rubber sleeve jacket.

Figure 2-10. Photographs of the jacketing of a $^1/_4$-scale uniaxial test specimen WC-UC-NDQ-10. (a) The sample is loaded until the can was breached. (b) The sample was covered in modeling clay. (c) The rubber sleeve was pulled up over the clay and tightly taped around the upper and lower platens to seal it.

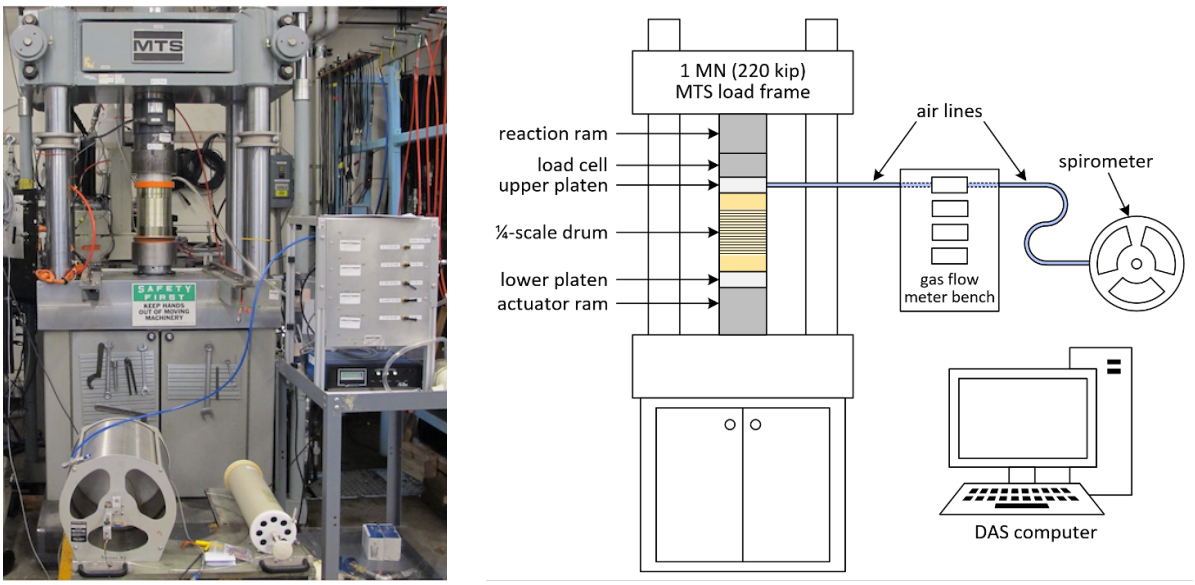

(a) Photo (b) Schematic

Figure 2-11. Photo and schematic of experimental setup for supplemental uniaxial compression tests. (Not all uniaxial tests utilized the 1 MN load frame shown in (a). See main text for further details.)

2.5.2. Uniaxial Compression Experimental Methods and Equipment

As discussed in Section 2.3.1, the SNL Geomechanics Lab has three computer-controlled servo-hydraulic test systems that were used for the testing of both the full-scale and 1/4-scale uniaxial samples. Fig. 2-11 is a photo and schematic of a typical experimental setup used in the tests. The 5 MN (1100 kip) load frame (Fig. 2-3c) was used for the full-scale uniaxial tests. It was needed to achieve the target axial stress of 15 MPa on the 55-gal. drums. The two 1.0 MN (220 kip) test systems were utilized for the 1/4-scale tests. All but the two slowest strain-rate 1/4-scale tests were performed on the 1.0 MN (220 kip) test system (Fig. 2-3a); the two slowest were performed on the 1.0 MN (220 kip) AT test system (Fig. 2-3b).

2.5.3. Uniaxial Compaction Testing Results

This section compares various uniaxial test results to each other without attempting to precisely portray the results from individual samples. The curves are occasionally plotted without the unloading/reloading curves to make the plot easier to read. Figures showing the individual curves for each uniaxial test, with unloading and reloading included, can be found in Section A.1.

An airtight seal was maintained on most uniaxial compression samples, but samples WC-UC-NDQ-02 and WC-UC-NDF-03 split excessively along the side wall of the sample during the tests. For these tests, volume strain and lateral strain were discarded once the sample's airtight seal was lost. The axial engineering stress and axial strain measurements would have been still useable because containers are expected to split open while compacted in a disposal room. This report, however, only presents Cauchy stresses and the axial Cauchy stress calculation depends on

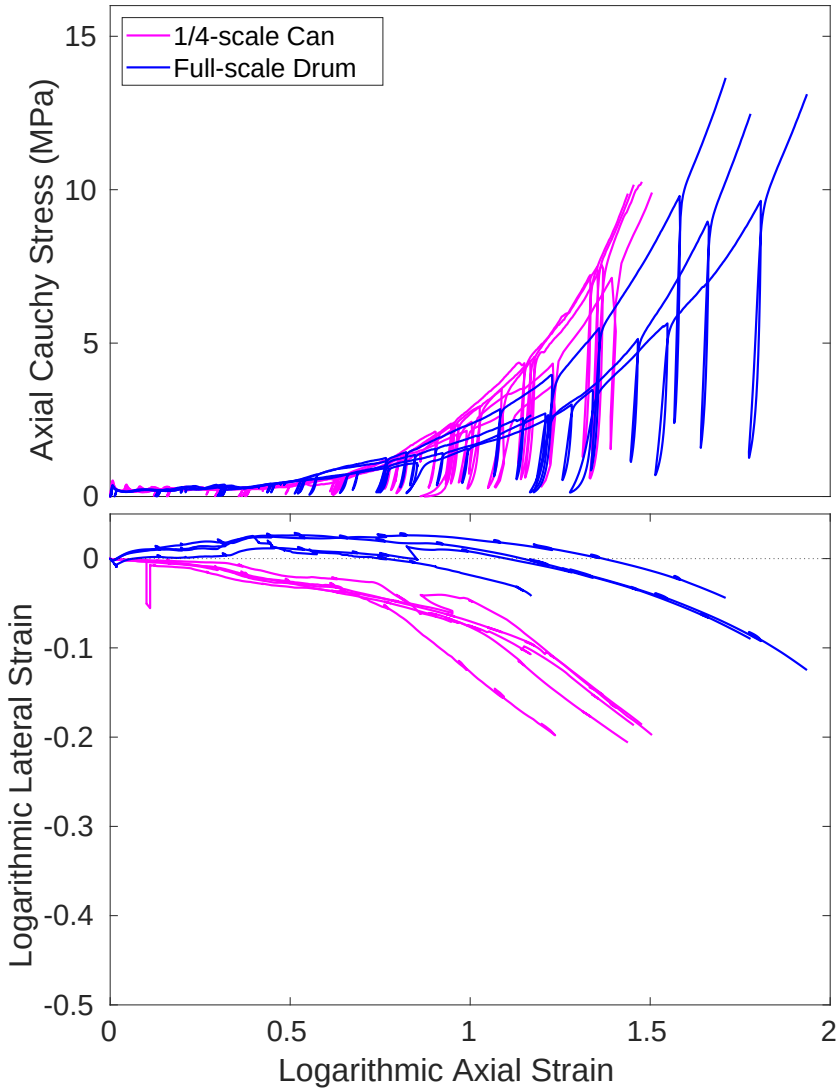

Figure 2-12. Comparison of uniaxial compression tests performed at the 10^{-4} sec^{-1} strain rate.

the volume strain through Eqs. (2.13) and (2.14), so no measurements after the breech are reported herein. The first 1/4-scale test done, WC-UC-NDQ-01, the volumetric data was recorded through the use of a 2 liter per minute flow meter. During the unload/reload cycle, the volume of air measured was near the minimum values of the meter's range. Therefore, for the second test, WC-UC-NDQ-02, it was decided that the volumetric measurements would be recorded with a spirometer. While the overall trend of the volumetric strain of WC-UC-NDQ-02 is quite similar to the other tests, during the unload/reload cycles, the change of volume was too small for the spirometer to accurately record. This uncertainty in the volumetric measurements of the second test negatively impacts the confidence of the Cauchy stress and lateral strain calculations for test WC-UC-NDQ-02. These curves are still included in figures of the uniaxial compression test results. The subsequent tests all used a 100 standard cubic centimeter per minute (SCCM) flow meter to capture the volumetric changes of the cans. The resolution of this meter was able to accurately capture the volume changes during the unload/reload cycles.

A comparison of typical axial stress versus strain curves for representative 1/4-scale and full-scale containers can be seen in Fig. 2-12. This figure is a composite of the axial Cauchy stress and logarithmic lateral strain plotted against the logarithmic axial strain for the uniaxial tests performed at the 10^{-4} sec^{-1} strain rate. The behavior of the two container types up until "lock-up" begins is quite similar. ("Lock-up" corresponds to when the waste begins to rapidly stiffen.) After the beginning of lock-up, the 1/4-scale responds with somewhat more axial stress, compared to the full-scale drum, for the same axial strain. Both the 1/4-scale and full-scale containers exhibit lateral expansion toward the end of each test, with the 1/4-scale displaying significantly more than the full-scale. The small lateral strains measured on the full-scale samples for $0 < \varepsilon_a < 1$ followed by significant lateral expansions for $\varepsilon_a > 1$ agree with the qualitative written description in Butcher et al. (1991, Section 3.3.2), which was briefly reviewed in Section 1.2. The difference is the specimens tested herein did not leak, so the lateral strain evolution was quantified and reported.

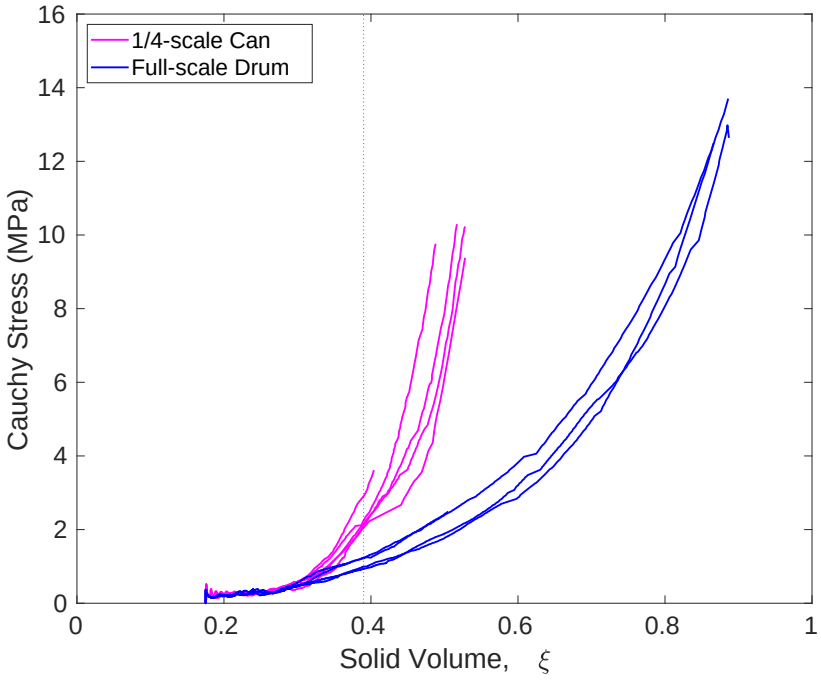

Figure 2-13. Cauchy stress versus solid volume fraction for full- and 1/4-scale uniaxial compression tests. The dashed vertical line is where $\xi = 0.39$ and is selected as the point at which the waste begins to substantially resist load.

The differences between the 1/4- and full-scale samples become more visible in Fig. 2-13, where Cauchy stress is plotted against ξ. The solid volume fraction ξ is a volumetric measure of compaction, so it incorporates both axial and lateral strains. The full-scale samples reach $\sigma_a > 1$ MPa at a greater axial compaction and smaller lateral expansion than the 1/4-scale samples in Fig. 2-12. Accordingly, switching from the 1/4- and full-scale samples caused the solid volume fraction required to reach $\sigma_a > 1$ MPa to increase significantly in Fig. 2-13.

Fig. 2-13 also helps one select the lock-up point. It is hard to determine a precise lock-up point since σ_a gradually builds with increasing ξ, but it was helpful to select practical lock-up value for

later analyses, so $\xi = 0.39$ was selected by visually inspecting Fig. 2-13. The vertical dashed line in the figure indicates $\xi = 0.39$.

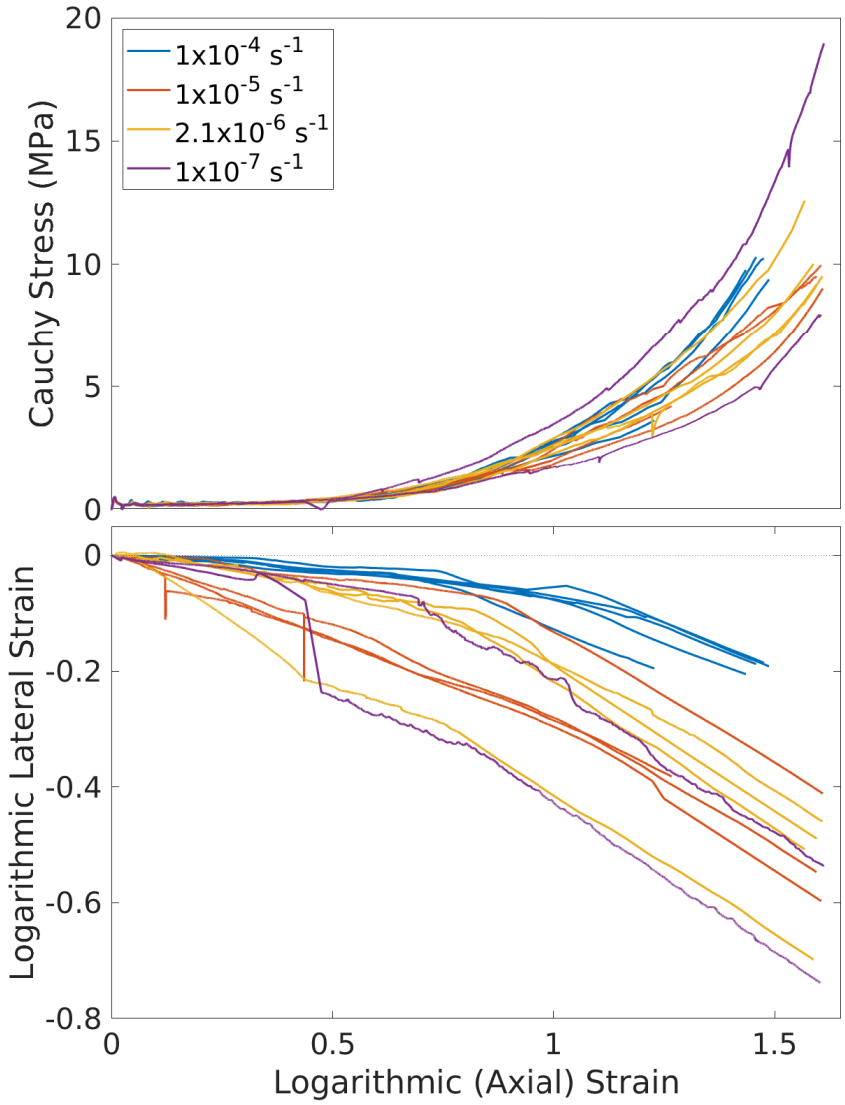

Figure 2-14. Comparison of 1/4-scale can uniaxial compression tests for all uniaxial tests performed at the varying strain rates.

Fig. 2-14 shows the effects of varying the strain rate for the uniaxial compression tests. The figure shows the results of all the 1/4-scale can tests performed at the four strain rates. Although it is difficult to see the trend due to the sample-to-sample variability, decreasing the strain rate appears to decrease the axial Cauchy stress slightly at a given logarithmic axial strain. Part of the variation that makes the trend hard to see is the curves with the smallest and largest stresses correspond to the two tests at the slowest 10^{-7} sec^{-1} strain rate. The lowest curve is considered reliable, while the upper curve is considered an outlier. During this upper curve test (WC-UC-NDQ-18) at 10^{-7} sec^{-1} strain rate, a steel pipe translated until it was vertical and parallel to the axis of the

applied load. This pipe likely carried the applied load and increased the axial stress above what would normally be expected. While a pipe could end up in a drum parallel to the axis of loading, it is not thought to be a common occurrence.

The calculated elastic properties as a function of density are represented graphically in Fig. 2-15. The logarithm of Young's modulus ($\log_{10}(E)$) increases linearly with increasing density for the full-scale specimens, but is slightly non-linear for the 1/4-scale specimens. For low densities, the 1/4- and full-scale Young's moduli agree well, but they diverge at higher densities. At ρ = 1.5 g/cc, the 1/4-scale Young's moduli are roughly 10× the full-scale values. The calculated Poisson's ratios range from -0.02 to 0.25 and do not seem to correlate with density or the scale of the specimen. As mentioned previously in this section, the volumetric changes recorded by the spirometer during the unload reload cycles for the second test were flawed and calls into question the calculation of the elastic properties due to the reliance on the volumetric strain in computing the values. The Young's modulus calculation for WC-UC-NDQ-02 are more reliable and are shown in Fig. 2-15. However, the calculated Poisson's ratios for this test are not reliable and are not included on the plot.

The differences between the 1/4- and full-scale Young's moduli at ρ = 1.5 g/cc and the variation in Poisson's ratio might appear concerning, but the elastic behavior is thought to be relatively unimportant compared to the inelastic behavior. The inelastic behavior dominates the compaction process, while the elastic behavior dominates the unloading that can occur after compaction if the gas pressure within the room is large enough to re-inflate the disposal room. When the room is expanding the waste assists the gas in pushing against the salt for a short period, but the waste's elastic stiffness is so large that it quickly unloads over a small displacement compared to the eventual increase in room volume due to the gas.

2.6. Triaxial Compression Tests

Triaxial compressions tests were conducted only on 1/4-scale No. 12 food cans. During the test, a constant confining pressure is applied to a cylindrical specimen while the axial load is increased. A total of seven triaxial compression tests were conducted. A listing of the triaxial test samples is listed in Table 2-9.

2.6.1. Jacketing of Triaxial Compression Samples

Sections 2.1 and 2.2 describe the surrogate waste and the filling and sealing of the containers. Once the samples were sealed, they were jacketed. The process of jacketing was usually similar to that of the hydrostatic tests and is described in Section 2.7.1. In this report, the sequence of presentation of the tests–uniaxial compression, triaxial compression, and hydrostatic compression–is done in the order in which it is thought that the waste is compacted in a disposal room closure. However, chronologically, the hydrostatic compression tests were conducted prior to the triaxial tests and the trial and error process of determining the best way of jacketing the samples was done during the hydrostatic compression tests. Therefore, the discussion of jacketing the triaxial test samples will be presented in the hydrostatic compression test section, Section 2.7.

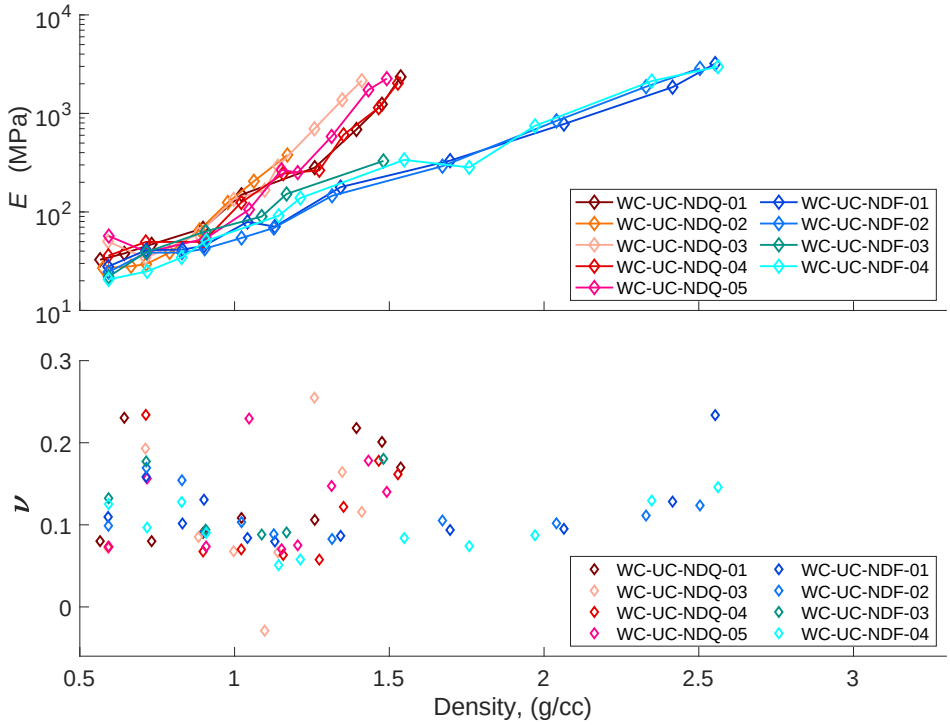

Figure 2-15. Young's modulus and Poisson's ratio versus density for uniaxial tests performed at $e_a = 10^{-4}$ 1/s.

Table 2-9. Listing of the triaxial compression test sample numbers and confining pressures at which the tests were conducted.

Sample	Confining Pressure (MPa)
WC-TX-NDQ-01-02	1.0
WC-TX-NDQ-01-03	1.0
WC-TX-NDQ-02-01	2.0
WC-TX-NDQ-02-03	2.0
WC-TX-NDQ-05-01	5.0
WC-TX-NDQ-15-02	15.0

The purpose of the jacket for triaxial tests was to keep the container sealed so that volumetric strain data could be collected throughout the duration of compaction process and to keep the confining fluid from penetrating into the sample.

2.6.2. Triaxial Compression Experimental Equipment and Testing Methods

Fig. 2-16 is schematic of the triaxial compression test setup. All triaxial tests were performed in the 1.0 MN (220 kip) MTS load frame (Table 2-7, Fig. 2-3a), which was used to apply the axial load. The 100 megapascal (MPa) (15,000 psi) pressure vessel was used to apply the confining pressure to the sample (Fig. 2-4a). The 5 MN (1100 kip) load frame (Fig. 2-3c) was used to control the large volume hydraulic piston shown in Fig. 2-4b. The hydraulic piston was used to apply and maintain the confining pressure in the pressure vessel.

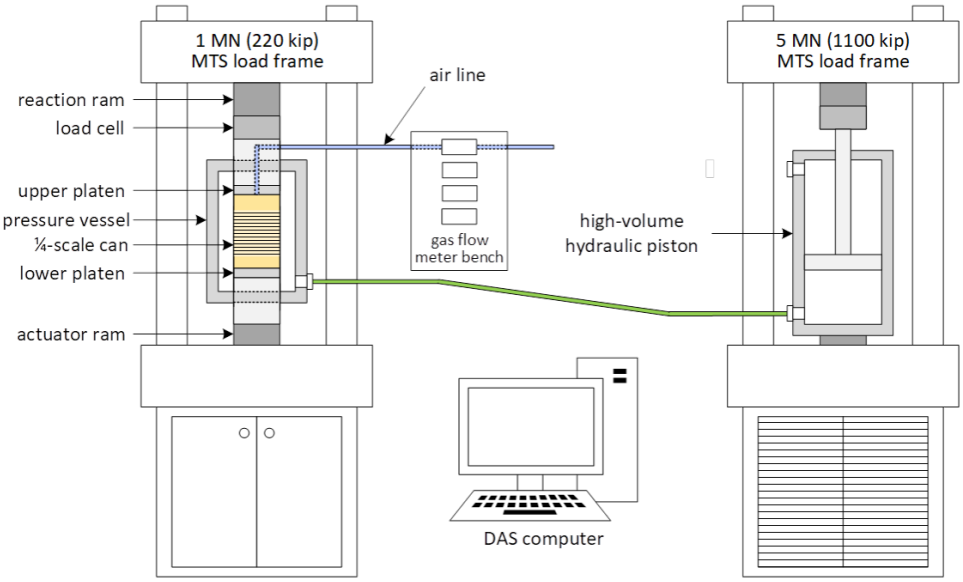

Figure 2-16. Schematic of experimental setup for triaxial compression tests.

Triaxial compression testing was performed using the following steps:

1. Increase confining pressure at a rate of $0.004 \leq \dot{p}_c \leq 0.008$ MPa/s to reach $p_c = 1$, 2, 5, or 15 MPa and then decrease back to $p_c = 0$. This initial compaction cycle was done without unload/reload loops to reduce the chance of jacket failure.
2. Attach flexible metal tubing to a nipple on top of sample to create a new vent port (see Fig. 2-17). The vent port was reconfigured to accommodate the end caps during the triaxial tests.
3. Place the compacted sample with vent port into an acrylic mold. Form endcaps using Hydro-Stone® gypsum cement (Figs. 2-17 and 2-18). Due to the significant deformation to the top and bottom surfaces of the cans during the hydrostatic loading portion of the test, an endcap was necessary to allow for a more uniform axial load.
4. Place the sample onto steel endcap inside the 100 MPa pressure vessel.

5. Place second steel endcap on top of sample (Fig. 2-18) and assembled pressure vessel.
6. Raise the confining pressure at a rate between $0.004 \leq \dot{p}_c \leq 0.02$ MPa/s to reach the value of p_c in Step 1. Hold the confining pressure constant for the remainder of the test.
7. Advance the 1 MN load frame actuator at an axial engineering strain rate of 10^{-4} sec^{-1} to apply an axial differential stress. Perform unload/reload loops to measure elastic properties at different levels of deformation.

Figure 2-17. Photograph of a pre-compacted sample in the acrylic mold with a vent port and flexible tubing attached to vent nipple on top of specimen. The white material below the sample is Hydro-Stone® gypsum cement.

2.6.3. Triaxial Compaction Testing Results

Similar to the uniaxial section, this section compares various triaxial test results to each other without attempting to precisely portray the results from individual samples. The curves are also plotted without the unloading/reloading curves to make the plot easier to read. Figures showing the individual curves for each triaxial test, with unloading/reloading included, can be found in Section A.2.

Seven triaxial tests were performed on 1/4-scale samples (see Table 2-9). No triaxial tests were conducted on full-scale drums. The test confining pressures were p_c =1, 2, 5, and 15 MPa. The p_c = 5 MPa sample, WC-TX-NDQ-05-01, developed a leak early in the test, so only the data before the breach was retained.

The differential stress, total logarithmic volumetric strain, and total logarithmic lateral strain (top, middle, and bottom subplots, respectively) plotted versus the total logarithmic axial strain, for all samples in which data was collected, are shown in Fig. 2-19. Fig. 2-20 shows the differential stress plotted versus the total volumetric strain. The total strains are computed based on the undeformed, non-compacted, can. The plot curves all begin at the point in which the triaxial compaction commences, that is after the cans have undergone hydrostatic compaction to the target confining pressure. (See Section 3.3 for plots relative to the hydrostatically compacted state.) These plots

Figure 2-18. Specimen WC-TX-NDQ-15-02 before compaction (left), after hydrostatic compaction at 15 MPa and with Hydro-Stone® formed endcaps molded on (middle), and after 27% axial strain during triaxial compression (right). Upper and lower steel endcaps are visible.

clearly demonstrate the effect of the different confining pressures, with higher confining pressures correlating to higher total volumetric strain, higher lateral strain, and higher stiffness.

The calculated elastic properties as a function of density are represented graphically in Fig. 2-21. The starting value of $\log_{10}(E)$ from each test appears to linearly correlate with density, but the correlation worsens once significant stress differences are applied. The calculated Poisson's ratios range from 0.18 to 0.69, and generally increase with increasing densities. Values above 0.5 might appear concerning because Poisson's ratio must be within $-1 \leq \nu \leq 0.5$ for isotropic materials, but no such bounds exist for anisotropic materials (Ting and Chen, 2005). Non-isotropic (non-hydrostatic) compaction of the waste containers likely induces significant anisotropy, so the calculated Poisson's ratios greater than 0.5 in Fig. 2-21 may, in fact, be reasonable values.

2.7. Hydrostatic Compression Tests

Hydrostatic compression tests were conducted on both 1/4-scale cans and full-scale 55-gallon drums. The 1/4-scale cans were tested in the Geomechanics Laboratory in Sandia National Laboratories and the full-scale 55-gallon drums were tested at the Southwest Research Institute (SwRI) in San Antonio, Texas. A list of the hydrostatic compression sample numbers, sample scale, and associated comments can be found in Table 2-10.

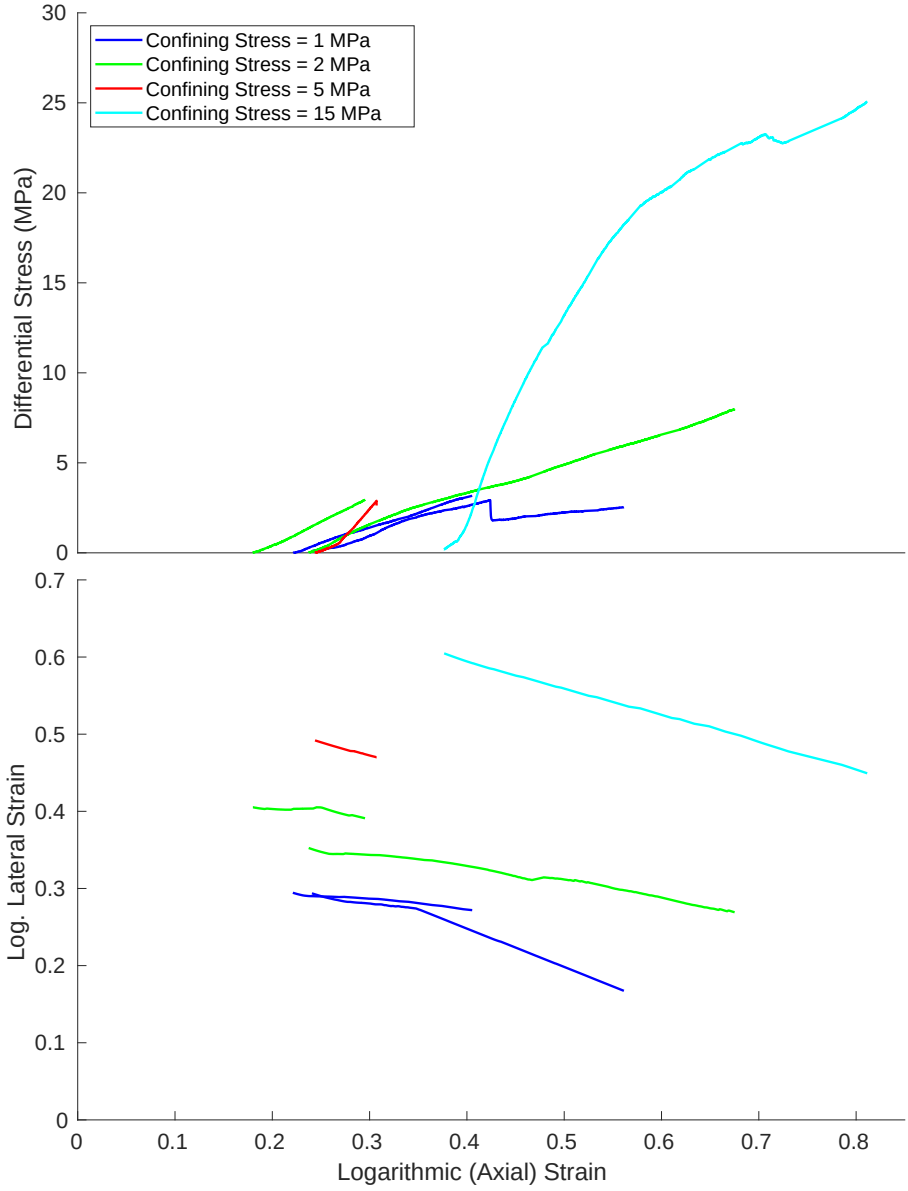

Figure 2-19. Triaxial compression test results, after the initial hydrostatic phase, plotted against axial strain. All strains are relative to the undeformed cans.

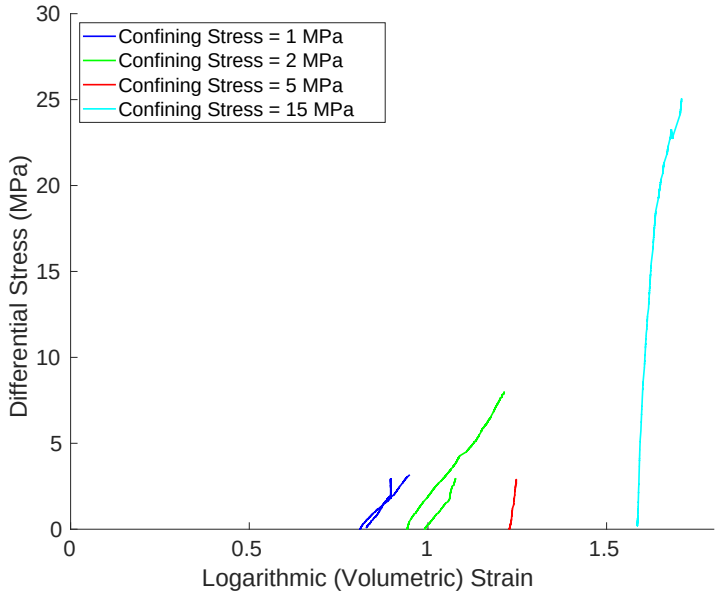

Figure 2-20. Triaxial compression test stress differences, after the initial hydrostatic phase, plotted against volumetric strain. The volume strains are relative to the undeformed cans.

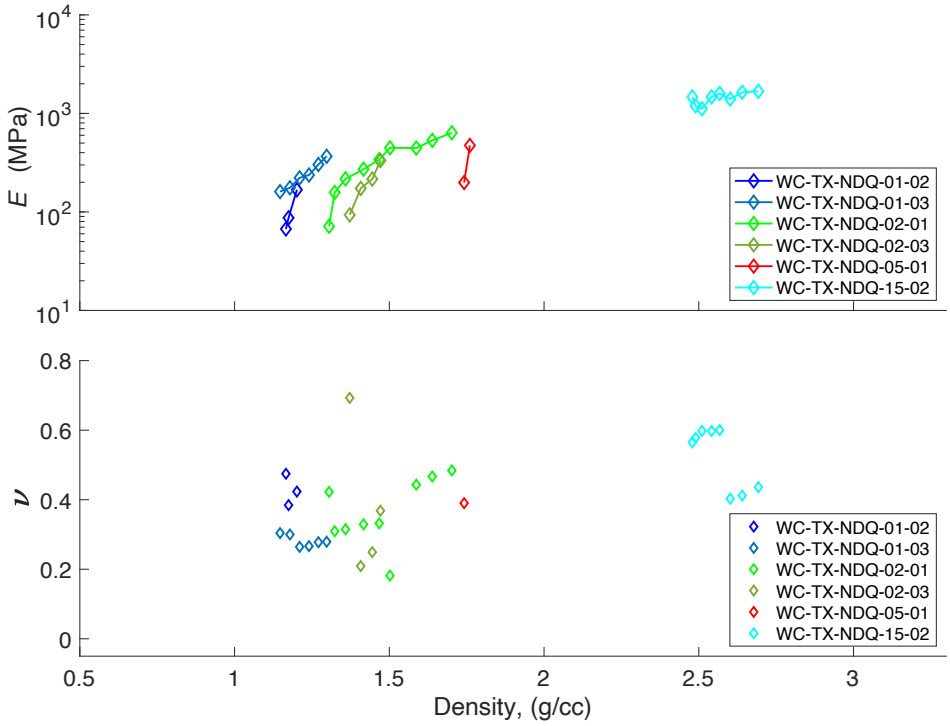

Figure 2-21. Young's modulus, E, and Poisson's ratio, ν, versus density for all triaxial tests.

Table 2-10. Hydrostatic compression tests.

Sample	1/4- or full-scale	Comments
WC-HC-NDQ-01	1/4	Leaked at 4.4 MPa
WC-HC-NDQ-02	1/4	–
WC-HC-NDQ-03	1/4	Clogged vent at 10.3 MPa
WC-HC-NDQ-04	1/4	Clogged vent at 2.7 MPa
WC-HC-NDF-01	Full	Leaked at 0.8 MPa
WC-HC-NDF-05	Full	Leaked at 0.7 MPa
WC-HC-NDF-06	Full	Leaked at 5.0 MPa
WC-HC-NDF-07	Full	Leaked at 5.8 MPa

2.7.1. Jacketing of Hydrostatic Compression Samples

The manner in which the cans/drums were filled with the surrogate waste and specimens prepared is discussed in Sections 2.1 and 2.2. Once the lids were sealed, the samples were jacketed. Depending on drum type, different methods were used in the jacketing process. Similar to the triaxial tests, the jacket in the hydrostatic tests was intended to prevent air from escaping without going through the spirometer/air flow meter and to keep the confining fluid from penetrating into the sample.

The full-scale drums were jacketed first with Kevlar® and then with rubber coatings. Kevlar® was used to prevent surrogate waste or container material from protruding through as the container was subjected to external pressure. Since Kevlar® has virtually no bending strength, it was deemed an acceptable jacket material for both hydrostatic and triaxial testing. Smooth-On PMC®-770 industrial liquid urethane rubber was brushed on over the Kevlar® to help it adhere to the drum (Fig. 2-22). A second Smooth-On brushable urethane product, Brush-On®-40, was then applied in multiple coats over the entire drum.

Jacketing the 1/4-scale hydrostatic test samples was a somewhat iterative process after some of the initial samples sprung leaks during their tests. The first two hydrostatic test samples, WC-HC-NDQ-01 and WC-HC-NDQ-02, were jacketed with three layers of Loctite® SF F720 tough rubber coating, also known as Loctite® Color Guard Coating. Kevlar® sheets were laminated on the surfaces of the can between the coats of Loctite® SF F720. Four rubber sleeves were placed around these first two samples. These sleeves were sealed using a vacuum pump and Loctite® SF F720 near the nipple flange interface on the top of the can. A sample covered with Kevlar® sheets and the application of rubber sleeves are shown in Fig. 2-23. For the final two 1/4-scale hydrostatic tests, specimens WC-HC-NDQ-03 and WC-HC-NDQ-04, the rubber sleeves were replaced with PMC®-770 urethane rubber (Fig. 2-24). It was thought that using PMC®-770 would provide a better seal at the nipple protrusion.

As mentioned in Section 2.6.1, most triaxial specimens were jacketed in a similar manner to the hydrostatic specimens. The p_c = 1 MPa triaxial tests were only coated with PMC®-770 urethane

Figure 2-22. Photographs of the jacketing process for full-scale drums to be tested under hydrostatic conditions. A new drum with no jacketing (left), a drum wrapped in Kevlar® and coated with one layer of PMC®-770 (center), and a finished sample with multiple coats of Brush-On®-40 applied (right).

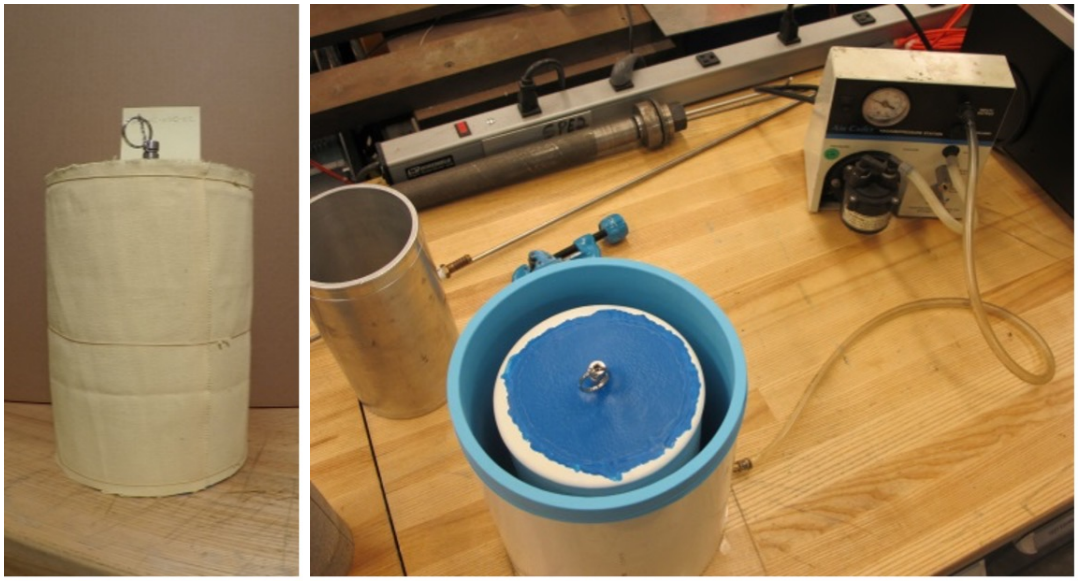

Figure 2-23. Photographs of a 1/4-scale hydrostatic sample showing Kevlar® sheets wrapped around a Loctite® SF F720 coated sample (left) and the method of sleeve installation using vacuum pump (right).

Figure 2-24. Photograph of a 1/4-scale hydrostatic sample being coated with PMC®-770 urethane rubber over the three coats of Loctite® SF F720 and two layers of Kevlar® sheets.

rubber. After breaches formed in the sides of these PMC®-770 jacketed samples, the WC-TX-NDQ-02-01 sample received a jacket composed of a Loctite® SF F720 / Kevlar® / Loctite® SF F720 / Kevlar® / Loctite® SF F720. All further triaxial samples received a Loctite® SF F720 / Kevlar® / Loctite® SF F720 / Kevlar® / Loctite® SF F720 / PMC®-770 jacket similar to WC-HC-NDQ-03 and -04. The WC-TX-NDQ-15-02 sample also had four rubber sleeves added. Trial triaxial tests without Kevlar® and Loctite® SF F720 produced nearly identical pressure versus volume strain responses, before leaks formed, to those with jacketing, indicating that the jacket did not affect the hydrostatic loading phase. The jacket probably did not significantly restrain the lateral expansion of the drum during the deviatoric loading phase either since the total (net) lateral strain was still compressive for all confining pressures in Fig. 2-19.

2.7.2. Hydrostatic Compression Testing Methods

2.7.2.1. Full-Scale Hydrostatic Compression Tests

The full-scale hydrostatic tests were performed in SwRI's 50-inch (127 cm) ID, 6000 psi (41 MPa) test chamber (Fig. 2-5) using fresh tap water at ambient temperature as the confining pressure fluid. The tests consisted of subjecting each drum to a series of pressure load/unload/reload loops to measure bulk modulus at various stages of the compaction process. Section 2.3.1 describes the testing system in more detail.

The full-scale hydrostatic tests were pressurized using two Haskel brand air pumps, which applied a volumetric engineering strain rate of approximately $\dot{e}_v = 10^{-4}$ sec^{-1}. When the engineering volume strain was approximately 37 %, the second, larger air pump was used to apply the pressure at $\dot{p} = 0.6$ MPa/min. Note that the volumetric strain rate likely deviated from $\dot{e}_v = 10^{-4}$ sec^{-1} when the pressurization rate was controlled. Unload/reload pressure loops were performed at the

intervals given in Table 2-11. Values in the green-shaded cells are the target values, while the non-shaded cells are the corresponding approximate observed values for 1/4-scale and full-scale samples.

Table 2-11. Criterion for performing an unload/reload loop for hydrostatic tests.

Engineering Volume Strain	Confining Pressure (MPa)	(psi)
0.12	≈ 0.07	10
0.24	≈ 0.10	15
0.36	≈ 0.21	30
≈ 0.39	0.34	50
≈ 0.47	0.69	100
≈ 0.53	1.38	200
≈ 0.58	2.76	400
≈ 0.61	5.52	800
≈ 0.65	10.34	1500
≈ 0.67	15.00	2175

Care was taken to avoid inelastically deforming the sample while filling the pressure vessel with water. The drum noticeably compacts with as little as 1 kPa (0.15 psi) of pressure, so at least one port on top of the pressure vessel was left open to the atmosphere. At SwRI, this necessitated using a dipstick to constantly check the water level in the pressure vessel during filling. When it was determined the pressure vessel was nearly full, the vessel fill rate was substantially slowed down. Once water was observed coming out from the vent port on top of the pressure vessel, the source valve was closed, and the water was allowed to stop flowing before the vent port was plugged to minimize an increase in vessel pressure. During the filling process, spirometer readings were monitored for premature drum crush.

A premature leak of the first full-scale drum prompted an investigation of the failure mode. Visual observation of a preliminary test and the first test indicated that the drums seemed to prefer to collapse on three planes that were fairly evenly spaced around the circumference of the drum. Two of the three planes are shown in Fig. 2-25a, where a solid black line partially defines each mostly vertical plane. If the vent bung was in the middle of one of those planes, compaction near the lid tended to push the bung out of the lid and create a leak in the sample (Fig. 2-25a). In order to force the bung to be located within the shaded circular region in Fig. 2-25a, where it would remain open to unimpeded air flow, three buckling points were induced on the next sample. The desired buckling points in Fig. 2-25b are shown with arrows on the top lid of the sample. A gentle tap with a rubber mallet created a slight dent at three points on the sample coinciding with the arrows drawn on the lid (one dent is shown). The dents controlled the location of the buckling planes, causing the vent to be located at the junction of two buckling planes. There was concern the pre-induced buckling (dents) before the test would adversely affect the deformation behavior, but

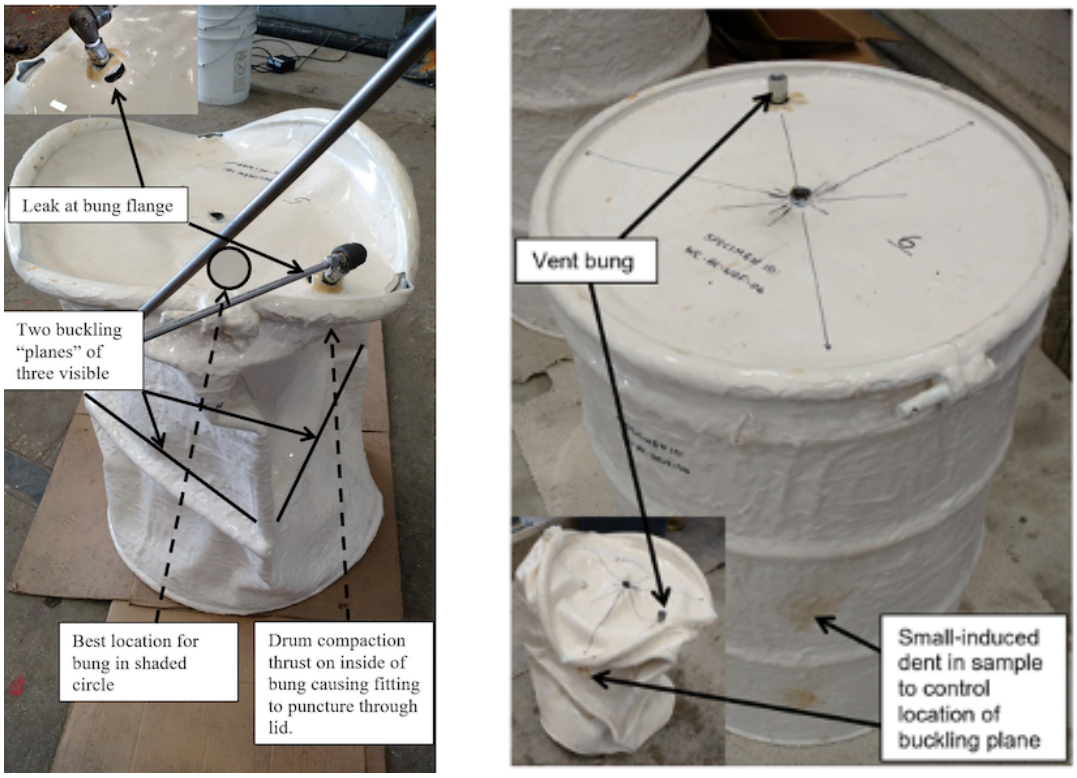

(a) Sample with premature vent bung failure

(b) Pre-test dented sample without premature vent bung failure

Figure 2-25. Full-scale hydrostatic samples with and without premature vent bung failure.

it proved to be nearly the same as samples which did not have pre-existing dents. The pre-induced buckling technique was used on all subsequent full-scale tests.

2.7.2.2. ¼-Scale Hydrostatic Compression Tests

Hydrostatic compression tests on ¼-scale cans in the Geomechanics Laboratory were performed in the 1 MN (220 kip) load frame (Fig. 2-3a) using the 100 MPa pressure vessel (Fig. 2-4a) to constrain the confining pressure. Fig. 2-4a shows the spirometer connected to the pressure vessel used for the ¼-scale hydrostatic tests. A large hydraulic piston (Fig. 2-4b) driven in the 5 MN load frame (Fig. 2-3c) was used to generate up to 15 MPa confining pressure. This system was used to apply an engineering volume strain rate on the can of 10^{-4} sec^{-1}.

As mentioned in the previous section, it is critical to fill the pressure vessel in a manner such that the sample is not deformed by the pressure generated during the filling process. To keep the pressure in the confining fluid as low as possible, shop air was used to pressurize a reservoir filled with silicon oil, the confining fluid used in the ¼-scale experiments. The shop air was set to approximately 5 psi and the top valve on the pressure vessel was left open. When fluid was observed exiting the top valve, the shop air was disconnected, and the valve was closed.

2.7.3. Hydrostatic Compaction Testing Results

Figure 2-26. Photographs of 1/4-scale (top row) and full-scaled (bottom row) post-test hydrostatically compacted samples.

Similar to previous sections, this section compares hydrostatic test results to each other without attempting to precisely portray the results from individual samples. Figures showing the individual curves for each hydrostatic test on each sample can be found in Section A.3.

Four hydrostatic tests were performed on full-scale 55-gallon drums and four tests were performed on the 1/4-scale cans. Fig. 2-26 shows photographs of all the post-test hydrostatic samples for both 1/4-scale and full-scale. Sample WC-HC-NDQ-02 (top row, second from left) is shorter because that sample was additionally used for a triaxial test, named WC-TX-NDQ-10-01 [2].

The final confining pressure goal was 15 MPa (2175 psi), but only one hydrostatic sample (WC-HC-NDQ-02) did not leak or develop a clogged vent port. For example, a leak at 0.8 MPa in sample WC-HC-NDF-01 caused an increase in volume strain without an increase in pressure. In addition, the vent ports in samples WC-HC-NDQ-03 and WC-HC-NDQ-04 clogged at 10.3 and 2.7 MPa confining pressure, respectively, resulting in an increase in pressure without an increase

[2] WC-HC-NDQ-02 successfully reached $p = 15$ MPa without any leaks, so the sample was going to be re-used in a triaxial test with $p_c = 15$ MPa confining pressure. During the hydrostatic phase of the triaxial test, however, the sample developed a slow leak at around 10 MPa. Rather than just abandon the test, the sample was triaxially compacted at $p_c = 10$ MPa as a practice test, which was named WC-TX-NDQ-10-01. The results from WC-TX-NDQ-10-01 are not included herein because the sample experienced $p = 15$ MPa before being triaxially compacted at $p_c = 10$ MPa and the slow leak raised questions about the volume strain measurements.

in volume strain. The experimental measurements after these failures were removed so as to not distract the reader.

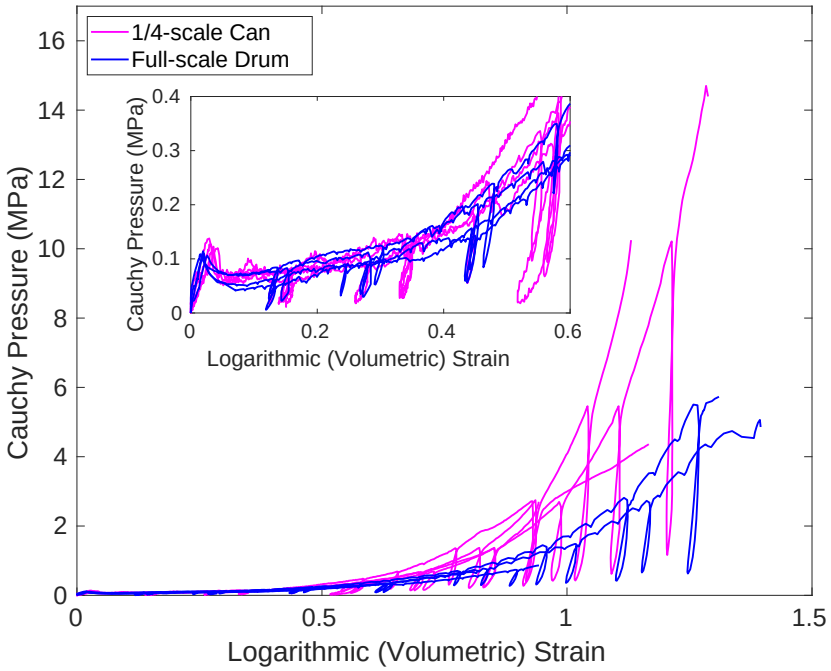

Figure 2-27. Mechanical responses from 1/4-scale and full-scale hydrostatic compression experiments.

A plot of the Cauchy pressure versus Logarithmic volumetric strain for all the hydrostatic compression tests is shown in Fig. 2-27. The plot illustrates the sample-to-sample consistency within scale and the differences between the1/4- and full-scale samples. The two begin to deviate beginning at 50 % volume strain, such that the 1/4-scale samples achieved higher pressure for a given volumetric strain than the full-scale samples. The deviation is probably due to differences between the 1/4-scale and full-scale specimens, but a small part could be due to changing control modes in the full-scale tests, which occurred at $\varepsilon_v \sim 44$ % (see Section 2.7.2.1). The inset plot in Fig. 2-27 is zoomed in to show the comparison of initial buckling pressure and the start of lock-up, when the pressure begins to rise rapidly. The 1/4-scale and full-scale samples show similar behavior up until that time.

Fig. 2-28 shows that the logarithm of the bulk modulus ($\log_{10}(K)$) scales nearly linearly with density for all hydrostatic tests. As mentioned in Section 2.5.3, the elastic behavior is considered less important than the inelastic behavior.

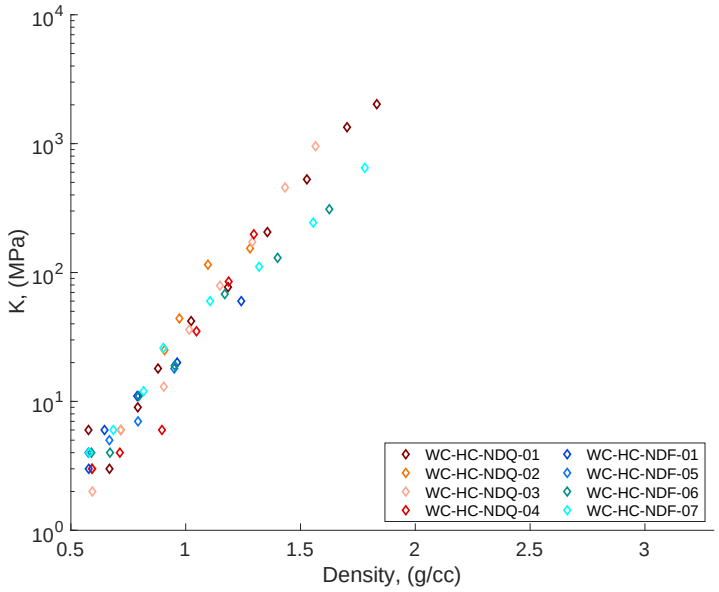

Figure 2-28. Bulk modulus versus density for all hydrostatic compression tests.

3. WASTE COMPACTION MODEL

This chapter describes the development of a new waste material model. Similar to Butcher et al. (1991); Butcher (1997a); Stone (1997a), the new waste material model does not explicitly model the individual waste constituents within each 55-gallon container. Instead, the entire container is homogenized into a single waste material whose behavior is obtained by calibrating a constitutive model against the experimental measurements. Unlike Butcher et al. (1991); Butcher (1997a); Stone (1997a), the new model calibration is based on current estimates of waste composition and initial porosity, it does not rely on combining the oedometric response of each constituent using a mixture rule, and it does not utilize uncertain assumptions about the stress state within the oedometer. Moreover, the uniaxial, triaxial, and hydrostatic experiments probed the waste response over a wider array of stress states, and measured (or inferred) all relevant homogenized strain and stress components while compacting the containers. In addition, the Foam Damage (FD) model, the constitutive model at the core of the waste material model, has a more flexible formulation than the soil and crushable foam model (SAF) constitutive model discussed in Chapter 1. As will be shown in this chapter, these superior experiments and more flexible constitutive model enabled an improved waste material model compared to the legacy model developed in Butcher et al. (1991); Butcher (1997a); Stone (1997a). All files associated with developing this new waste material model are archived at `/data/cvs/CVSLIB/WIPP_EXTERNAL/ap180_files` on Sandia Carlsbad's Linux Server.

The remainder of this chapter is organized as follows: Section 3.1 describes the FD constitutive model, Section 3.2 discusses the calibration of the FD constitutive model against the experiments, Section 3.3 compares the legacy and new waste material models against the experiments, Section 3.4 uses the new model in a disposal room simulation, and Section 3.5 explores the behavior of the legacy and new model behavior under plane strain conditions.

3.1. Foam Damage Constitutive Model

The FD model (Neilsen et al., 2015) was developed for simulating the mechanical behavior of stiff foams, which compact in a manner similar to standard waste containers. Both are characterized by large initial porosities, large plastic deformations, and relatively small elastic rebound. Once much of the porosity has been crushed, both "materials" begin to stiffen significantly. The FD model's damage formulation is designed to capture tensile failure of stiff foams, which is not of interest herein. Four aspects of the FD model are more flexible than the SAF model: (1) one can specify a deviatoric hardening function, (2) the flow direction varies with porosity ϕ, (3) the flow direction varies with the shape of the yield surface, and (4) the model includes strain rate dependence. A thorough description of the FD model development and formulation can be found in Neilsen et al. (2015), but this section presents the parts of the model relevant to the capturing the waste

compaction behavior. The temperature dependence and damage formulation, for example, are discussed in Neilsen et al. (2015), but they do not help model the waste compaction behavior, so they are omitted herein. The FD model is implemented in Sierra/SolidMechanics (2022) version 5.4.1, which was used in the simulations presented herein.

3.1.1. Formulation

A few preliminaries bear mentioning. First, compressive strains and stresses are treated as positive. Second, this section presents the model in an infinitesimal strain setting for simplicity, so there is no distinction between various stress measures or various strain measures. Although not shown herein, the model is later extended into the finite deformation realm using Sierra/SolidMechanics (2022)'s hypoelastic framework. In this framework, the stress $\boldsymbol{\sigma}$ becomes the Cauchy stress and the total strain rate $\dot{\boldsymbol{\varepsilon}}$ becomes the un-rotated rate of deformation. In the absence of rotations, the un-rotated rate of deformation is equivalent to the logarithmic strain rate.

The FD model uses the following simple additive decomposition of the total strain rate into elastic parts and inelastic parts:

$$\dot{\boldsymbol{\varepsilon}} = \dot{\boldsymbol{\varepsilon}}^e + \dot{\boldsymbol{\varepsilon}}^{in}. \tag{3.1}$$

Several parts of the model depend on the maximum solid volume fraction $\xi = 1 - \phi$, which the model computes from the initial solid volume fraction ξ_0 and the volume strain.

The elastic behavior utilizes generalized Hooke's law in rate form to relate $\dot{\boldsymbol{\varepsilon}}^e$, the fourth-order isotropic elastic stiffness tensor $\mathbb{E}$, and the stress rate $\dot{\boldsymbol{\sigma}}$:

$$\dot{\boldsymbol{\sigma}} = \dot{\mathbb{E}} : \boldsymbol{\varepsilon}^e + \mathbb{E} : \dot{\boldsymbol{\varepsilon}}^e \tag{3.2}$$

$$\mathbb{E} = (k - \tfrac{2}{3}\mu)\, \boldsymbol{I} \otimes \boldsymbol{I} + 2\mu \mathbb{I}, \tag{3.3}$$

where k is the bulk modulus, μ is the shear modulus, $\boldsymbol{I}$ is the second-order identity tensor, and $\mathbb{I}$ is the fourth-order symmetric identity tensor[1]. The bulk and shear moduli are related to Young's modulus E and Poisson's ratio ν as

$$k = \frac{E}{3\,(1-2\,\nu)} \tag{3.4}$$

$$\mu = \frac{E}{2\,(1+\nu)}. \tag{3.5}$$

Both Young's modulus and Poisson's ratio vary with ξ:

$$E = E_r\, E_\xi \tag{3.6}$$

$$\nu = \nu_r\, \nu_\xi, \tag{3.7}$$

[1] Neilsen et al. (2015) incorrectly quotes generalized Hooke's law in rate form as $\dot{\boldsymbol{\sigma}} = \mathbb{E} : \dot{\boldsymbol{\varepsilon}}^e$, which neglects the $\dot{\mathbb{E}} : \boldsymbol{\varepsilon}^e$ term shown in Eq. (3.2). This mistake, however, is only a typographical error (Neilsen, 2022), since the FD model numerical implementation in Sierra/SolidMechanics (2022) is consistent with Eq. (3.2).

where E_r and ν_r are material constants, and $E_\xi = E_\xi(\xi)$ and $\nu_\xi = \nu_\xi(\xi)$ are user-defined functions of ξ.

Inelastic strain evolves when the stress state is on or exceeds the yield surface. The yield surface is an ellipsoid defined as

$$\frac{\bar{\sigma}^2}{a^2} + \frac{p^2}{b^2} - 1 = 0, \tag{3.8}$$

where:

- $a > 0$ and $b > 0$ are the deviatoric (or shear) and volumetric (or hydrostatic) strengths, respectively, and are user-defined functions of ξ, i.e. $a = a(\xi)$ and $b = b(\xi)$.
- $p = \mathrm{tr}(\boldsymbol{\sigma})/3$ is the pressure
- $\bar{\sigma} = \sqrt{\frac{3}{2}\boldsymbol{\sigma}^{dev} : \boldsymbol{\sigma}^{dev}}$ is the von Mises stress and $\boldsymbol{\sigma}^{dev} = \boldsymbol{\sigma} + p\,\boldsymbol{I}$ is the deviatoric stress.

One can rearrange Eq. (3.8) into the following yield function,

$$\varphi = \sigma^* - a = 0, \tag{3.9}$$

where the effective stress σ^* is defined as

$$\sigma^* = \sqrt{\bar{\sigma}^2 + \frac{a^2}{b^2}p^2}. \tag{3.10}$$

The model formulation then uses a Perzyna-type formulation to calculate the inelastic strain rate $\dot{\boldsymbol{\varepsilon}}^{in}$ as follows,

$$\dot{\boldsymbol{\varepsilon}}^{in} = \dot{\lambda}\,\boldsymbol{g} = \exp(h)\left\langle \frac{\sigma^*}{a} - 1 \right\rangle^n \boldsymbol{g} \tag{3.11}$$

where $\dot{\lambda} = \left\|\dot{\boldsymbol{\varepsilon}}^{in}\right\|$ is the effective inelastic strain rate, $\boldsymbol{g}$ is the inelastic flow direction, $\langle\cdot\rangle$ denotes Macaulay brackets, h is a material constant, and n is another material constant. The Macaulay brackets give the model a purely elastic domain, where $\dot{\lambda} = 0$, for $\sigma^* < a$, and an elastic-viscoplastic domain, where $\dot{\lambda} \geq 0$, for $\sigma^* \geq a$.

The inelastic flow direction $\boldsymbol{g}$ is a symmetric second order unit tensor that is a combination of the radial and associated flow directions. These radial and associated flow directions are respectively defined as

$$\boldsymbol{g}_{radial} = \frac{\boldsymbol{\sigma}}{\|\boldsymbol{\sigma}\|} = \frac{\boldsymbol{\sigma}}{\sqrt{\boldsymbol{\sigma} : \boldsymbol{\sigma}}} \tag{3.12}$$

$$\boldsymbol{g}_{associated} = \frac{\frac{\partial \varphi}{\partial \boldsymbol{\sigma}}}{\left\|\frac{\partial \varphi}{\partial \boldsymbol{\sigma}}\right\|} = \frac{\frac{3}{a^2}\boldsymbol{\sigma}^{dev} + \frac{2}{3b^2}p\,\boldsymbol{I}}{\left\|\frac{3}{a^2}\boldsymbol{\sigma}^{dev} + \frac{2}{3b^2}p\,\boldsymbol{I}\right\|}. \tag{3.13}$$

These two flow directions are linearly combined as

$$\boldsymbol{g} = \frac{(1-\beta)\,\boldsymbol{g}_{associated} + \beta\,\boldsymbol{g}_{radial}}{\left\|(1-\beta)\,\boldsymbol{g}_{associated} + \beta\,\boldsymbol{g}_{radial}\right\|}, \tag{3.14}$$

where $\beta = \beta(\xi)$ is the radial flow fraction. The radial flow fraction is another user defined function, but it is constrained to be $0 \leq \beta \leq 1$. Pure radial flow means the inelastic strain rate is aligned with the applied stress. Pure associated flow means the inelastic flow direction is normal to the yield surface.

If a, b, and/or β evolve with ξ, then $\boldsymbol{g}$'s direction evolves with ξ. Typically, β begins at a high value and decreases as ξ increases in order to cause the associated flow contribution to $\boldsymbol{g}$ to increase as the material is compacted. In addition, b typically evolves to larger values than a, such that the associated flow direction evolves to become more deviatoric (more volume preserving) as the material is compacted. Under uniaxial stress compaction, a transition from largely radial flow toward volume preserving flow causes the lateral strain to grow more quickly as compaction progresses.

3.1.2. Pore Pressure Effects

WIPP waste is a porous material that will likely be subjected to a pore pressure p_p above atmospheric pressure inside a disposal room, so one might think that the FD model would need to be formulated to take into account p_p. Although the FD model does not explicitly include p_p in the formulation, one can conceptually include it, provided certain conditions are met. The Terzaghi effective stress is a common and appropriate way to incorporate pore pressure effects since the solids within the waste are practically incompressible compared to the overall compressibility of the waste. The Terzaghi effective stress is defined as $\bar{\boldsymbol{\sigma}} = \boldsymbol{\sigma} - p_p \boldsymbol{I}$, where $\boldsymbol{\sigma}$ is the total Cauchy stress. The pore pressure will be spatially uniform if the applied strain rate is slow enough relative to fluid flow rates through the pore network. This condition is likely met because the strain rates are reasonably slow in the experiments, the strain rates are far slower in a WIPP disposal room, waste containers are vented (as mentioned in Section 2.2), and compacted waste is assumed to be quite permeable to fluid flow. If the pore pressure is spatially uniform, then the fluid pressure at the boundary of the waste block is equal to the pore pressure. If one takes care to not apply fluid pressure to the boundary of the waste block, then $\bar{\boldsymbol{\sigma}} = \boldsymbol{\sigma}$ and pore pressure effects are effectively included in Section 3.1.1.

3.1.3. Strain Rate Dependence Under Hydrostatic and Uniaxial Stress

To understand the model's strain rate dependence under hydrostatic stress, it is instructive to combine Eqs. (3.10) and (3.11) to obtain

$$\left(\frac{\bar{\sigma}}{a}\right)^2 + \left(\frac{p}{b}\right)^2 = \left[\left(\frac{\dot{\lambda}}{\exp(h)}\right)^{1/n} + 1\right]^2, \tag{3.15}$$

set $\bar{\sigma} = 0$, and rearrange Eq. (3.15) as

$$|p| = b\left[\left(\frac{\dot{\lambda}}{\exp(h)}\right)^{\frac{1}{n}} + 1\right]. \tag{3.16}$$

The hydrostatic strain rate dependence is controlled by the $\left[\left(\dot{\lambda}/\exp(h)\right)^{1/n}+1\right]$ factor in Eq. (3.16), and the volumetric strain rate is approximately equal to $\dot{\lambda}$ because the elastic volumetric strain rate is typically small compared to the inelastic strain rate and $\boldsymbol{g}$ is always aligned with the hydrostat under hydrostatic stress. This makes the strain rate dependence straightforward to calibrate against hydrostatic stress tests.

To understand the model's strain rate dependence under uniaxial stress, set $p = \bar{\sigma}/3$, and rearrange Eq. (3.15) as

$$\bar{\sigma} = c\left[\left(\frac{\dot{\lambda}}{\exp(h)}\right)^{\frac{1}{n}}+1\right], \tag{3.17}$$

where

$$c = \left[\frac{1}{a^2}+\frac{1}{(3b)^2}\right]^{-1/2}. \tag{3.18}$$

The strain rate dependence is again controlled by the $\left[\left(\dot{\lambda}/\exp(h)\right)^{1/n}+1\right]$ factor in Eq. (3.17), but $\dot{\lambda}$ generally varies with ξ under uniaxial stress, even if the axial strain rate magnitude $|\dot{\varepsilon}_{zz}|$ is held fixed in a given experiment. As shown in Fig. 3-1, when the model calibration presented in Section 3.2 is used to simulate experiment WC-UC-NDQ-02, $\dot{\lambda} \approx |\dot{\varepsilon}_{zz}|$ only at $t = 0$. (The fluctuations in $\dot{\lambda}$ are due to using the axial strain measurements from the experiment to drive the axial strain in the simulation.) As ξ increases, the flow direction $\boldsymbol{g}$ increasingly deviates from $\boldsymbol{g}^{radial}$, such that $\dot{\lambda} > |\dot{\varepsilon}_{zz}|$ must hold to have $\dot{\lambda}\, g_{zz} \approx \dot{\varepsilon}_{zz}$. The ratio $\dot{\lambda}/|\dot{\varepsilon}_{zz}|$ depends on b/a and β for a given ξ, but it is independent of $|\dot{\varepsilon}_{zz}|$.

3.2. Waste Material Model Calibration

This section describes the procedure used to calibrate the FD constitutive model and defines the calibrated parameters/functions.

3.2.1. Calibration Procedure

The waste material model was calibrated by simulating the various experiments, comparing the simulated responses against the measured responses, manually modifying various model parameters/functions, and repeating the process until a satisfactory match was obtained.

Attempts to calibrate the model against all the measurements from the uniaxial, triaxial, and hydrostatic tests were not fruitful. One could satisfactorily calibrate the model to capture the stress vs. strain measurements from two out of the three test types, but not all three test types. A potential reason is the mechanical behavior of actual waste likely depends on whether it was uniaxially, triaxially, or hydrostatically compacted to reach a given ξ, yet the FD constitutive model only uses ξ to define the degree of hardening and ξ cannot distinguish between different modes of compression. In other words, deformation dependent anisotropy likely develops, yet the FD model only includes simple isotropic hardening. Anisotropic models were briefly considered

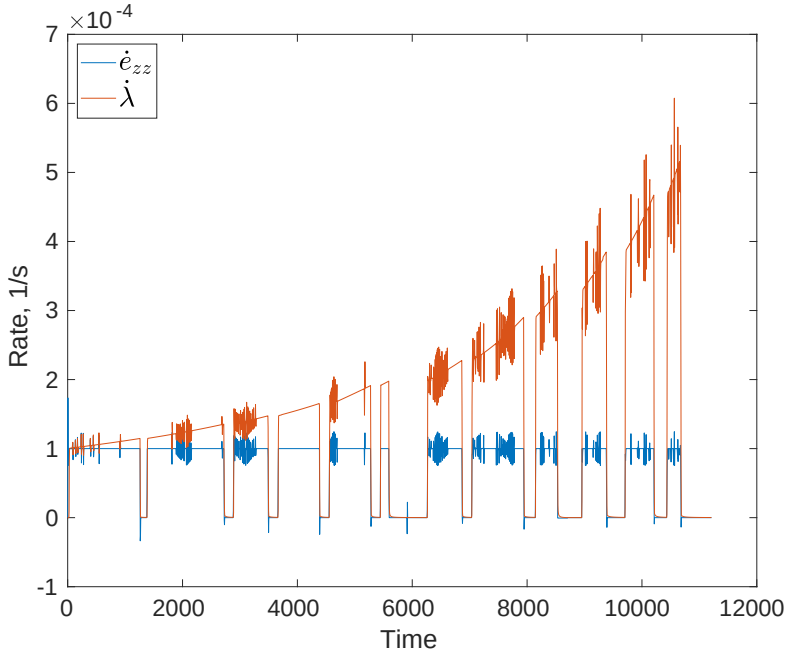

Figure 3-1. Comparison of axial strain rate $\dot{e}_{zz}$ to the inelastic strain rate magnitude $\dot{\lambda}$ during a uniaxial compression simulation of experiment WC-UC-NDQ-02.

and discarded because their added complexity was thought to outweigh their higher fidelity. As will be discussed in Section 3.4, capturing the uniaxial stress vs. strain curves was thought to be far less important than capturing the triaxial and hydrostatic behaviors. Consequently, the FD model was calibrated against the measured triaxial and hydrostatic behaviors, and, to a lesser extent, the uniaxial lateral strain vs. axial strain responses. The calibration did not attempt to capture the uniaxial stress vs. strain responses.

All calibration simulations were performed by prescribing the appropriate pressure and displacement boundary conditions on a single finite element using Sierra/SolidMechanics (2022). Spatially uniform pressures and deformations were applied, such that the single element simulations were essentially material point simulations. In each hydrostatic simulation, the deformation was prescribed to match the engineering volumetric strain history measured in the 1/4-scale experiment WC-HC-NDQ-02, except the strain history was artificially extended at a rate of $\dot{e}_v = 10^{-4}$ 1/s in order to reach $p \geq 15$ MPa. (This means the simulations of the full-scale hydrostatic compression tests did not include the switch from volume strain control to pressure control employed in the experiments (see Table 2-11).) Similarly, in each uniaxial simulation, the axial deformation was prescribed to match the engineering strain history measured in the 1/4-scale experiment WC-UC-NDQ-02, which utilized $\dot{e}_a = 10^{-4}$ 1/s, except the strain history was artificially extended at a rate of $\dot{e}_a = 10^{-4}$ 1/s in order to reach $\varepsilon_a = 1.5$. (The uniaxial tests at other strain rates did not need to be individually simulated, as discussed below.) The triaxial simulations also mimiced the experiments by gradually increasing the hydrostatic stress to reach a target value, unloading to zero stress, reloading to the same target hydrostatic stress, and then prescribing an axial engineering strain history. By using the corresponding measured strain

history as an input to each simulation, each simulation included the unload/reload loops in the corresponding experiment.

Although engineering strain histories were used as inputs to the simulations, care was taken to compare experiments against simulations using Cauchy stress measures and logarithmic strain measures. Comparisons of simulated responses against experimental measurements were done via simple visual comparisons of stress vs. strain curves and lateral strain vs. axial strain curves.

The steps to calibrate the model were as follows:

1. The experimental measurements of Poisson's ratio did not conclusively indicate a clear dependence on density, so Poisson's ratio was set to $\nu = 0.3$. This value was roughly in the middle of those measured in the uniaxial vs. triaxial experiments (see Figs. 2-15 and 2-21).

2. Manual iterations through the following three sub-steps were performed until a satisfactory fit to the 1/4-scale experiments was found. This process created deviatoric and hydrostatic strength functions specific to the 1/4-scale experiments, which are respectively denoted as $a(\xi) = a_{1/4}(\xi)$ and $b(\xi) = b_{1/4}(\xi)$. Other parameters and functions were not specific to the 1/4-scale experiments, so they are not labeled with "1/4" subscripts.

    a) The 1/4-scale hydrostatic strength $b_{1/4}(\xi)$ was manually adjusted to match the 1/4-scale hydrostatic p vs. ε^{vol} curves, ignoring the elastic unloading/reloading portions of the experiments. This step was performed first because the FD constitutive model's response to pure hydrostatic loading is independent of $a(\xi) = a_{1/4}(\xi)$ and $\beta(\xi)$.

    b) The functions $a_{1/4}(\xi)$, $\beta(\xi)$, and $E(\xi)$ were manually adjusted to match the 1/4-scale triaxial compaction stress difference vs. axial strain curves, the 1/4-scale triaxial compaction lateral strain vs. axial strain curves, and the 1/4-scale uniaxial lateral strain vs. axial strain curves, all at the axial engineering strain rate of 10^{-4} 1/s.

    c) The parameters h and n were manually adjusted to match the strain rate sensitivity of the 1/4-scale uniaxial stress vs. strain curves.

        i. The predicted uniaxial stress had to be artificially scaled to roughly match the 1/4-scale uniaxial strength measurements because the calibration did not capture the experimentally measured uniaxial stress vs. strain behavior, as mentioned above. This scaled prediction $\bar{\sigma}^{sc}$ was simply

$$\bar{\sigma}^{sc} = f\,\bar{\sigma}, \tag{3.19}$$

        where $\bar{\sigma}$ was computed using Eq. (3.17) and f was selected to make $\bar{\sigma}^{sc}$ match the average 1/4-scale uniaxial strength at $\varepsilon_a = 1.14$ and $\dot{e}_a = 10^{-4}$ 1/s. The axial strain $\varepsilon_a = 1.14$ corresponded to $\xi = 0.39$ in WC-UC-NDQ-02. (Recall that $\xi = 0.39$ corresponds to the practical lock-up point in Fig. 2-13.) Equation (3.17) requires a value of $\dot{\lambda}$, but $\dot{\lambda}$ varies with ξ under uniaxial stress, as discussed in Section 3.1.3, so a uniaxial stress simulation was conducted at $\dot{e}_a = 10^{-4}$ 1/s to establish $\dot{\lambda} = \dot{\lambda}_{ref}$ at $\xi = 0.39$.

ii. The parameters h and n in Eq. (3.17) were adjusted to make $\bar{\sigma}^{sc}$ agree with the uniaxial stress measurements for $\dot{e}_a < 10^{-4}$ 1/s. To ensure that the newly adjusted values h_{new} and n_{new} would not alter $\bar{\sigma}^{sc}$ at $\dot{e}_a = 10^{-4}$ 1/s and $\xi = 0.39$, the following constraint

$$\left(\frac{\dot{\lambda}_{ref}}{\exp(h_{new})}\right)^{1/n_{new}} = \left(\frac{\dot{\lambda}_{ref}}{\exp(h)}\right)^{1/n} \tag{3.20}$$

was enforced. Of course, once h_{new} and n_{new} were selected, the old values of h and n were respectively replaced with h_{new} and n_{new}.

3. The full-scale strength functions were respectively computed from the 1/4-scale strength functions as $a(\xi) = a_{1/4}(w\xi)$ and $b(\xi) = b_{1/4}(w\xi)$, where $w = 1.12$ was selected to scale the response from the stiffer 1/4-scale hydrostatic p vs. ε_v curves to the more relevant full-scale hydrostatic compaction p vs. ε_v curves. This approach assumes the shear behavior scales in the same manner as the hydrostatic behavior, which is reasonable given the similarities between the for full-scale and 1/4-scale hydrostatic and uniaxial tests as can be seen in Figs. 2-12 and 2-27 in the early stages of the tests.

3.2.2. Parameters and Functions for Calibration 1

Table 3-1. Calibration 1 parameters and functions for FD model.

Parameter / Function		Units	Value
Initial Density	ρ_0	kg/m^3	505.5
Initial Solid Volume Fraction	ξ_0	-	0.175
Young's Modulus Reference	E_r	GPa	4.0
Young's Modulus Fraction	$E_\xi(\xi)$	-	See Table 3-2a and Fig. 3-2
Poisson's Ratio Reference	v_r	-	0.3
Poisson's Ratio Fraction	v_ξ	-	1
Shear Strength	$a(\xi)$	MPa	See Table 3-2c and Fig. 3-3
Hydrostatic Strength	$b(\xi)$	MPa	See Table 3-2d and Fig. 3-3
Radial Flow Fraction	$\beta(\xi)$	-	See Table 3-2b and Fig. 3-3
Flow Rate	h	-	-55.0
Power Exponent	n	-	23.0

The new waste material model parameters/functions for "Calibration 1" are given in Tables 3-1 and 3-2. An example input file for use with Sierra/SolidMechanics (2022) is also included in Chapter B. The name Calibration 1 was adopted in case future studies elect to create new waste material model calibrations of the FD constitutive model. All other preliminary calibrations referred to in this report were eventually abandoned so they were not given formal names.

Table 3-2. Values used to construct piecewise linear functions found in Table 3-1.

(a) Young's Modulus Fraction

ξ (−)	E_ξ (−)
0.000	0.010
0.250	0.015
0.400	0.025
0.500	0.075
0.650	0.128
1.000	0.500
2.000	1.000
100.0	1.000

(b) Radial Flow Fraction

ξ (−)	β (−)
0.000	0.700
0.200	0.700
0.250	0.650
0.300	0.550
0.350	0.400
0.400	0.220
0.450	0.150
0.500	0.075
0.640	0.000
1.000	0.000
10.00	0.000

(c) Shear Strength

ξ (−)	a (MPa)
0.000	0.02
0.112	0.02
0.280	0.02
0.336	0.02
0.392	0.04
0.448	0.07
0.470	0.12
0.493	0.19
0.504	0.22
0.560	0.36
0.582	0.46
0.616	0.72
0.672	1.32
0.694	1.74
0.728	2.80
0.784	4.42
0.896	10.52
1.008	14.62
1.120	30.00
11.20	500.0

(d) Hydrostatic Strength

ξ (−)	b (MPa)
0.000	0.012
0.280	0.012
0.336	0.036
0.448	0.132
0.504	0.240
0.560	0.480
0.672	1.440
0.784	12.0
0.896	45.6
1.008	84.0
1.120	168.0
11.20.	960.0

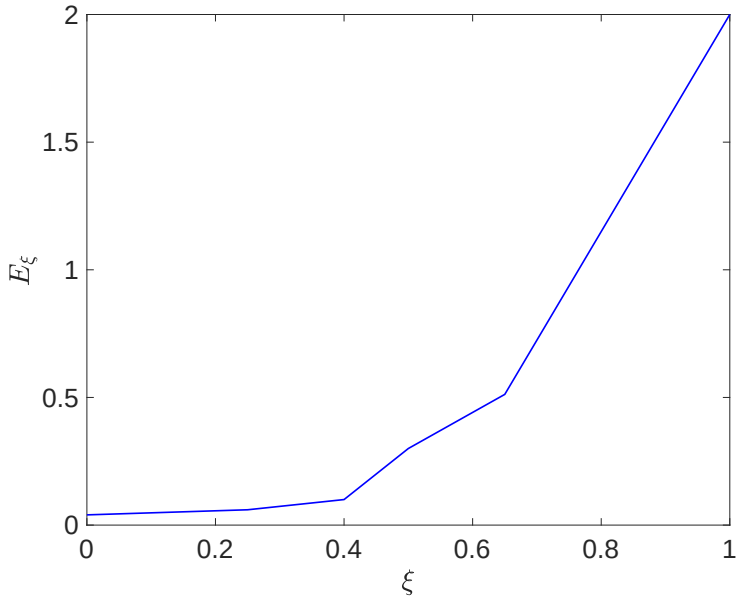

Figure 3-2. Young's modulus fraction E_ξ versus solid volume fraction ξ.

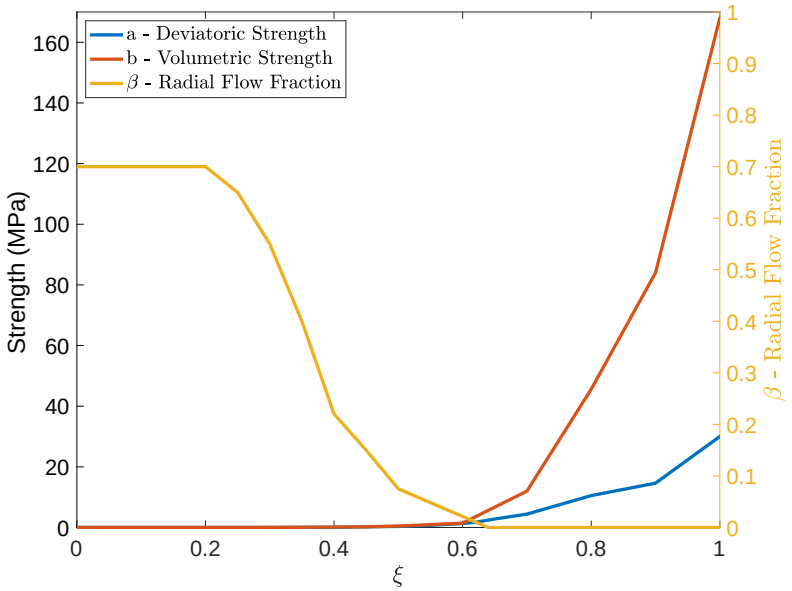

Figure 3-3. Deviatoric and volumetric strengths (left axis) versus solid volume fraction, ξ, and radial flow fraction (right axis) versus ξ.

Calibration 1's initial density ρ_0 and initial solid volume fraction $\xi_0 = 1 - \phi_0$ were selected to match those of the experiment samples, as documented in Section 2.1, while the other parameters/functions were calibrated using the procedure described in Section 3.2.1. As shown in Figs. 3-2 and 3-3, the continuous functions $E_\xi = E_\xi(\xi)$, $a = a(\xi)$, $b = b(\xi)$, and $\beta = \beta(\xi)$ are each constructed as a piecewise linear interpolation of the corresponding values in Table 3-2. As ξ increases, the functions $E_\xi(\xi)$, $a(\xi)$, and $b(\xi)$ all increase, as one might expect. The function $\beta(\xi)$, on the other hand, decreases from 0.7 to 0 with increasing ξ. The horizontal axis in each plot is $0 \le \xi \le 1$, which are the valid values of ξ, but each table includes values beyond $\xi = 1$ to ensure the waste material continues to stiffen if the FD model implementation erroneously allows $\xi > 1$, which has not been observed.

The FD model also includes the ability to limit principal tensile stresses by setting an initial tensile strength that can subsequently degrade with damage. This ability, however, was effectively de-activated by setting the initial tensile strength to 100 MPa.

3.3. Comparison Against Experiments

This section compares the legacy waste material model, as defined in Section 1.3, and new waste material model, as defined by Sections 3.1.1 and 3.2.2, against the experiments used to calibrate the new model parameters/functions. Single finite element simulations within Sierra/SolidMechanics (2022) were used to probe both the new and legacy waste material model behaviors. Note that all experiments and corresponding simulations included multiple elastic

unload/reload phases, but the plots in this section do not include the elastic unload/reload phases for ease of viewing.

Fig. 3-4 compares the legacy and new waste material model uniaxial compression behaviors against the uniaxial compression test results at $\dot{e}_a = 10^{-4}$ 1/s. All of the results for the 1/4-scale and full-scale experiments are plotted. The legacy model sharply over-predicts the measured uniaxial stress vs. strain responses and erroneously predicts non-monotonic lateral shrinkage rather than lateral expansion. The new model fares better, but its predictions are far from perfect. It correctly captures the highly compliant uniaxial stress vs. strain responses for $0 < \varepsilon_a < 0.5$ in Fig. 3-4a, yet severely under-predicts the responses for $0.5 < \varepsilon_a$, as expected from the discussion in Section 3.2.1. Section 3.4 presents a justification for ignoring these poor predictions at high uniaxial strains. On the other hand, the new model does a far better job of capturing the lateral strain vs. axial strain measurements in Fig. 3-4b than the legacy model. The new model predicts monotonic lateral expansion, rather than non-monotonic lateral shrinkage. Nevertheless, the new model lateral strain predictions align better with the 1/4-scale measurements than the full-scale measurements. Alternate new model calibrations more closely captured the full-scale lateral strain vs. axial strain measurements, but these alternate model calibrations were abandoned because they poorly captured the triaxial test results. Regardless, it is encouraging that the new model qualitatively captures the observed lateral expansion, which is a factor in predicting the transition away from uniaxial stress loading, toward hydrostatic loading, during a disposal room simulation.

The dashed vertical line and two labeled coordinate pairs in Fig. 3-4a help explain how the scaling factor f in Eq. (3.19) was computed. The dashed vertical line in Fig. 3-4a at $\varepsilon_a = 1.14$ shows the logarithmic strain corresponding to $\xi = 0.39$ in WC-UC-NDQ-02. (Recall that $\xi = 0.39$ corresponds to the practical lock-up point in Fig. 2-13.) The coordinate pairs in Fig. 3-4a are (logarithmic axial strain, axial Cauchy stress). The stress in the upper coordinate pair is the averaged axial Cauchy stress of the four 1/4-scale experiments at $\varepsilon_a = 1.14$. The stress in the lower coordinate pair is the axial Cauchy stress simulated by the new model at $\varepsilon_a = 1.14$. (The new model also happens to predict $\xi = 0.39$ at $\varepsilon_a = 1.14$.) The scaling factor is the ratio of these two stresses: $f = 3.742$ MPa$/0.3385$ MPa $= 11.05$.

Fig. 3-5 depicts the strain rate dependence measured in the uniaxial stress experiments, as well as the new model's strain rate dependence, but the plot requires some introduction. The von Mises stress was extracted from each uniaxial stress experiment at $\xi = 0.39$ and plotted versus the inelastic strain rate $\dot{\lambda}$. The experiments did not measure $\dot{\lambda}$, so uniaxial stress simulations with the new waste material model were used to compute $\dot{\lambda}$ at $\xi = 0.39$ for each $\dot{e}_a$ used in the experiments. The plot also contains four dashed vertical lines, which indicate the four different engineering strain rates $\dot{e}_a$ used in the tests. Comparing the measurements to the immediate right of each dashed line confirms that the ratio of $\dot{\lambda}/\dot{e}_a$ does not depend on $\dot{e}_a$, as pointed out in Section 3.1.3. The plot also includes a dashed vertical lines at $\dot{\lambda} = 2 \times 10^{-11}$ 1/s and $\dot{\lambda} = 1 \times 10^{-14}$ 1/s, which indicate the range of waste block strain rates expected for compaction within a WIPP disposal room (see Fig. 3-9d). Finally, the blue curve in the plot depicts $\bar{\sigma}^{sc}$ versus $\dot{\lambda}$, which was computed using Eqs. (3.17) to (3.19) with $f = 11.05$, $a(\xi) = a_{1/4}(\xi)$, $b(\xi) = b_{1/4}(\xi)$, and $\xi = 0.39$ to make the new model behavior artificially agree with the 1/4-scale uniaxial measurements, at least at $\xi = 0.39$.

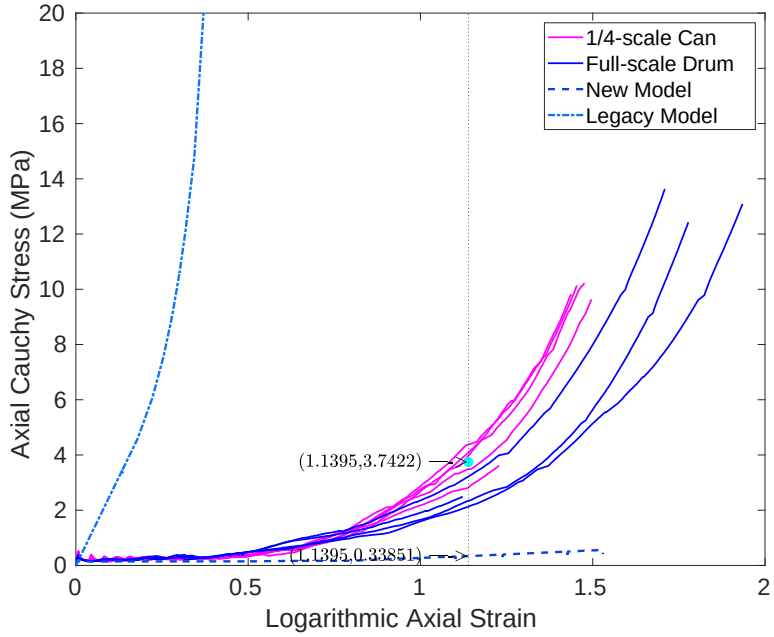

(a) Axial stress vs. axial strain

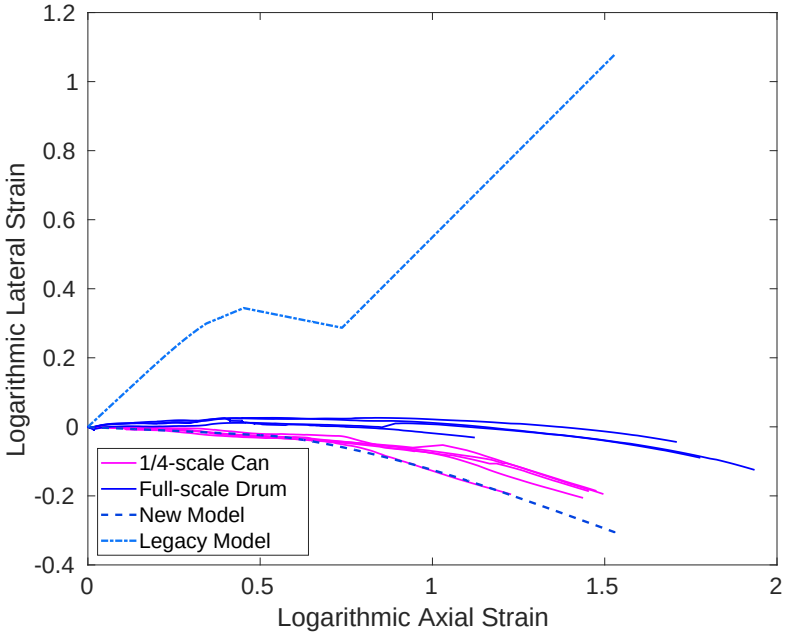

(b) Lateral strain vs. axial strain

Figure 3-4. Comparisons of the new and legacy models' response to uniaxial compression against the $^1/_4$- and full-scale uniaxial compression test results at $\dot{e}_a = 10^{-4}$ 1/s. See main text for a description of the vertical dashed line and coordinate pairs in Fig. 3-4a.

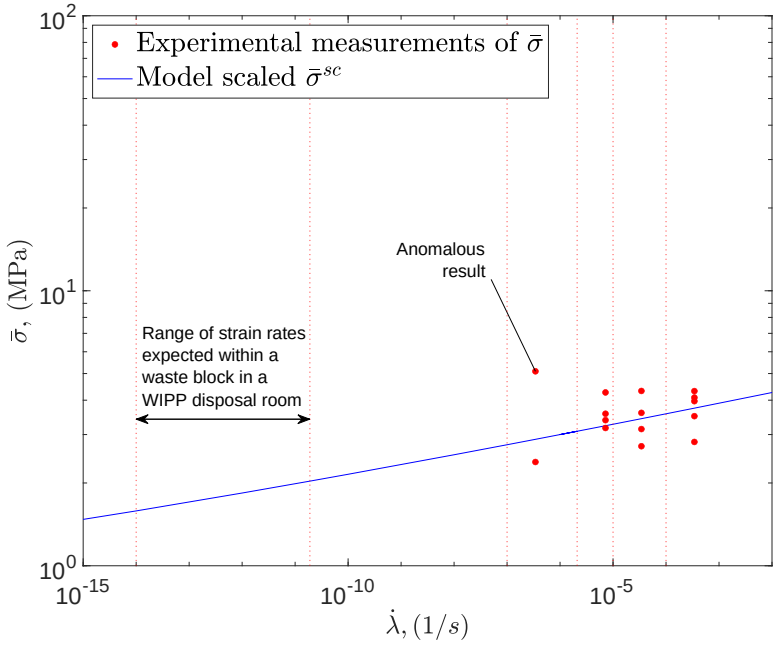

Figure 3-5. A comparison of the experimentally measured strain rate dependence against the model's (scaled) behavior for uniaxial compression. All stresses and strain rates correspond to $\xi = 0.39$.

The measurement scatter in Fig. 3-5 makes it difficult to precisely pin down the strain rate dependence. Note that the highest $\bar{\sigma}$ measurement at the slowest applied axial strain rate is most likely an anomalous result (see Section 2.5.3). When this point is neglected, the test results seem to indicate a small amount of strain rate dependence. Further tests would more precisely quantify this dependence, but the new model's $\bar{\sigma}^{sc}$ vs. $\dot{\lambda}$ is a reasonable fit to the existing measurements. An alternate new model calibration with slightly less strain rate dependence was considered and discarded after it poorly captured the triaxial test results. The impact of extrapolating the new model behavior down to expected strain rates within a WIPP disposal room is considered in Section 3.5.

Figure 3-6 compares the triaxial compression test results against the corresponding legacy and new model behaviors. The responses for four different radial confining pressures (p_c =1 MPa, 2 MPa, 5 MPa, and 15 MPa) are shown. The lateral strain is plotted as $\varepsilon_l - \varepsilon_l^h$, which is the lateral strain relative to the lateral strain at the end of the hydrostatic compression phase. Similarly, all quantities are plotted against $\varepsilon_a - \varepsilon_a^h$, which is the axial strain relative to the axial strain at the end of the hydrostatic compression phase. (Note that this method of plotting is compact, but hides the fact that the triaxial phase starts at a different total axial and lateral strain for each confining pressure. See Fig. 2-19 for plots of the experimental measurements using total axial and lateral strain.) The new model responses agree far better with the experimental measurements than the legacy model responses. The legacy model greatly over-predicts the differential stress measurements for all confining pressures; incorrectly predicts lateral shrinkage for p_c = 1, 2, and 5 MPa; and incorrectly predicts a non-monotonic lateral strain history for p_c = 15 MPa. The new model, by contrast, produces differential stress and lateral strain vs. axial strain curves agree fairly

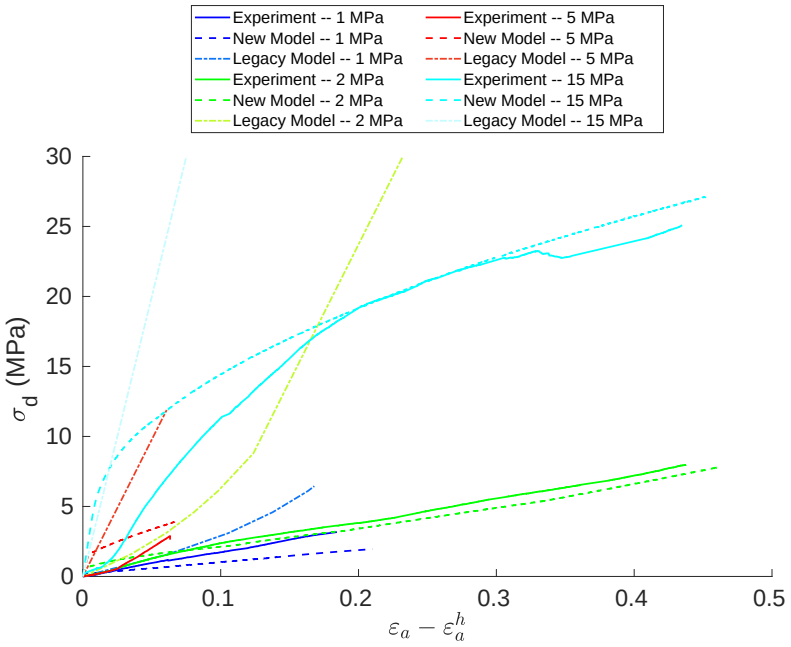

(a) Differential stress vs. axial strain

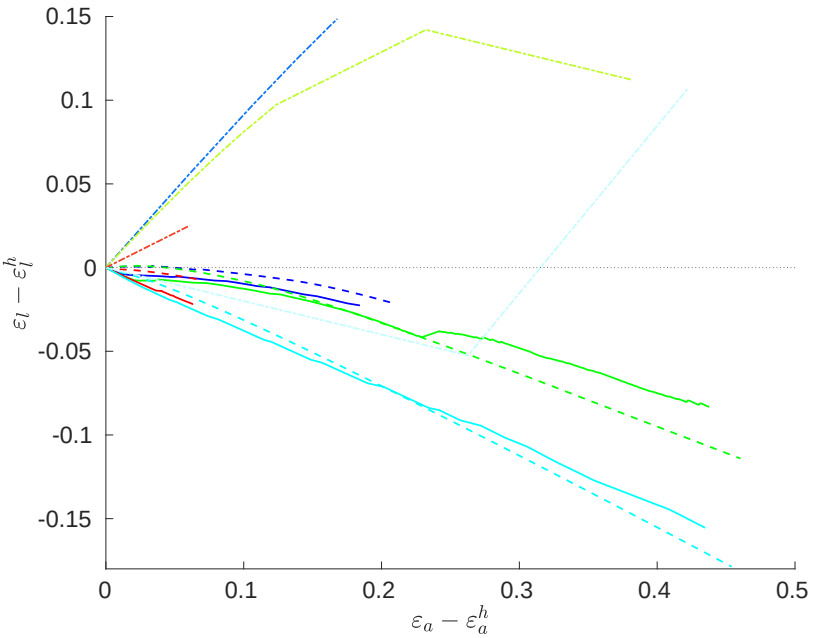

(b) Lateral strain vs. axial strain

Figure 3-6. Comparisons of triaxial compression measurements for four different confining pressures versus the corresponding legacy and new model behaviors. In all cases, $\dot{e}_a = 10^{-4}$ 1/s.

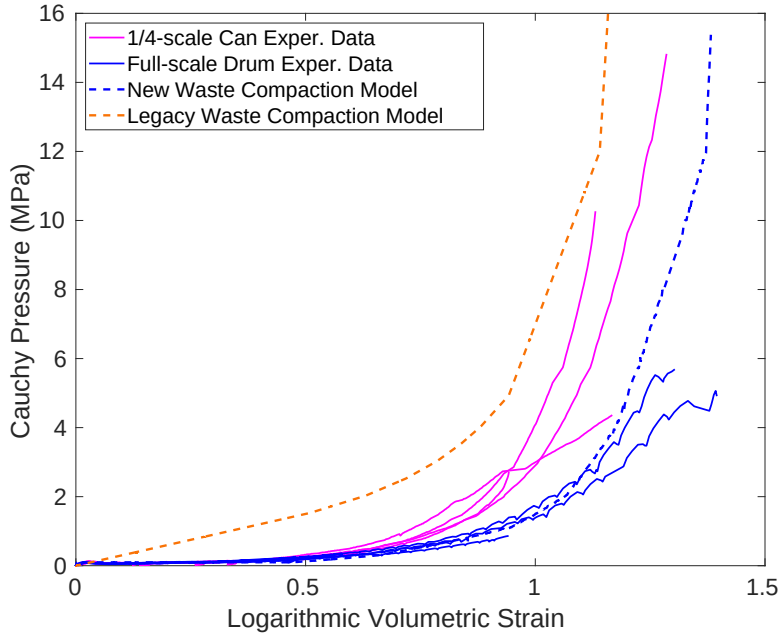

Figure 3-7. Comparison of experimental hydrostatic compression test results versus the corresponding legacy and new model behaviors. In all cases, $\dot{e}_v = 10^{-4}$ 1/s.

well with the test results, except for the $p_c = 5$ MPa case. The 5 MPa test could be an outlier, or perhaps the new model simply cannot capture a transition in behavior between 2 and 15 MPa confining pressure. Regardless, the overall quality of the agreement between the new model and the test results is encouraging, given the non-proportional stress paths (hydrostatic followed by triaxial) employed in these tests.

Figure 3-7 compares the experimentally measured hydrostatic behavior against the new and legacy waste model behaviors. Of the experiment types used to measure the waste strength in this section, the hydrostatic compaction tests are probably the most relevant since the final stress state in a disposal room is close to hydrostatic. The new waste model clearly agrees better with the full-scale container measurements than the legacy model, and is substantially more compliant than the legacy model when compared at the same volumetric strain. The new model offers practically negligible resistance until about $\varepsilon_v = 0.5$ and reaches $p^{litho} \approx 14.7$ MPa at $\varepsilon_v = 1.38$, while the legacy model predicts a non-negligible resistance as soon as $\varepsilon_v > 0.1$ and reaches p^{litho} at $\varepsilon_v = 1.16$. Likely causes for these differences between the legacy and new model hydrostatic compression predictions were discussed in Section 1.4. Figure 3-7 also demonstrates another reason why it was necessary to first calibrate $b(\xi)$ against the 1/4-scale measurements and then scale the $b(\xi)$ function (and $a(\xi)$ function) to match the full-scale measurements. The full-scale tests only reached $p = 5.7$ MPa, so the 1/4-scale model calibration provided a basis to reasonably extrapolate from 5.7 MPa up to p^{litho}.

3.4. Analysis of a Disposal Room Simulation

As discussed in Chapter 1, the principal motivation for developing a new waste material model was to more accurately simulate the waste compaction process within a WIPP disposal room. One such disposal room simulation was first performed and analyzed while calibrating the new waste material model to determine the most important waste compaction loading modes. The simulation and analysis were then repeated with the final waste model calibration, as documented in Section 3.2.2, to confirm the analysis conclusions had not changed. For simplicity, this section only documents the disposal room simulation with the final waste model calibration.

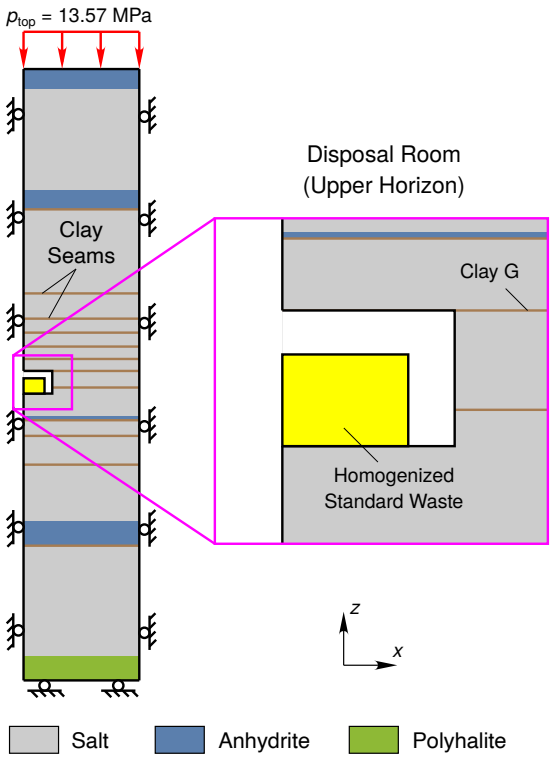

Figure 3-8. Stratigraphy, homogenized waste, and boundary conditions used in disposal room simulation.

Figure 3-8 depicts the stratigraphy, room, homogenized waste, and boundary conditions used in the two-dimensional, plane-strain, disposal room simulation. The details of the geomechanical model were similar to those of Simulation 11 in Reedlunn et al. (2022), except the width of the domain was 20.27 m, the half width of the room was 5.03 m, the height of the room was 3.96 m, and the top of the room was coincident with Clay G. Rather than model each individual drum, all the waste containers within the room were combined into a block of homogenized standard waste. This waste block had an initial height of 2.68 m, which is the height of three drums stacked on top of each other, and a half width of 3.68 m. The width of the waste was computed by conserving the initial volume of the containers, yet removing the void space between them (see Stone (1997a) for further details). The salt was allowed to viscoplastically deform into the room, compacting the waste, for 10,000 years of simulated time. The pressure due to any gas trapped within the room was ignored so that the compaction was entirely determined by the competition between the salt

and the waste. This initial boundary value problem was solved with the finite element method in Sierra/SolidMechanics (2022). To give an idea of the discretization, 25 selective deviatoric elements spanned the half width of the room and 18 selective deviatoric elements spanned the half width of the waste block.

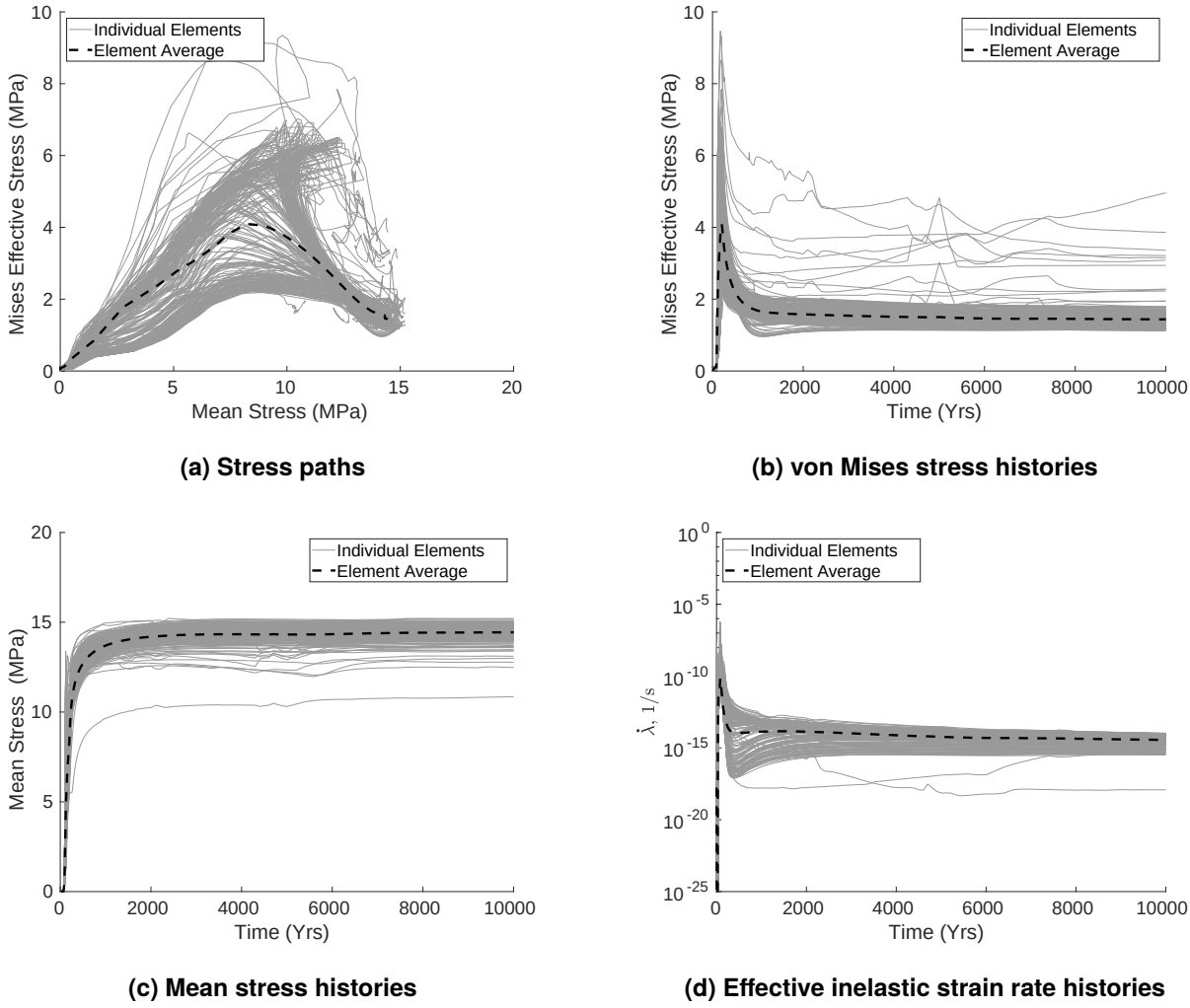

(a) Stress paths

(b) von Mises stress histories

(c) Mean stress histories

(d) Effective inelastic strain rate histories

Figure 3-9. Stress paths, stress histories, and equivalent strain rate histories of individual waste block elements and average of waste block element stress paths in the disposal room simulation.

The stress paths experienced by the waste during the disposal room porosity simulation are depicted in Fig. 3-9a. The light grey lines represent the stress paths of individual elements, averaged over the element's eight integration points, while the thick black dashed curve is the average of all the individual element stress paths. Fig. 3-9b, Fig. 3-9c, and Fig. 3-9d show the development of the von Mises effective stress, the element pressure (mean stress), and $\dot{\lambda}$ (computed using Eq. (3.11)), respectively, over time. In each plot, the light grey lines represent the progressions for each element and the thick black dashed curve represents the average of all of the elements. The average stress path seen in Fig. 3-9a is also seen in Fig. 3-10 where it is compared against the stress paths computed in the uniaxial, hydrostatic, and triaxial simulations at

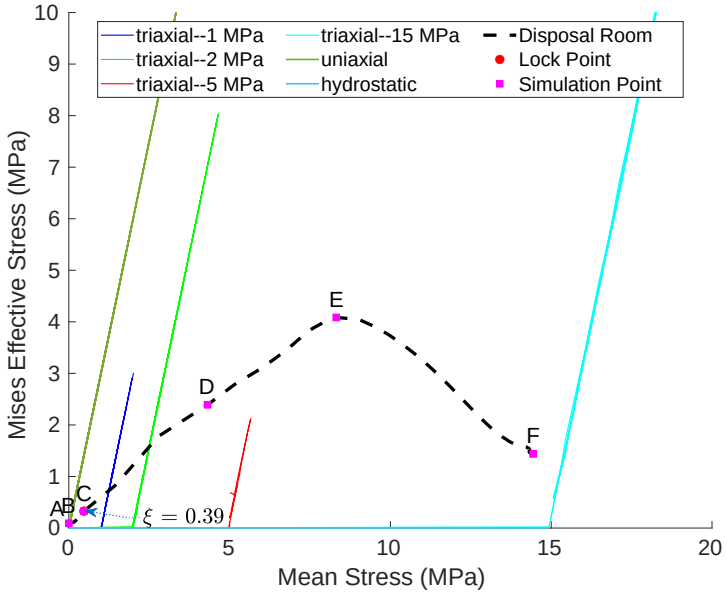

Figure 3-10. Average of waste block element stress paths from the disposal room simulation and experimental stress paths. Each labeled point along the average simulated stress path corresponds to an image in Fig. 3-11. Experimental stress paths include the uniaxial, hydrostatic, and triaxial tests at the four confining stresses.

the four confining stress. The red circle in Fig. 3-10 denotes the lock-up point ($\xi = 0.39$) where the waste begins to significantly resist the crushing pressure of the salt. The letter labels along the average stress path correspond to the deformed mesh images in Fig. 3-11.

Figure 3-10 demonstrates that the uniaxial stress response of the waste is not an important part of the waste compaction simulation. The waste experiences predominantly uniaxial stress between A and B as it is compressed between the floor and the ceiling (see Fig. 3-11a and Fig. 3-11b). This uniaxial stress state occurs *before* the majority of the waste reaches the lock-up point, so the waste does not yet supply significant resistance to compaction while in the uniaxial stress state.

Between B and C (see Figs. 3-10, 3-11b and 3-11c), the room walls begin to touch the sides of the homogenized waste, creating significant lateral stresses. The lateral stresses within the waste drive the waste's average stress path away from the uniaxial stress path and toward the triaxial stress paths. The lateral stresses are partly due to the room walls laterally compressing the waste, but also due to the waste attempting to laterally expand against the walls and the plane strain constraints.

At C (see Figs. 3-10 and 3-11c), the waste reaches the lock-up point and begins to supply significant back pressure to the salt after the lock-up point. The waste lock-up point corresponds to when the inelastic flow has completed most of its transition from predominantly radial to associative flow (see Fig. 3-3), a transition toward more volume preserving deformations. Triaxial compression of a volume preserving material leads to lateral expansion. These observations prompted the decision to focus the FD constitutive model calibration on the experimentally

measured triaxial and hydrostatic behaviors, qualitatively matching the uniaxial lateral strain vs. axial strain behavior, and forgo capturing the uniaxial stress vs. strain behavior for $\varepsilon_a > 0.5$.

After the lock-up point, the waste develops significant von Mises and mean stress. The average stress path between C and E crosses the 1 and 2 MPa confining pressure triaxial stress paths, and would cross the 5 MPa confining pressure triaxial stress path if it were extended. At E, the average von Mises stress reaches a maximum and begins decreasing towards a more hydrostatic stress state.

After 10,000 years, at F, the stress state is not fully hydrostatic, and it may not ever become fully hydrostatic, i.e. with zero von Mises stress. The salt constitutive model cannot sustain a non-zero von Mises stress over the long-term. The FD constitutive model, however, can maintain a non-zero von Mises stress forever: one can set $0 < \sigma^* \leq a$ with $\bar{\sigma} > 0$ and obtain $\dot{\lambda} = 0$ in Eq. (3.11). The homogenized waste surfaces in contact with the salt could eventually have $\sigma_{xx} = \sigma_{zz} = p^{litho}$, but the out-of-plane stress σ_{yy} does not necessarily become p^{litho} at $t = \infty$.

3.5. Plane Strain Compression Simulations

Section 3.3 compared the legacy and new waste material models against the experiments, but it is also important to make comparisons under plane strain compression. Plane strain conditions are often used to model the long and slender disposal rooms at the WIPP, so single finite element simulations of plane strain compression (see Fig. 1-5a) help one understand how switching from the legacy to the new waste model will affect future predictions of disposal room porosity. During the plane strain simulations in this section, equal engineering strain rates $\dot{e}_{xx} = \dot{e}_{zz}$ roughly mimic the compressive action of the drift walls and floor/ceiling, and cause each model to respond with $\sigma_{xx} = \sigma_{zz}$ stresses. The plane strain constraint ($\varepsilon_{yy} = 0$) mimics the lack of deformation along the length of the drift, and causes an out-of-plane stress σ_{yy}.

The plane strain behavior of the new and legacy models are shown in plots of stress vs. strain and in plots of stress vs. porosity. Both types of plots are needed to understand how a waste model influences a disposal room's spatially averaged Lagrangian porosity $\phi_L = V_g/V_{r0}$, where V_g is the void volume available for gas storage and V_{r0} is the original room volume. If the gas pressure within the room is negligible, the original room region quickly equilibrates to a combination of solid salt and porous waste. A waste model's stress vs. strain behavior and p^{litho} control the fraction of V_{r0} filled with salt. A waste model's stress vs. porosity behavior and p^{litho} control the porosity of the waste block within V_{r0}. Plotting stress vs. porosity also conveys that the new waste model starts at $\phi_i = 1 - \xi_i = 0.825$ while the legacy waste model starts at $\phi_i = 0.681$.

Fig. 3-12 compares the legacy and new models under plain strain loading at a strain rate of $\dot{e}_{xx} = \dot{e}_{zz} = 10^{-14}$ 1/s, which approximates the strain rate seen in the disposal room simulations detailed in Section 3.4. Each stress component is plotted against it conjugate strain component in Fig. 3-12a. First, notice that the legacy waste model predicts a non-physical tensile σ_{yy}, but the new waste model predicts reasonable compressive σ_{yy} behavior. The new waste model therefore resolves shortcoming 6 in Chapter 1. Second, observe that it is not entirely straightforward to say whether the new model will decrease or increase ϕ_L. For the same strain, as plotted in Fig. 3-12a,

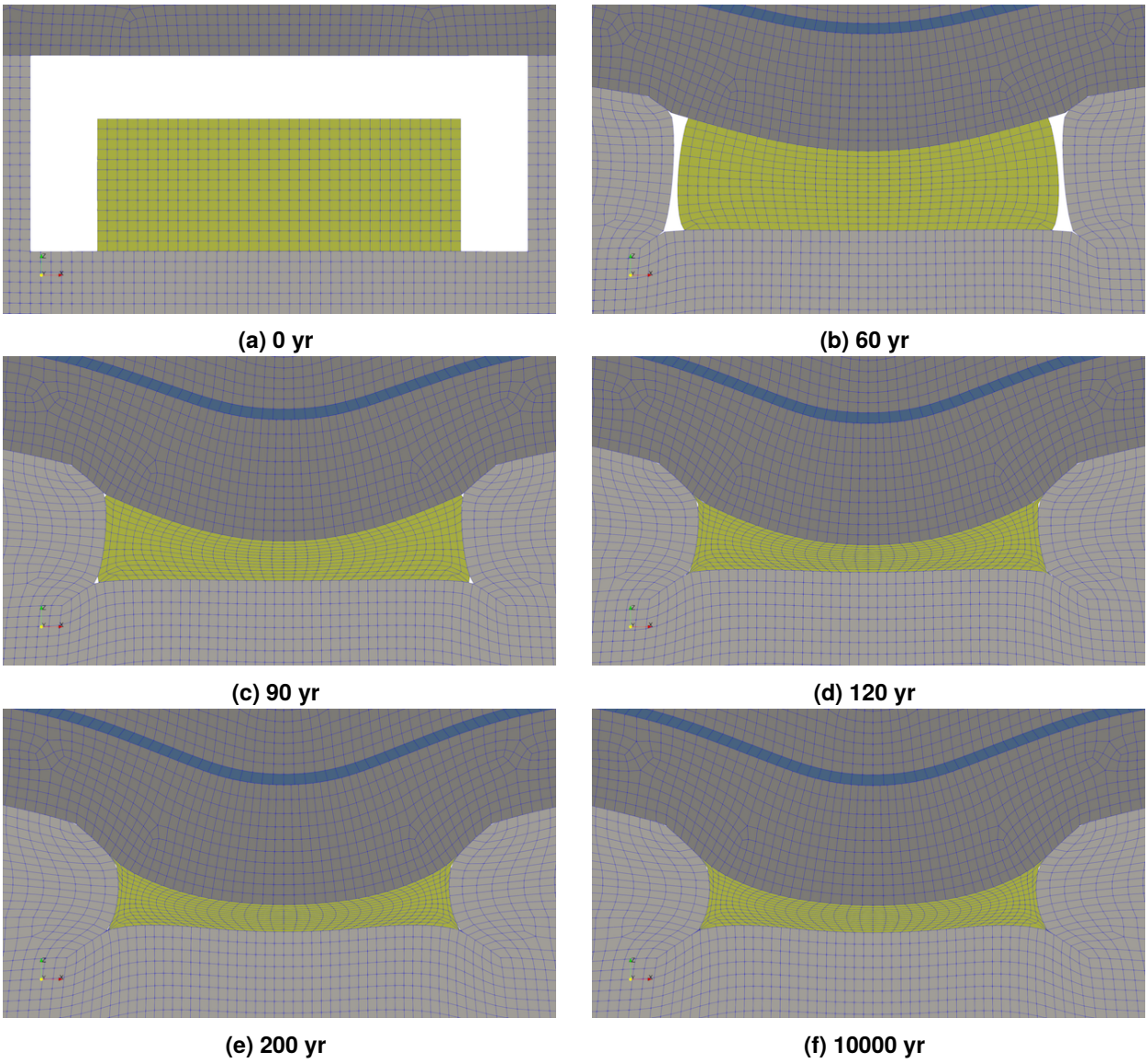

(a) 0 yr

(b) 60 yr

(c) 90 yr

(d) 120 yr

(e) 200 yr

(f) 10000 yr

Figure 3-11. Progression of compaction of waste in disposal room simulation. Moments in time correspond to points on stress path in Fig. 3-10.

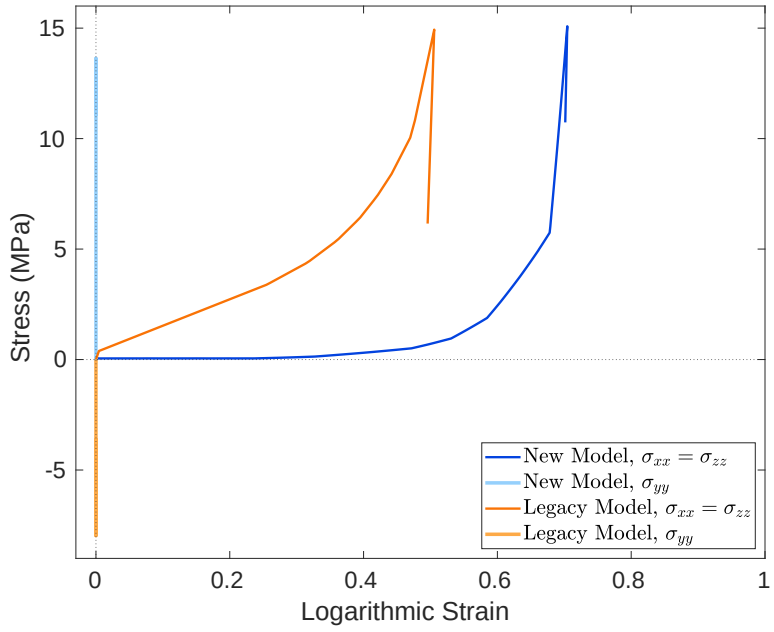

(a) Stress vs.logarithmic strain

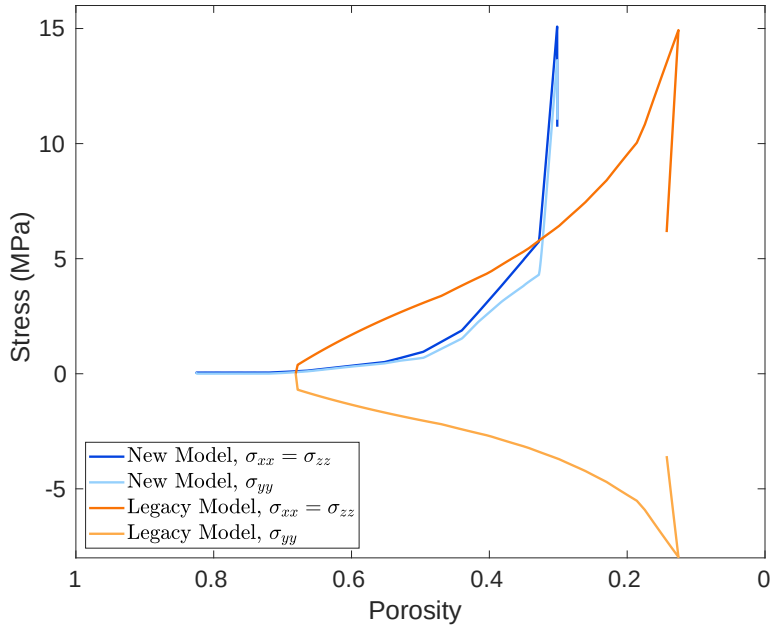

(b) Stress vs. porosity

Figure 3-12. A comparison of the legacy and new model responses to plane strain loading with $\dot{e}_{xx} = \dot{e}_{zz} = 10^{-14}$ 1/s and $e_{yy} = 0$.

the new waste model is more compliant. The new model offers practically negligible resistance until about $\varepsilon_{xx} = \varepsilon_{zz} = 0.3$ and reaches p^{litho} at $\varepsilon_{xx} = \varepsilon_{zz} = 0.7$, while the legacy model predicts a non-negligible resistance as soon as $\varepsilon_{xx} = \varepsilon_{zz} > 0$ and reaches p^{litho} at $\varepsilon_{xx} = \varepsilon_{zz} = 0.51$. For the same porosity, however, the new waste model exhibits significantly larger strength once $\phi < 0.32$, as shown in Fig. 3-12b. The new model reaches p^{litho} at $\phi = 0.30$, whereas the legacy model requires $\phi = 0.13$ to reach p^{litho}. Disposal room simulations are needed to precisely quantify which effect dominates.

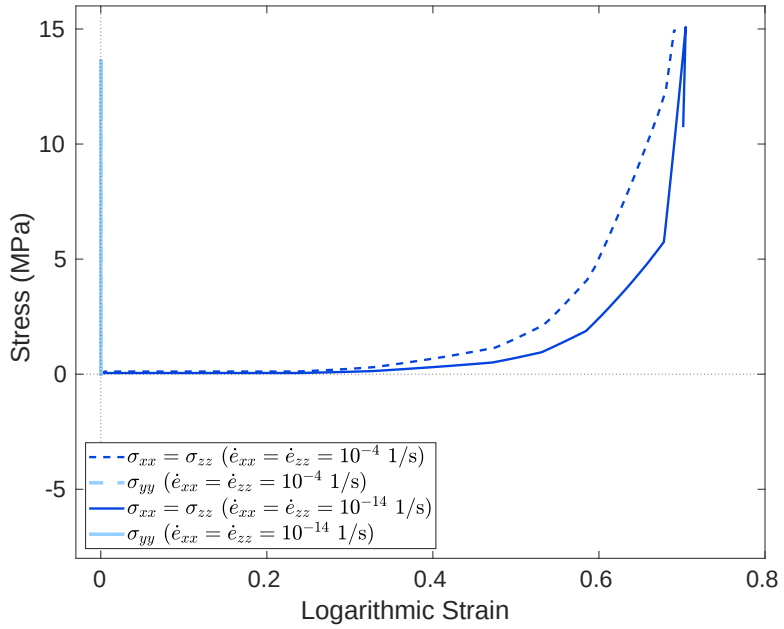

Figure 3-13. A comparison of new model's in-plane and out-of-plane responses under plane strain loading at two different strain rates.

Another difference between the legacy and new models is the new model includes rate dependence. Fig. 3-13 depicts the new model responses at two strain rate extremes. The fast strain rate of $\dot{e}_{xx} = \dot{e}_{zz} = 10^{-4}$ 1/s is representative of the laboratory tests, while $\dot{e}_{xx} = \dot{e}_{zz} = 10^{-14}$ 1/s loosely corresponds to the average $\dot{\lambda}$ predicted at the end of the disposal room simulation in Section 3.4. As one might expect from Fig. 3-5, the new model predicts the waste becomes significantly more compliant upon reducing the strain rate from 10^{-4} to 10^{-14} 1/s. Nevertheless, the new model's response is quite stiff when $\sigma_{xx} = \sigma_{zz} = p^{litho}$, so reducing the strain rate from 10^{-4} to 10^{-14} 1/s only increases $\varepsilon_{xx} = \varepsilon_{zz}$ from 0.69 to 0.70 at $\sigma_{xx} = \sigma_{zz} = p^{litho}$. The strain rate sensitivity, therefore, appears to play a small role in final waste compressibility and porosity predictions.

4. POSSIBLE AREAS FOR IMPROVEMENT

This chapter briefly discusses potential areas for improvement. To be clear, these improvements should not be viewed as prerequisites for credible disposal room porosity simulations. These possible areas for improvement are only suggestions to contemplate if new reasons arise to revise the waste material model.

The new model presented herein is for non-degraded waste. A simplistic argument for neglecting degraded waste is degradation processes can generate significant amounts of gas and the waste compaction behavior is not very important when significant gas pressures build up within the room. Butcher (1997b, Section 3.2.2) presented further arguments for focusing on non-degraded waste. Regardless, if it becomes important to predict the porosity (and permeability) of disposal rooms filled with degraded waste, Hansen and Mellegard (1998); Broome et al. (2014) presented uniaxial strain, triaxial stress, and hydrostatic stress compaction experiments on surrogate, degraded, waste. It might be possible to simply create another FD model calibration that captures the results from those degraded waste experiments.

The new model captures the triaxial and hydrostatic compaction measurements reasonably well, but its uniaxial stress response is much too compliant at large axial strains compared to the measurements. This poor uniaxial prediction is not considered an issue for disposal room simulations, as discussed in Section 3.4, but it could be important in other scenarios. For example, a roof fall on top of the containers, which is not considered in the disposal room model, would apply a largely uniaxial stress state to the containers. If one is interested in accurate container deformations directly after a roof fall, then it may make sense to create another FD model calibration that captures the measured uniaxial stress behavior.

Figure 3-9 shows that the waste elements in a disposal room simulation follow stress paths that are qualitatively different than the uniaxial, triaxial, and hydrostatic stress paths used in the experiments. In all the experiments, the mean (hydrostatic) stress was increased to some level, or set to zero, before generating a non-zero von Mises stress. The opposite sequence would be closer to the stress path in a disposal room: increase the von Mises stress to some level via uniaxial stress loading and then increase the mean stress to p^{litho}. Such experiments could be used for model calibration or model validation.

Uniaxial stress compaction experiments were used to characterize the strain rate dependence of the waste, as documented in Section 2.5. The decision to forgo capturing the uniaxial stress vs. strain behavior, however, made it challenging to calibrate the FD model's strain rate dependence, as discussed in Section 3.2.1. In the future, it might be better to experimentally characterize the hydrostatic strain rate dependence. The hydrostatic strain rate dependence reduces to a simple expression in the FD model, while the uniaxial strain rate dependence does not because $\dot{\lambda}$ varies with ξ under uniaxial stress (see Section 3.1.3). Furthermore, the hydrostatic behavior is more

relevant than uniaxial behavior for predicting the final porosity of disposal rooms. On the other hand, perhaps strain rate effects are of secondary importance since Fig. 3-12 shows that reducing the strain rate by ten orders of magnitude does not dramatically change the porosity at which the waste is able to resist the lithostatic pressure.

5. SUMMARY

One must have a credible model for the compaction of the standard waste containers within a WIPP disposal room in order to credibly predict the porosity (and permeability) of said disposal room. A review of the legacy waste material model, however, uncovered seven shortcomings:

1. Butcher (1997a) assumed a waste composition that was substantially different from recent, more accurate, estimates.
2. Butcher (1997a) assumed an initial waste porosity that was lower than recent, more accurate, estimates.
3. Butcher (1997b, Section 3.2.2) assumed the waste produced zero lateral stress (and zero lateral strain) in the oedometer tests used to derive the model's volumetric compaction curve.
4. The oedometer tests used to calibrate the legacy model only reached $p = 4.93$ MPa with the zero lateral stress assumption, yet lithostatic pressure at WIPP is $p^{litho} \approx 14.7$ MPa.
5. The Drucker-Prager yield surface was not calibrated against experimental measurements.
6. The legacy model predicts non-physical tensile out-of-plane stresses when in-plane compression is applied under plane strain conditions, which occurs in disposal room porosity simulations.
7. The legacy model assumes waste compaction does not depend on strain rate.

To rectify these shortcomings, a series of new experiments were conducted and a new waste material model was developed.

The new experiments utilized a surrogate waste that is more representative of the waste in WIPP standard containers than the waste assumed by the legacy model. The new surrogate waste composition was close to those reported in WIPP inventory estimates from CRA-2009, 2014, and 2019. This waste composition had 2.4× the weight fraction of metals and 0.23× the weight fraction of cellulosics as Butcher (1997a)'s assumed composition. The new surrogate waste porosity was 0.825, which is 1.2× the porosity assumed by Butcher (1997a).

The new experiments consisted of uniaxial, triaxial, and hydrostatic stress compaction tests on containers filled with the new surrogate waste. Only uniaxial and hydrostatic tests were performed on full-scale containers, while all three tests types were performed on 1/4-scale containers. Each piece of waste within the 1/4-scale containers was scaled down to1/4of its full-scale counterpart. During compaction, the waste was initially very compliant, but rapidly stiffened once the solid volume fraction exceeded 0.38. The 1/4-scale and full size containers produced stress vs. strain curves with similar shapes, but the full size containers were somewhat more compliant. Rather

than assuming zero lateral strain in the uniaxial and triaxial stress tests, the lateral strain was inferred from the volume strain. The volume strain was captured by measuring the volume of expelled air from each container, while being careful to avoid leaks. The lateral strain evolved slowly during the initial stages of compaction, but evolved more quickly as the waste became stiffer and stronger. Although uniaxial stress tests at strain rates ranging from 10^{-7} 1/s to 10^{-4} 1/s produced a fair degree of scatter, they appeared to detect a mild amount of strain rate dependence.

The results of the new waste compaction experiments were used to calibrate the FD constitutive model, thus creating a new waste material model. The calibration focused first on capturing the $^1/_4$-scale container behavior and then was adjusted to match the full-scale container behavior. As the FD model could not match all the experimental measurements, the calibration ignored the uniaxial stress vs. strain behavior once the waste stiffened, yet strove to capture the remaining measurements.

The newly calibrated model, not surprisingly, captured the experimental measurements far better than the legacy model. The legacy model responses were generally far too strong at a given strain and incorrectly predicted lateral shrinkage instead of lateral expansion. The new model responses, on the other hand, satisfactorily matched the stress–strain and lateral expansion measurements, except the stiff uniaxial response at large axial strains. A disposal room simulation, however, showed that the waste only experiences uniaxial compression early in a disposal room simulation, prior to when the waste stiffens. After the uniaxial period, the waste transitions towards a more hydrostatic stress state, which the new model captures well.

Material point plane strain compression simulations were used to further explore the model behaviors. The new model did not exhibit the non-physical tensile out-of-plane stress predicted by the legacy model under plane strain compression, meaning the new model should predict compressive stresses along the length of a disposal room. In addition, the new model was substantially weaker for the same strain, yet was substantially stronger for the same porosity, so it was not clear whether the new model would lower or raise the Lagrangian porosity within a room. Finally, a comparison of the new model at two strain rates 10 decades apart showed that the strain and porosity corresponding to p^{litho} was relatively insensitive to strain rate.

Although the new model has some possible areas for improvement, it adequately resolves all six shortcomings of the legacy model. The new waste material model is a large improvement and is ready for careful engineering use.

BIBLIOGRAPHY

B.M. Butcher, T.W. Thompson, R.G. VanBuskirk, and N.C. Patti. Mechanical compaction of Waste Isolation Pilot Plant simulated waste. Technical report SAND90-1206, Sandia National Laboratories, Albuquerque, New Mexico 87185 and Livermore, California 94550, June 1991.

C.M. Stone. Final disposal room structural response calculations. Technical report SAND97-0795, Sandia National Laboratories, Albuquerque, New Mexico 87185 and Livermore, California 94550, August 1997a.

B. Reedlunn, J. G. Argüello, and F.D. Hansen. A reinvestigation into Munson's model for room closure in bedded rock salt. *International Journal of Rock Mechanics and Mining Sciences*, 151, March 2022. doi: 10.1016/j.ijrmms.2021.105007.

S. King. Gas generation function for calculating waste creep closure. Internal Sandia Memorandum, August 2021.

LANL. Performance assessment inventory report – 2018. Technical report INV-PA-18, Revision 0, Los Alamos National Laboratory Carlsbad Operations, Carlsbad, NM, 2018.

W.E. Baker, G.E. Ransleven, G.J. Friesenhahn, and J.C. Hokanson. A review of accident simulation in low-level nuclear waste transportation. Technical report TTC-0054, Southwest Research Institute, San Antonio, TX, 1980.

M. Huerta, G.H. Lamoreaux, L.E. Romesberg, H.R. Yoshimura, B.J. Joseph, and R.A. May. Analysis, scale modeling, and full-scale tests of low-level nuclear waste drum response to accident environments. Technical report SAND80-2517, Sandia National Laboratories, Albuquerque, New Mexico, 1983.

J. VandeKraats. Quarter-scale modeling of room convergence effects on CH TRU drum waste emplacements using WIPP reference design geometries. Technical report DOE/WIPP 87-012, Westinghouse Experimental Engineering, Carlsbad, NM, 1987.

W.R. Wawersik. One-quarter-scale laboratory crush tests on unconfined waste cans and a confined waste package in support of the Waste Isolation Pilot Plant (WIPP). Technical report SAND98-2574, Sandia National Laboratories, Albuquerque, New Mexico, 2001.

C.M Stone. SANTOS: a two-dimensional finite element program for the quasistatic, large deformation, inelastic response of solids. Technical Report SAND90-0543, Sandia National Laboratories, Albuquerque, NM, USA; Livermore, CA, USA, 1997b.

Sierra/SolidMechanics. *Sierra/SolidMechanics 5.4 User's Guide.* Sandia National Laboratories, Albuquerque, NM, USA; Livermore, CA, USA, 5.4.1 edition, January 2022.

B.M. Butcher. A summary of the sources of input parameter values for the Waste Isolation Pilot Plant final porosity surface calculations. Technical report SAND97-0796, Sandia National Laboratories, Albuquerque, New Mexico 87185 and Livermore, California 94550, August 1997a.

DOE. Waste Isolation Pilot Plant transuranic waste baseline inventory report (revision 1). Technical report DOE/CAO-94-1005, U.S. Department of Energy, Carlsbad Area Office, Carlsbad, NM, February 1995.

B.M. Butcher. Waste Isolation Pilot Plant disposal room model. Technical report SAND97-0794, Sandia National Laboratories, Albuquerque, New Mexico 87185 and Livermore, California 94550, August 1997b.

J Randall Weatherby, William T Brown, and Barry M Butcher. The closure of WIPP disposal rooms filled with various waste and backfill combinations. In *The 32nd US Symposium on Rock Mechanics (USRMS)*. American Rock Mechanics Association, 1991.

G.D. Callahan. Disposal room calculations with alternative TRU waste models. Technical report WIPP:1.2.7:PA:QA-L:533999, RESPEC, prepared for Sandia National Laboratories, September 2004.

G.D. Callahan and F.D. Hansen. Transuranic waste model evaluation. In *40th US Symposium on Rock Mechanics (USRMS)*, number ARMA-2005-859. American Rock Mechanics Association, June 2005.

B.Y. Park and F.D. Hansen. Memo to David Kessel: Stresses at the centerline of the WIPP waste. WIPP Records Center ERMS# 538781, Sandia National Laboratories, Carlsbad, NM, February 2005.

Gary D. Callahan. *Documentation of SPECTROM-32: A Finite Element Thermomechanical Stress Analysis Program, Revision 1*. RESPEC, Rapid City, SD, 2002.

S.T. Broome and L.S. Costin. Compaction behavior of emplaced waste. WIPP Test Plan TP 08-01 Revision 1, Sandia National Laboratories, Albuquerque, NM, USA, 2010.

Courtney G. Herrick. Analysis plan for the development of a model for the compaction behavior of emplaced WIPP waste. WIPP Analysis Plan AP-180 Rev. 0, ERMS 569227, Sandia National Laboratories, December 2017.

S.T. Broome, M.D. Ingraham, G.M. Flint, M.B. Hileman, P.C. Barrow, and C.G. Herrick. Laboratory testing of surrogate non-degraded Waste Isolation Pilot Plant materials. In *50th US Rock Mechanics/Geomechanics Symposium*, number ARMA-2016-120. American Rock Mechanics Association, June 2016.

M. Orlowski. WIPP full scale hydrostatic testing of 55 gallon waste disposal drums, final report, issue 1. Technical report SwRI Project 18.18197.03, Southwest Research Institute, San Antonio, TX, 2015.

F.D. Hansen and K.D. Mellegard. Physical and mechanical properties of degraded waste surrogate material. In *Proceedings, 3rd North American Rock Mechanics Syposium, Cancun, Mexico, June 3-5, 1998*. Published in *Int. J. Rock Mech. Min. Sci.* 35(4/5): Paper No. 081, March 1998.

S.T. Broome, D.R. Bronoswki, S.J. Kuthakun, C.G. Herrick, and T.W. Pfeifle. Compaction behavior of surrogate degraded emplaced WIPP waste. Technical report SAND2014-1897, Sandia National Laboratories, Albuquerque, New Mexico, 2014.

EPA. Criteria for the certification and re-certification of the Waste Isolation Pilot Plant's compliance with the disposal regulations: Recertification decision. Technical report EPA-HQ-OAR-2004-0025-0007, U.S. Environmental Protection Agency, April 2006.

EPA. Criteria for the certification and re-certification of the Waste Isolation Pilot Plant's compliance with the disposal regulations: Recertification decision. Technical report EPA-HQ-OAR-2014-0609-0081, U.S. Environmental Protection Agency, July 2017.

EPA. Criteria for the certification and re-certification of the Waste Isolation Pilot Plant's compliance with the disposal regulations: Recertification decision. Technical report EPA-HQ-OAR-2019-0534-0043, U.S. Environmental Protection Agency, May 2022.

DOE. Waste Isolation Pilot Plant transuranic waste baseline inventory report (revision 3). Technical report DOE/CAO-95-1121, U.S. Department of Energy, Carlsbad Area Office, Carlsbad, NM, 1996.

LANL. Performance assessment inventory report – 2008. Technical report INV-PA-08, Revision 0, Los Alamos National Laboratory Carlsbad Operations, Carlsbad, NM, 2008.

LANL. Performance assessment inventory report – 2012. Technical report INV-PA-12, Revision 0, Los Alamos National Laboratory Carlsbad Operations, Carlsbad, NM, 2012.

F.D. Hansen, M.K. Knowles, T.W. Thompson, M. Gross, J.D. McLennan, and J.F. Schatz. Description and evaluation of a mechanistically based conceptual model for spall. Technical report SAND97-1369, Sandia National Laboratories, Albuquerque, New Mexico, 1997.

C.G. Herrick. Update report on the mechanical testing of drums filled with surrogate nondegraded WIPP waste. WIPP Records Center ERMS# 574654, Sandia National Laboratories, Carlsbad, NM, 2020.

T.C.T Ting and T. Chen. Poisson's ratio for anisotropic elastic materials can have no bounds. *The quarterly journal of mechanics and applied mathematics*, 58(1):73–82, 2005.

M.K. Neilsen, W.Y. Lu, W.M. Scherzinger, T.D. Hinnerichs, and C.S. Lo. Unified creep plasticity damage (UCPD) model for rigid polyurethane foams. Technical report SAND2015-4352, Sandia National Laboratories, Albuquerque, New Mexico 87185 and Livermore, California 94550, May 2015.

M.K. Neilsen. On the implementation of the foam damage model in Sierra/SolidMechanics. Personal communication, November 2022.

A. APPENDIX – PLOTS OF EXPERIMENTAL RESULTS

This appendix includes the plots of the experimental results

A.1. Uniaxial Compression Test - Experimental Results

The results of the uniaxial compression tests can also be found in Herrick (2020), but Herrick (2020) computed the lateral strains incorrectly (see footnote in Section 2.4).

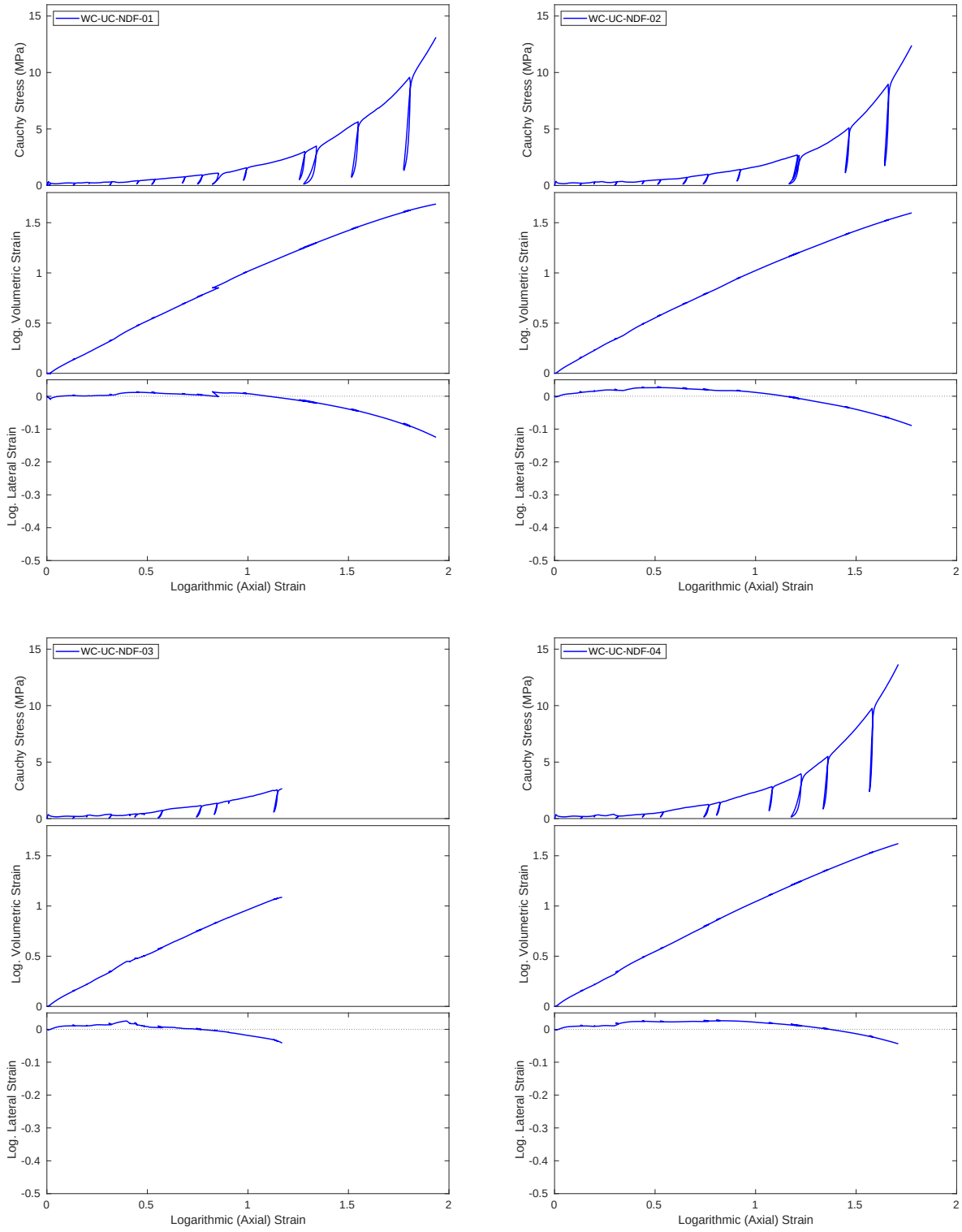

Figure A-1. Plots of uniaxial compression test experimental results for the tests performed on the full-scale drums at the strain-rate = 10^{-4} sec^{-1}. A total four samples were tested. These composite plots are the results for each individual test showing the Cauchy stress, the logarithmic volumetric strain, and the logarithmic lateral strain plotted against the logarithmic axial strain.

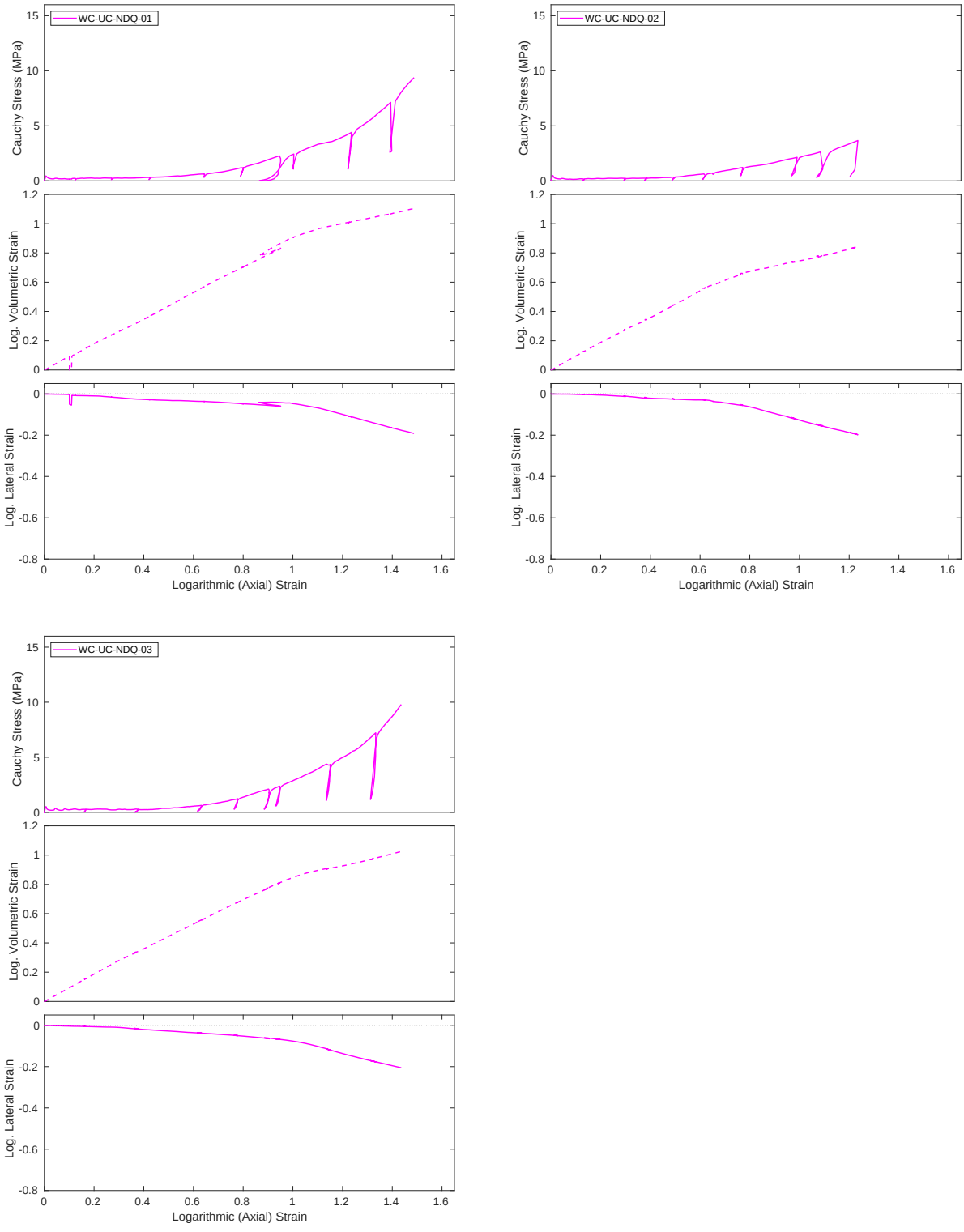

Figure A-2. Plots of uniaxial compression test experimental results for the tests performed on the $^1/_4$-scale drums at the strain-rate = 10^{-4} sec^{-1}. A total five samples were tested. These composite plots are the results for each individual test showing the Cauchy stress, the logarithmic volumetric strain, and the logarithmic lateral strain plotted against the logarithmic axial strain.

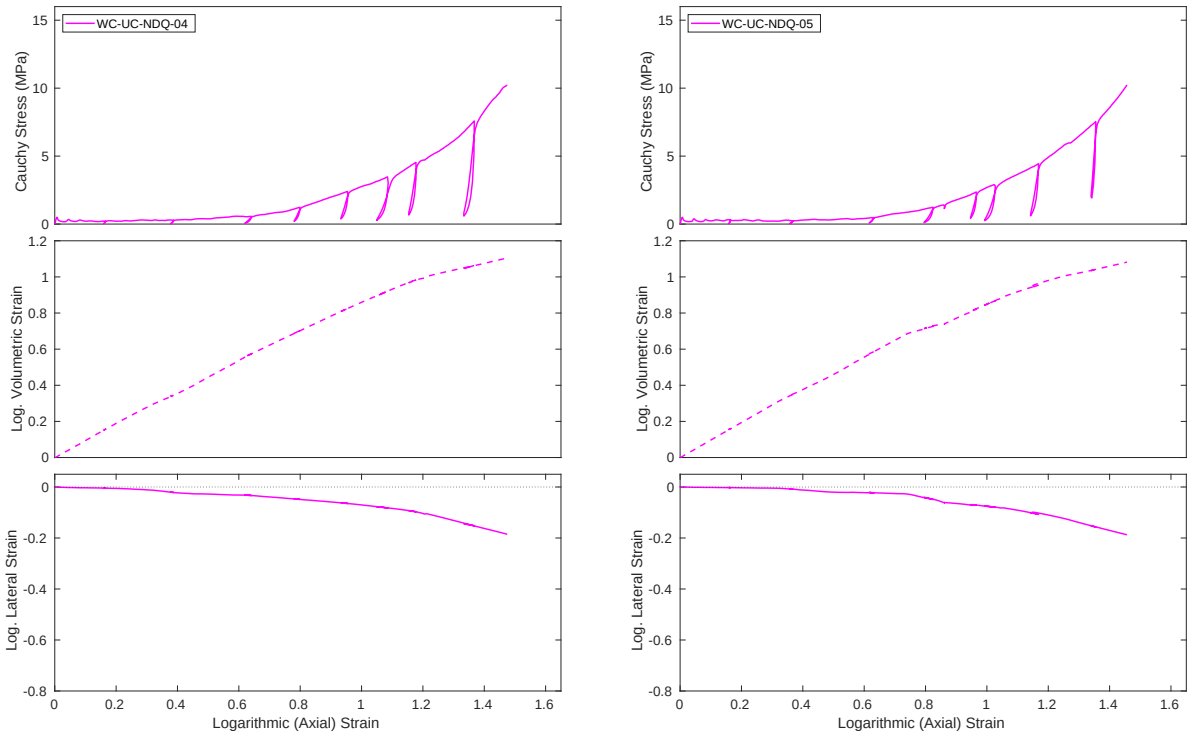

Figure A-2. (cont.) Plots of uniaxial compression test experimental results for the tests performed on the $^1/_4$-scale drums at the strain-rate = 10^{-4} sec^{-1}. A total five samples were tested. These composite plots are the results for each individual test showing the Cauchy stress, the logarithmic volumetric strain, and the logarithmic lateral strain plotted against the logarithmic axial strain.

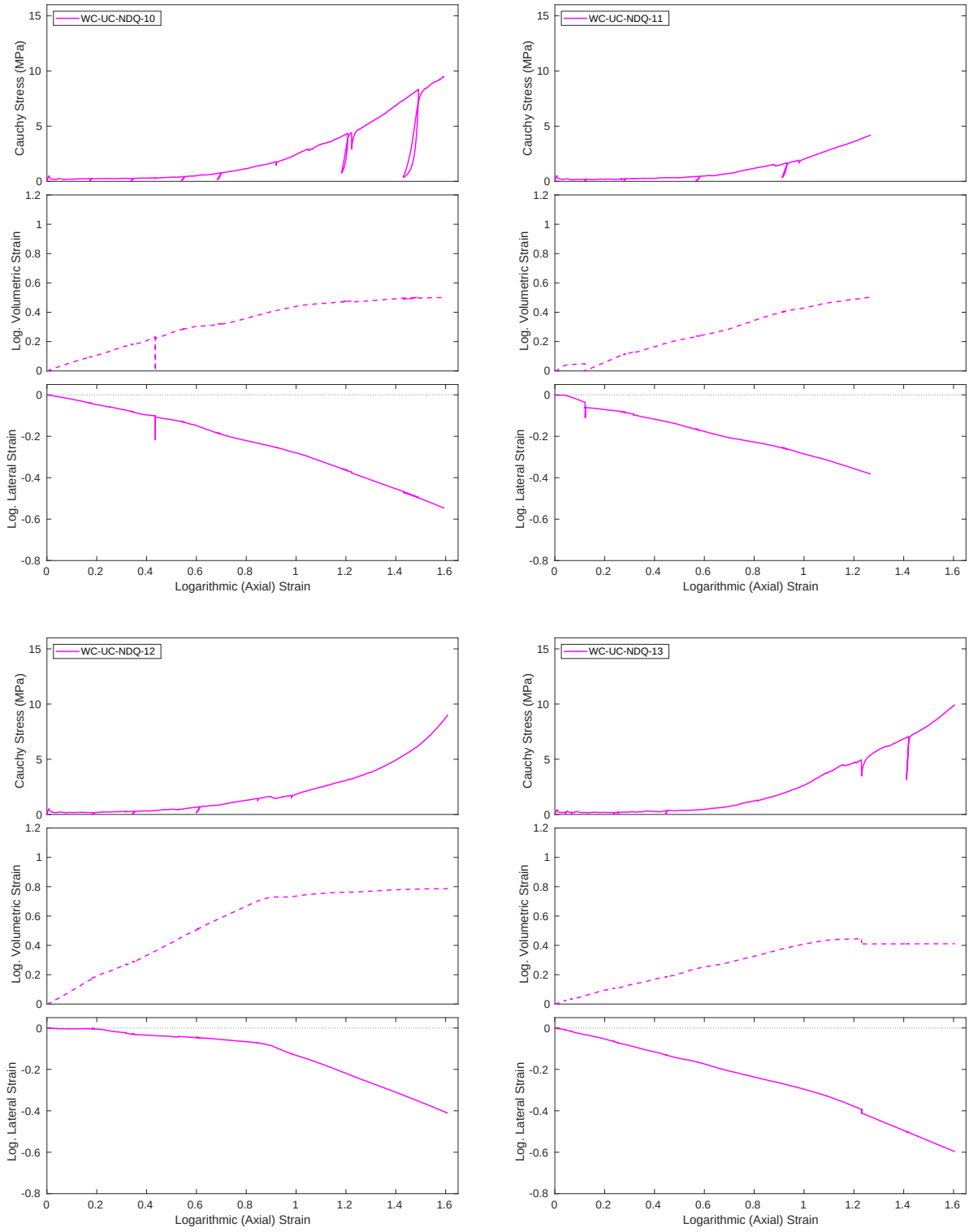

Figure A-3. Plots of uniaxial compression test experimental results for the tests performed on the $^1/_4$-scale drums at the strain-rate = 10^{-5} sec^{-1}. A total four samples were tested. These composite plots are the results for each individual test showing the Cauchy stress, the logarithmic volumetric strain, and the logarithmic lateral strain plotted against the logarithmic axial strain.

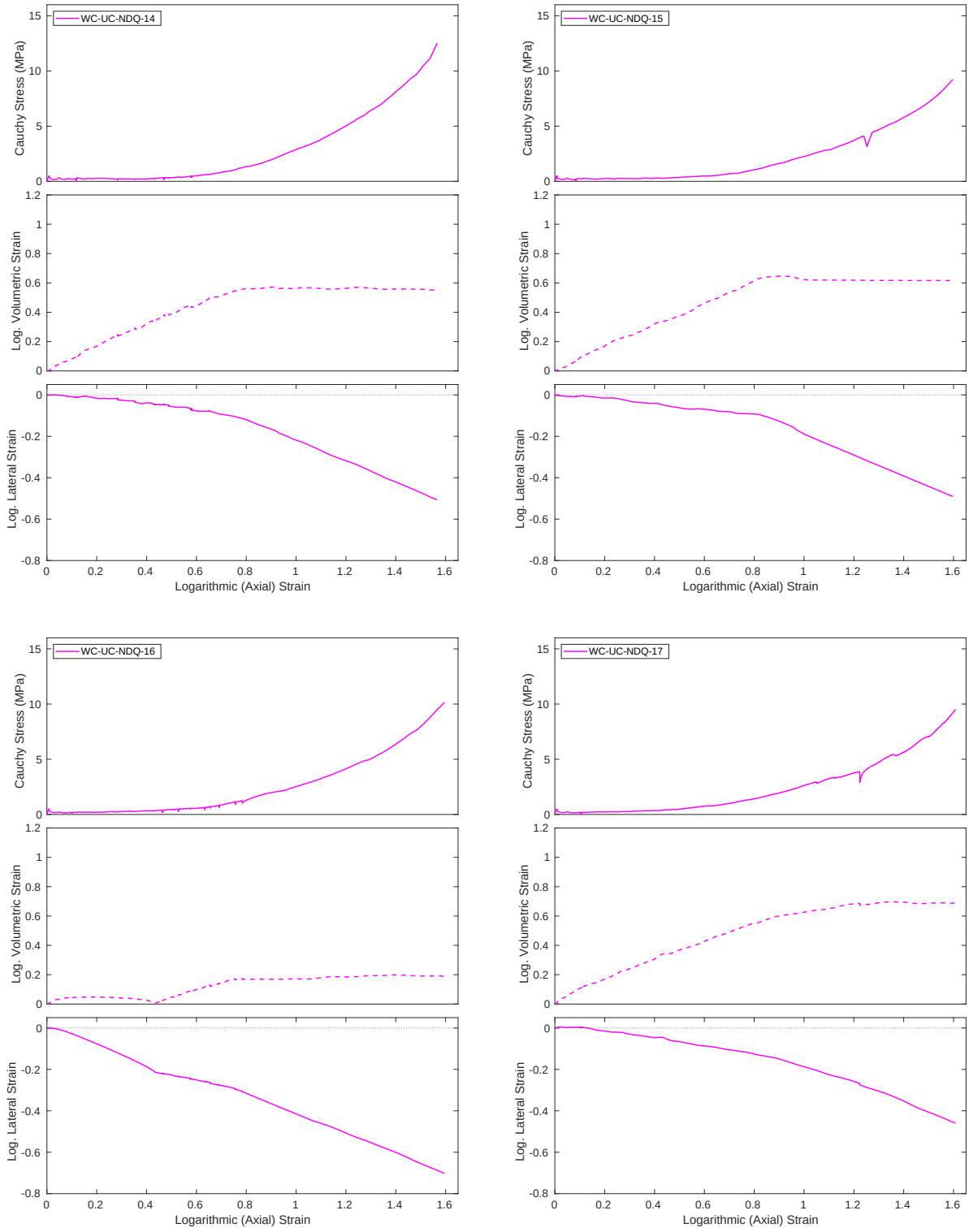

Figure A-4. Plots of uniaxial compression test experimental results for the tests performed on the $^1/_4$-scale drums at the strain-rate = 2.1×10^{-6} sec^{-1}. A total four samples were tested. These composite plots are the results for each individual test showing the Cauchy stress, the logarithmic volumetric strain, and the logarithmic lateral strain plotted against the logarithmic axial strain.

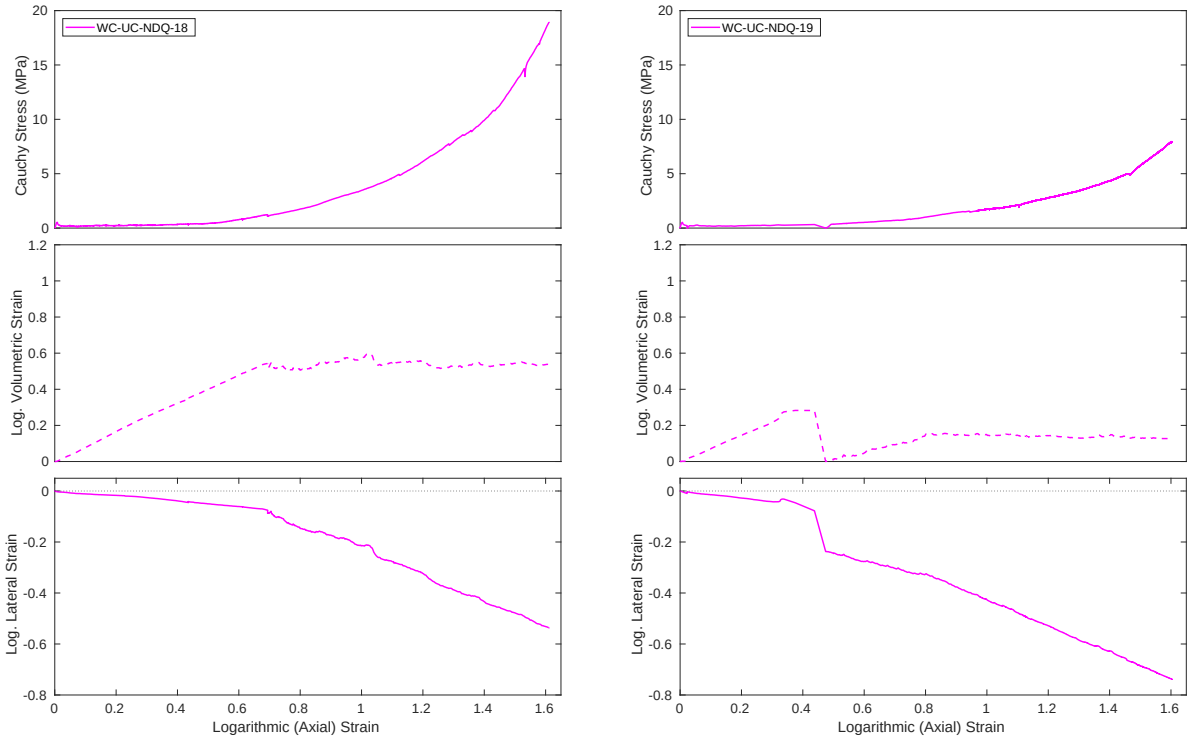

Figure A-5. Plots of uniaxial compression test experimental results for the tests performed on the $^1/_4$-scale drums at the strain-rate = 10^{-7} sec^{-1}. A total two samples were tested. These composite plots are the results for each individual test showing the Cauchy stress, the logarithmic volumetric strain, and the logarithmic lateral strain plotted against the logarithmic axial strain.

A.2. Triaxial Compression Test - Experimental Results

The results of the uniaxial compression tests can also be found in Herrick (2020), but Herrick (2020) computed the lateral strains incorrectly (see footnote in Section 2.4).

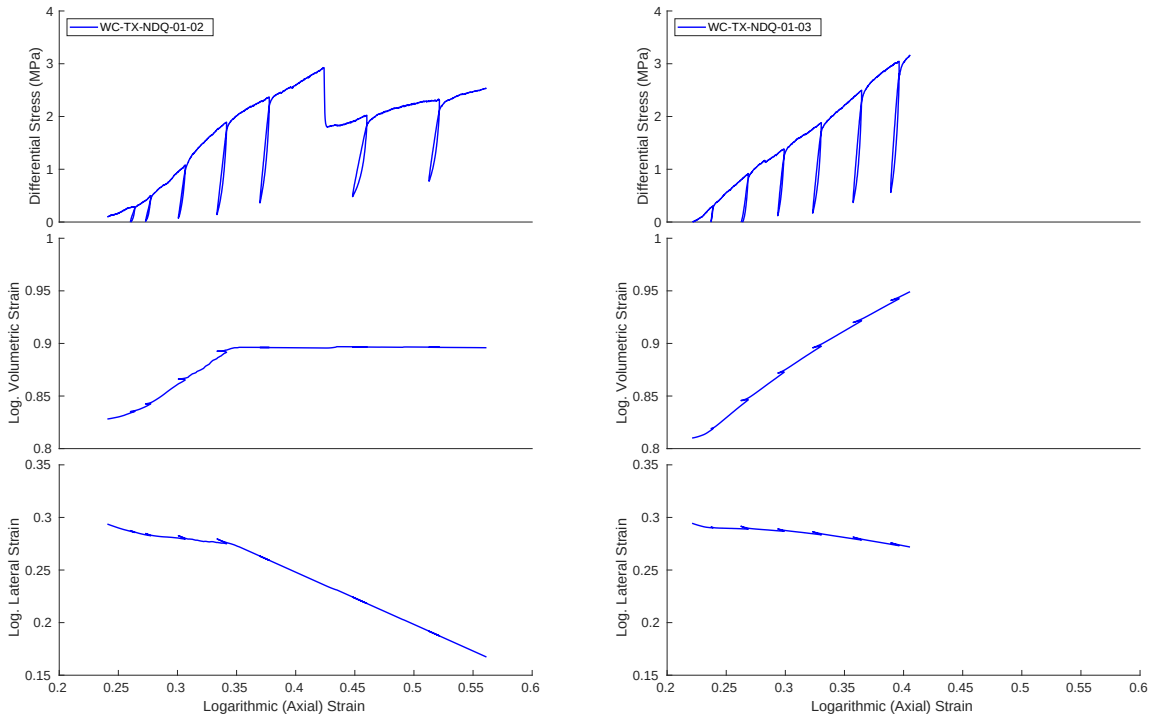

Figure A-6. Plots of triaxial compression test experimental results for the tests performed on the 1/4-scale cans at a confining stress of 1 MPa. These composite plots are the results for each individual test showing the differential stress, the logarithmic volumetric strain, and the logarithmic lateral strain plotted against the logarithmic axial strain.

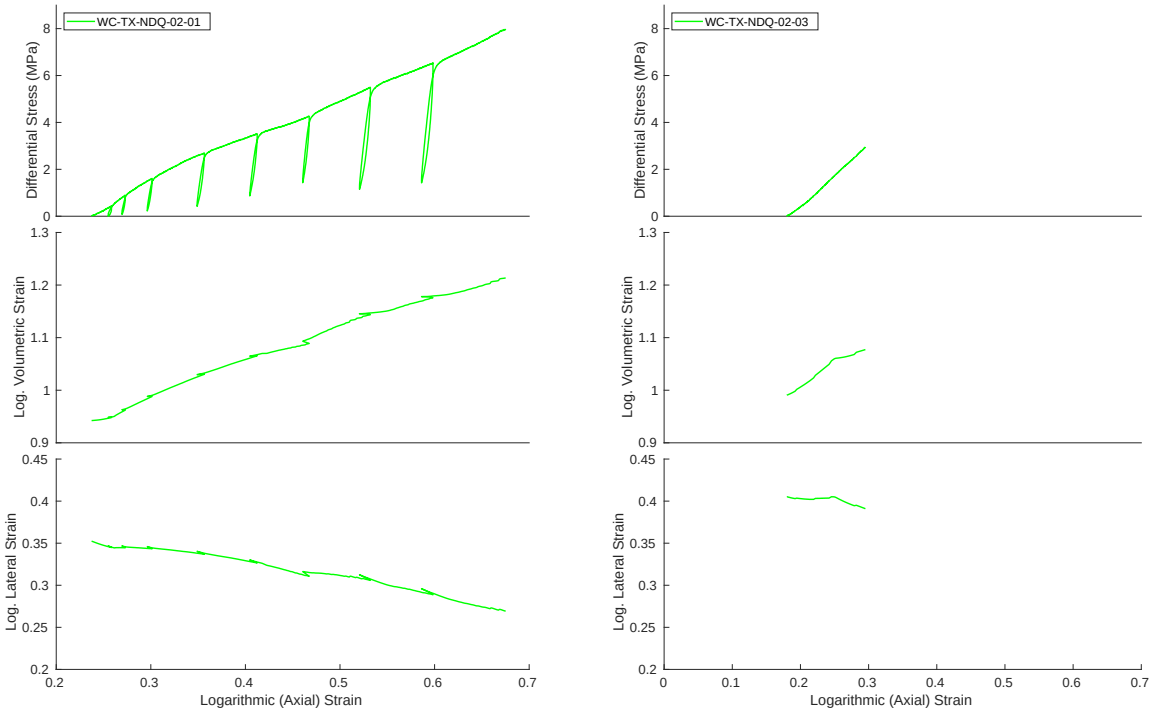

Figure A-7. Plots of triaxial compression test experimental results for the tests performed on the $^1/_4$-scale cans at a confining stress of 2 MPa. These composite plots are the results for each individual test showing the differential stress, the logarithmic volumetric strain, and the logarithmic lateral strain plotted against the logarithmic axial strain.

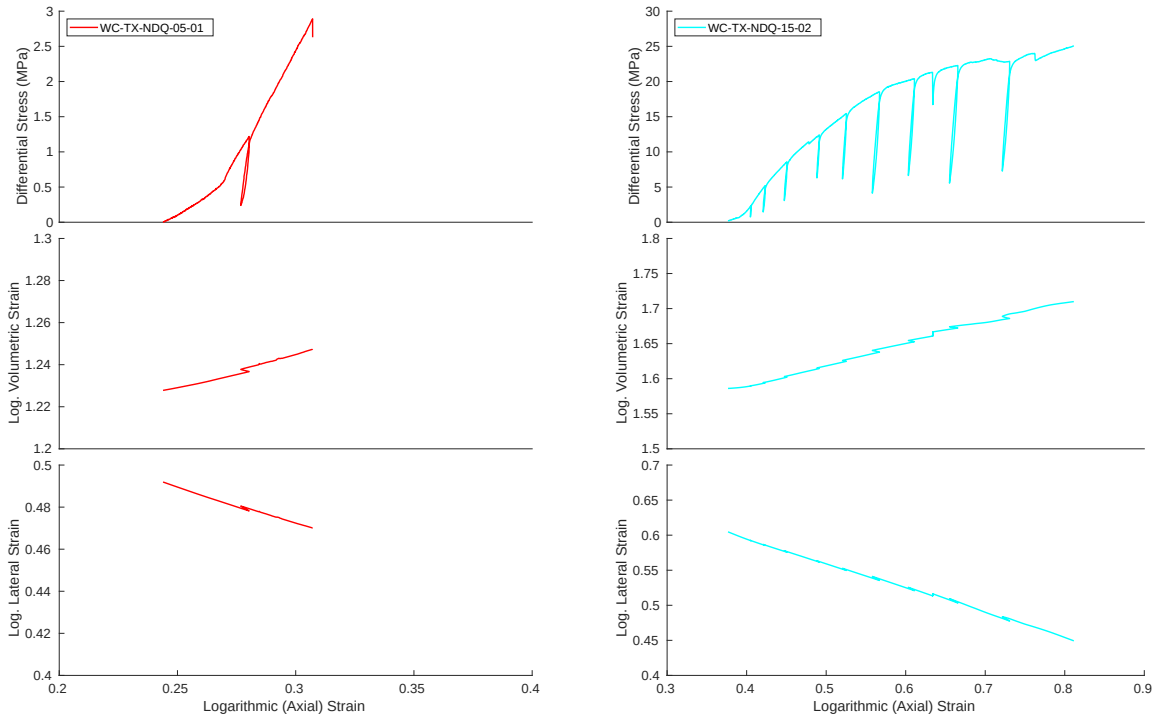

Figure A-8. Plots of triaxial compression test experimental results for the tests performed on the 1/4-scale cans at a confining stress of 5 and 15 MPa (left and right, respectively). These composite plots are the results for each individual test showing the differential stress, the logarithmic volumetric strain, and the logarithmic lateral strain plotted against the logarithmic axial strain.

A.3. Hydrostatic Compression Test - Experimental Results

The results of the hydrostatic compression tests can also be found in Herrick (2020).

A.3.0.1. Full-scale samples

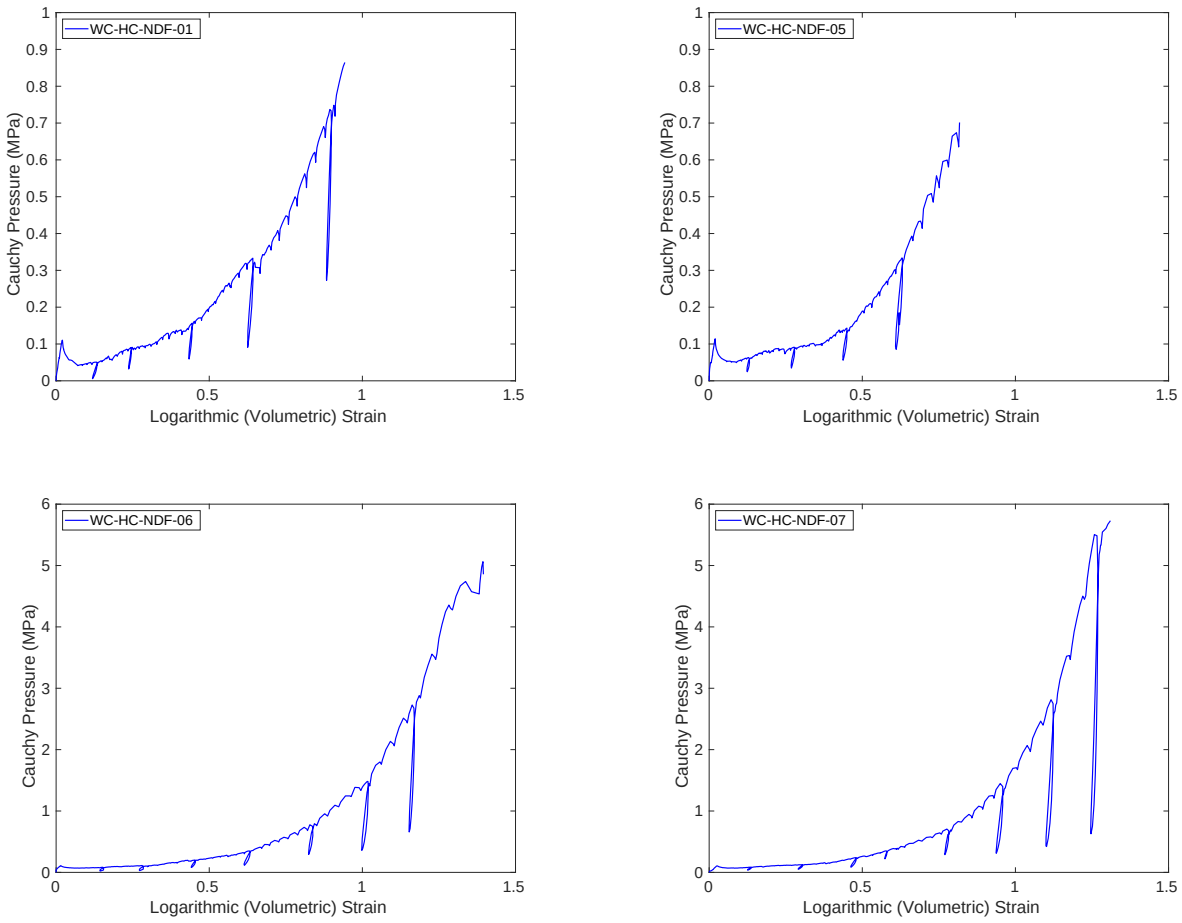

Figure A-9. Plots of experimental results for hydrostatic compression tests for the Full-scale samples

A.3.0.2. 1/4-scale samples

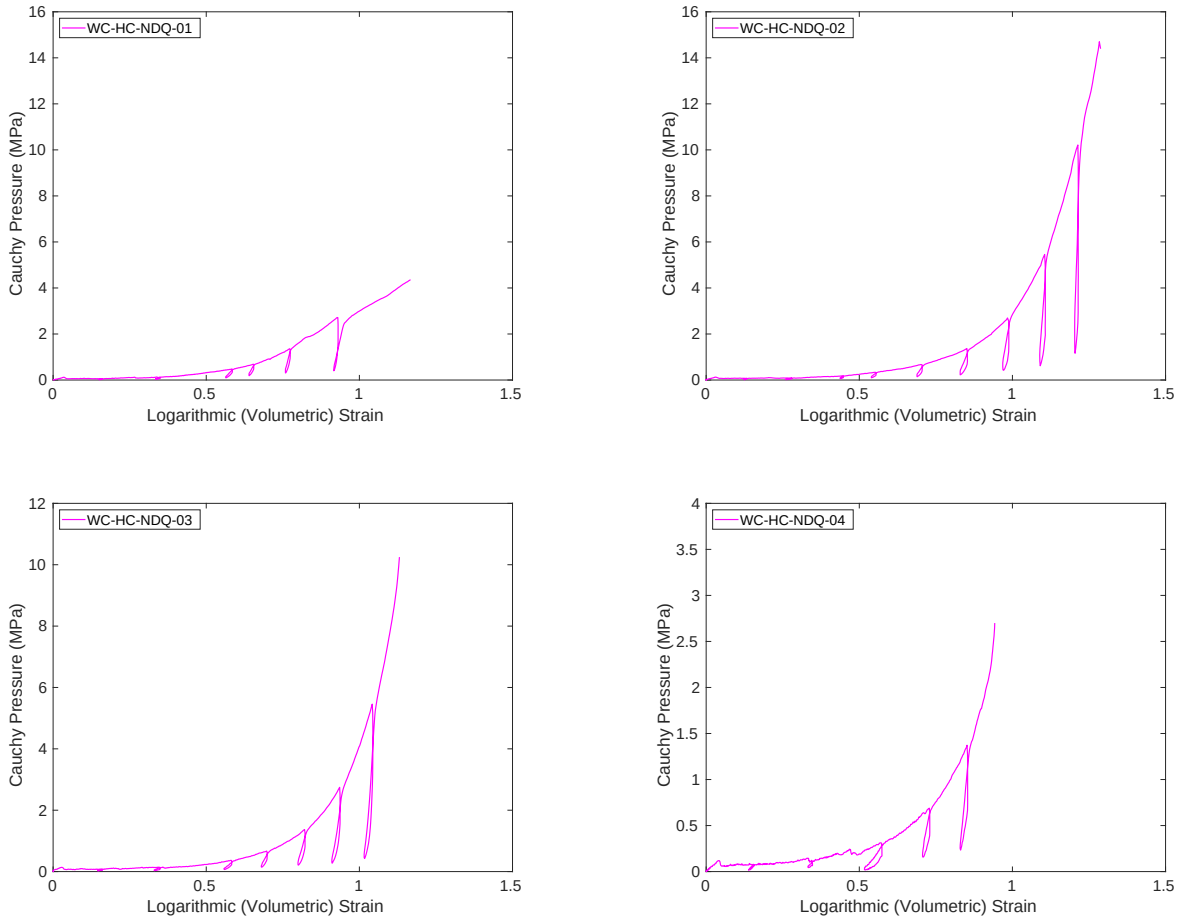

Figure A-10. Plots of experimental results for hydrostatic compression tests for the 1/4-scale samples

B. APPENDIX – FOAM DAMAGE MATERIAL MODEL PARAMETERS

These material parameters are the parameters that were used in the simulations detailed in the sections above. Parameter names and definitions can be found in the Sierra/SM User's guide (Sierra/SolidMechanics, 2022) under the Foam Damage materials models section.

```
###
###     Material property definitions
###
##
##      Input block for Container
##      N, kg, m, seconds, C Stress: Pa, Temperature: C
##
    begin property specification for material container
        density = 505.5         ## kg/m3
        thermal engineering strain function = container_Thermal
        begin parameters for model foam_damage
            youngs modulus = 4000.0e6     ## locked up Pa
            poissons ratio = 0.300
            phi = 0.175           ## volume fraction solids
            flow rate = 1.000
            power exponent = 1.000
            tensile strength = 100.0e6     ## high so no fail in tension
            adam = 1.000
            bdam = 0.330
            youngs function = container_Modulus
            poissons function = container_PR
            rate function = container_Rate
            exponent function = container_Expo
            shear hardening function = container_Shear
            hydro hardening function = container_Hydro
            beta function = container_Beta
            youngs phi function = container_E
            poissons phi function = container_Constant
            damage function = container_Damage
        end parameters for model foam_damage
    end property specification for material container

    begin definition for function container_Damage
        type is piecewise linear
```

```
        begin values
                0.00    0.00
                0.50    0.00
                0.60    0.00
              100.00    0.00
        end values
    end definition for function container_Damage

## flow direction 1 = radial, 0 = associated
    begin definition for function container_Beta
        type is piecewise linear
        begin values
                0.00    0.700
                0.20    0.700
                0.25    0.650
                0.30    0.550
                0.35    0.400
                0.40    0.220
                0.45    0.150
                0.50    0.075
                0.64    0.000
                1.00    0.000
               10.00    0.000
        end values
    end definition for function container_Beta

##
## from unloading slopes (function values are multiplied x reference value above)
##
    begin definition for function container_E
        type is piecewise linear
        begin values
                0.00    0.010
                0.25    0.015
                0.40    0.025
                0.50    0.075
                0.65    0.128
                1.00    0.500
                2.00    1.000
              100.00    1.000
        end values
    end definition for function container_E

    begin definition for function container_PR
        type is constant
```

```
        begin values
            1.000
        end values
    end definition for function container_PR

## steel 13 ppm/C
    begin definition for function container_Thermal
        type is piecewise linear
        ordinate is strain
        abscissa is temperature
        begin values
            -500.0    0.000
               0.0    0.000
             500.0    0.000
        end values
    end definition for function container_Thermal

    begin definition for function container_Constant
        type is constant
        begin values
            1.0
        end values
    end definition for function container_Constant

    begin definition for function container_Modulus
        type is piecewise linear
        ordinate is temperature
        abscissa is time
        begin values
            -1.0e5    1.00
              2.0e    1.00
             1.3e5    1.00
        end values
    end definition for function container_Modulus

# parameter "h"
    begin definition for function container_Rate
        type is constant
        begin values
            -55.0
        end values
    end definition for function container_Rate

# parameter "n"
    begin definition for function container_Expo
```

```
    type is constant
    begin values
        23.0
    end values
end definition for function container_Expo

begin function container_Shear
    type is piecewise linear
    begin values
          0.000      0.02e6
          0.112      0.02e6
          0.280      0.02e6
          0.336      0.02e6
          0.392      0.04e6
          0.448      0.07e6
          0.470      0.12e6
          0.493      0.19e6
          0.504      0.22e6
          0.560      0.36e6
          0.582      0.46e6
          0.616      0.72e6
          0.672      1.32e6
          0.694      1.74e6
          0.728      2.80e6
          0.784      4.42e6
          0.896     10.52e6
          1.008     14.62e6
          1.120     30.00e6
         11.200    500.00e6
    end values
end function

begin function container_Hydro
    type is piecewise linear
    begin values
```

```
            0.000       0.012e6
            0.280       0.012e6
            0.336       0.036e6
            0.448       0.132e6
            0.504       0.240e6
            0.560       0.480e6
            0.672       1.440e6
            0.784      12.000e6
            0.896      45.600e6
            1.008      84.000e6
            1.120     168.000e6
           11.200     960.000e6
        end values
    end function

###
### end of input block for container material
###
```

DISTRIBUTION

Email—Internal

Name	Org.	Sandia Email Address
Walter Witkowski	1550	wrwitko@sandia.gov
Jim Bean	1554	jebean@sandia.gov
Aaron Brundage	1554	albrund@sandia.gov
Chet Vignes	1558	cvignes@sandia.gov
Stacy Nelson	1558	smnelso@sandia.gov
Michael Neilsen	1558	mkneils@sandia.gov
Devin O'Connor	1558	dtoconn@sandia.gov
Jibril Coulibaly	1558	jbcouli@sandia.gov
Greg Flint	8261	gmflint@sandia.gov
Emily Stein	8840	ergiamb@sandia.gov
Edward Matteo	8842	enmatte@sandia.gov
Chris Camphouse	8842	rccamph@sandia.gov
Melissa Mills	8842	mmmills@sandia.gov
Robert Rechard	8842	rprecha@sandia.gov
Kristopher Kuhlman	8844	klkuhlm@sandia.gov
Rodney Kieth	8880	rlkeith@sandia.gov
D. Kicker	8880	dckicke@sandia.gov
Grace Duran	8880	gasosa@sandia.gov
Ross Kirkes	8881	grkirke@sandia.gov
Seth King	8881	sking@sandia.gov
Stephen Wagner	8881	swagner@sandia.gov
Byoung Park	8912	bypark@sandia.gov
Todd Zeitler	8912	tzeitle@sandia.gov
Austin Holland	8914	aaholla@sandia.gov
Matt Ingraham	8914	mdingr@sandia.gov
Perry Barrow	8914	pbarrow@sandia.gov
Technical Library	1911	sanddocs@sandia.gov

Email—External

Name	Company Email Address	Company Name
Anderson Ward	anderson.ward@cbfo.doe.gov	U.S. Department of Energy Carlsbad Field Office
George Basabilvazo	george.basabilvazo@cbfo.doe.gov	U.S. Department of Energy Carlsbad Field Office
Mike Gross	mike_gross@earthlink.net	Nuclear And Regulatory Support Services LLC
Gordan Gjerapic	ggjerapic@gmail.com	ZG-Geo Ltd.
Frank Hansen	francis.d.hansen@gmail.com	N/A
J. Guadalupe Arguello	llae.arguello@att.net	N/A

Sandia National Laboratories

Sandia National Laboratories is a multimission laboratory managed and operated by National Technology & Engineering Solutions of Sandia LLC, a wholly owned subsidiary of Honeywell International Inc., for the U.S. Department of Energy's National Nuclear Security Administration under contract DE-NA0003525.